



**Scuola di
Scienze Matematiche
Fisiche e Naturali**

Corso di Laurea Magistrale in
Scienze Fisiche e Astrofisiche

LIMIT SHAPES IN FERMIONIC MODELS

Supervisor:
Dr. Filippo Colomo

Co-Supervisor:
Dr. Jean-Marie Stéphan

Candidate:
Saverio Bocini

Academic Year:
2019/2020

Contents

Summary	3
Abstract	3
Chapters' contents	4
Conventions	5
1 Introduction	7
1.1 Limit shape phenomenon and dimer models	7
1.2 Free fermions	10
1.3 From dimers to imaginary-time fermions	13
1.4 Our model	19
1.4.1 Definition	19
1.4.2 Symmetries of the density profile	20
1.4.3 Pure nearest-neighbour hopping limit	23
1.4.4 The density problem	24
1.4.5 Cases with well-defined density	26
2 The Tools	29
2.1 Free fermions' techniques	29
2.1.1 Some useful properties	29
2.1.2 Wick's theorem	32
2.2 Semi-infinite Toeplitz matrices	36
2.2.1 Definition	36
2.2.2 Wiener-Hopf decomposition	37
2.2.3 Inversion formula	38
3 Exact Two-point Function	41
3.1 Scope of the chapter	41
3.2 Two-point function as a product of matrices	41
3.3 Two-point function as a double integral	44
3.4 Finite-size two-point correlation function	49

4 The Density Problem	51
4.1 Asymptotics: the starting point	51
4.2 Pure nearest-neighbour hopping	52
4.2.1 Revisiting the exact formulas	52
4.2.2 Limit shapes	54
4.3 Density profile at zero time	61
4.4 Full limit shapes	63
4.5 Pure next-nearest-neighbour hopping limit	69
5 Alternative Geometries	73
5.1 Beyond domain wall geometry	73
5.2 Correlation function for domain-wall-like geometries	74
5.3 Scaling limit in domain-wall-like geometries	79
5.3.1 General treatment	79
5.3.2 Specialization to our dispersion relation	80
5.3.3 Density profile for half-filled domain wall geometry	81
5.3.4 Other geometries and hoppings	85
5.4 Generalization of the domain-wall-like geometry	86
6 Final Remarks and Conclusion	91
Appendix A Saddle-Point Method for the Density	95
Appendix B Hilbert Transform	99
Bibliography	103

Summary

Abstract

Our starting point is a well known model of free fermions in imaginary time, where particles can hop to nearest neighbours on a one-dimensional lattice. The system is considered in the domain wall geometry, that is assuming that the initial and final states correspond both to the state where half the lattice is completely filled and the other half is empty. The motivation to study this model lies first of all in its connection with other important statistical models, such as a particular dimer model and the XX quantum spin chain. Secondly, the model is interesting because, in its simplicity, its density profile exhibits the limit shape phenomenon in the scaling limit, consisting in a spatial separation of phases between a deterministic region, where the density is either zero or one, and a fluctuating one, where the density is between zero and one.

The purpose of this work is to study some generalizations of the model described above, perturbing the Hamiltonian with a next-nearest-neighbour-hopping term and/or modifying the initial and final conditions. These changes, beside leading to different shapes for what concerns the separation of phases, also give rise to new features. In particular, the fact that we allow the fermions to jump over each other brings some non-trivial minus-signs in the computation of the density. This, combined with the non-unitarity of the evolution in imaginary time, results in the possibility for the density to be ill-defined, i.e. taking values outside the range $[0, 1]$. In this work we focus on the problems exhibited by the density, characterizing the regions where it is not well-defined.

Another motivation for studying limit shapes for this kind of model is the relation, through the Wick rotation, to real-time quantum quench problems. Some results in this direction were found first starting directly from imaginary time, then performing an analytic continuation to real time. However, the analytic continuation is not justified for every model and it is known that there are Hamiltonians that do not map to a statistical model with positive Boltzmann weights. By presenting models where the density is not between zero and one, we provide explicit examples where the analytic continuation is not possible.

Chapters' contents

Here is briefly how the chapters are organized:

- Ch. 1: The first section is dedicated to the introduction of the limit shape phenomenon; a few examples will be shown, without aiming at a complete description. In the following section the second general topic entering this work, namely free fermions, is introduced; here only the notations are discussed, while more technical details are left to Chapter 2. In the third section it will be shown how our starting model is closely related to a statistical mechanics model of dimers. Finally, the last section is devoted to introduce the main model we will focus on.
- Ch. 2: Some necessary theoretical tools are introduced, namely some free fermions techniques, including Wick's theorem, and the theory of semi-infinite Toeplitz matrices.
- Ch. 3: An exact integral formula for the two-point correlation function is obtained for a fairly general model of free fermions in domain wall geometry. This is done by the means of Wick's theorem and semi-infinite Toeplitz matrices' properties, recovering a known result by an alternative derivation. The new derivation will prove particularly suitable for generalization to other geometries.
- Ch. 4: The formula derived in Chapter 3 is used to study the density profile in the scaling limit for our model. This allows to characterize its limit shapes and justify the existence of regions where the density is ill-defined.
- Ch. 5: The exact formula of Chapter 3 is generalized to different geometries and it is then applied to study the limit shapes for our model in a such geometries. Considering alternative geometries will also allow to understand the problem of the ill-definition of the density in more general terms.
- Ch. 6: We draw some conclusions and mention some possible developments.

Conventions

Formulas and Symbols

Anti-commutator:

$$[A, B]_+ = AB + BA$$

Momentum basis:

$$c_x^\dagger = \int_{-\pi}^{+\pi} \frac{dk}{2\pi} e^{-ikx} d^\dagger(k)$$

$$c_x = \int_{-\pi}^{+\pi} \frac{dk}{2\pi} e^{+ikx} d(k)$$

Imaginary-time evolution:

$$A(\tau) = e^{\tau H} A e^{-\tau H}$$

Lattice-sites positions:

$$\tilde{\mathbb{Z}} = \mathbb{Z} + \frac{1}{2}$$

Position basis:

$$c_{i_1}^\dagger \dots c_{i_n}^\dagger |0\dots0\rangle, \quad i_1 < i_2 < \dots < i_n$$

Identity matrix $l \times l$:

$$\mathbb{I}_l$$

Acronyms

NN:

nearest-neighbour

NNN:

next-nearest-neighbour

Chapter 1

Introduction

1.1 Limit shape phenomenon and dimer models

We start by introducing one of the main topics of this work: the *limit shape phenomenon*. This phenomenon is observed in some lattice models, in the so-called *scaling limit*, where the number of sites of the lattice is sent to infinity and the lattice parameter to zero, in such a way that the size of the system stays constant. In such limit, under particular boundary conditions, these models may exhibit spatial phase separation, with the emergence of ordered and disordered regions, sharply separated by smooth curves, known as *arctic curves*. Correspondingly, the order parameter of the model acquires spatial dependence, with a non-trivial profile. We call *limit shape* the (integrated) profile of the order parameter for some given system.

The archetypical examples of models exhibiting the limit shape phenomenon are dimer models [1]. They may be defined on generic graphs but, for simplicity, we will restrict to lattice graphs. Moreover, we consider only *bipartite* lattices, that is we assume that one can label lattice sites with two colours, say black and white, in such a way that each lattice point has all its nearest neighbours of the opposite colour (e.g., the square and the hexagonal lattice are bipartite, while the triangular lattice is not). On this kind of lattice we introduce the dimers, which are objects that cover two neighbouring lattice sites each; equivalently, we can also see a dimer as covering a lattice link, meaning that it occupies the two sites connected by that lattice link. Finally, we consider the ensemble of dimers configuration, where an allowed configuration of dimers is such that each lattice site is occupied by one and only one dimer.

Dimers can be divided in classes, according to their orientation and the colours of the underlying lattice that they cover; see Fig. (1.1) for the case of the square lattice. To define ensemble averages, a probability distribution (taken uniform in the simplest cases) is specified. At this point, natural questions are for instance the distributions of the various classes of dimers. Examples of dimer coverings of an



Figure 1.1: All four classes of dimers for a two-dimensional square lattice are listed. The underlying square lattice is coloured with black and white to highlight that it is bipartite. The colour code for the dimers is: vertical dimers in blue (red) if their bottom part touches a black (white) lattice site; horizontal dimers in green (yellow) if their left part that touches a black (white) lattice site.

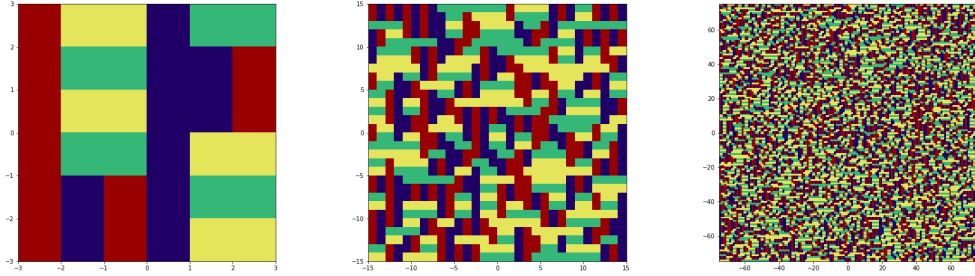


Figure 1.2: Dimer coverings of an $L \times L$ grid, chosen uniformly at random. From left to right, $L = 3, 15, 75$. The colour code is the same as in Fig. 1.1, while dimers have been made thicker to make the pictures look nicer. The pictures are generated using a Monte Carlo algorithm: start from any simple configuration; pick a plaquette (i.e. a square of 4 neighbouring sites) uniformly at random, if it has two horizontal (vertical) dimers, flip them to get vertical (horizontal) dimers, otherwise do nothing; repeat many times.

$L \times L$ grid are presented in Fig. 1.2.

The seminal example of dimer models exhibiting the limit shape phenomenon is the dimer covering of the square lattice in the Aztec Diamond shape [2], that is the portion of the two-dimensional square lattice defined by the sites

$$\mathbb{A}_L \equiv \{(i, j) \mid i, j \in \tilde{\mathbb{Z}}, |x| + |y| \leq L\}, \quad (1.1)$$

where $\tilde{\mathbb{Z}} \equiv \mathbb{Z} + \frac{1}{2}$. The Aztec Diamond shape is represented in Fig. 1.3.

The dimer covering of the Aztec Diamond undergoes the limit shape phenomenon when the number of lattice sites goes to infinity while the distance between lattice site decreases so that the overall size of the system stays the same. In particular, there is a spatial separation between four deterministic regions, where one can claim with certainty which type of dimer covers the lattice, and a fluctuating one, where at least two different types of dimers have an associated non-zero occupation probability (see Fig. 1.4). The two types of regions are usually called *frozen* (or *crystalline*) and *liquid* respectively.

For the Aztec Diamond, the limit shape phenomenon takes the form of a theorem, called *Arctic Circle Theorem* [3]): $\forall \epsilon > 0, \exists L \in \mathbb{N}$ such that *almost all* (i.e. with

1.1. LIMIT SHAPE PHENOMENON AND DIMER MODELS

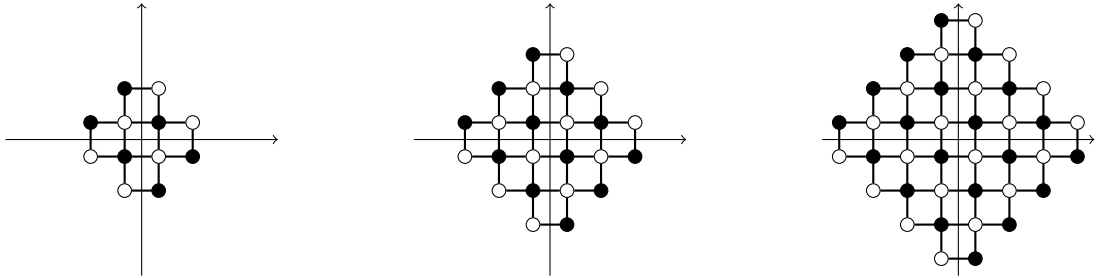


Figure 1.3: Aztec Diamond \mathbb{A}_L for $L = 2, 3, 4$. The lattice sites are coloured in black and white to highlight that the lattice is bipartite.

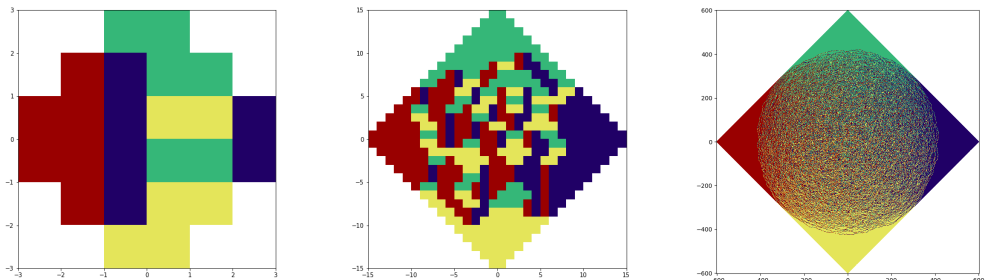


Figure 1.4: Dimer coverings of an Aztec diamond of order L , chosen uniformly at random. The colour code and the Monte Carlo algorithm are the same as in Fig. 1.2. From left to right, $L = 3, 15, 600$. As L increases, dimers appear totally frozen outside a region, whose boundary can be proved to tend uniformly to a circle.

probability $P > 1 - \epsilon$) randomly picked dimer coverings of \mathbb{A}_L have a disordered bulk region whose boundary stays within distance ϵL from the circle of radius $L/\sqrt{2}$. Further investigations of the dimer covering of the Aztec Diamond, such as the description of the interface's fluctuations, can be fund e.g. in [4–6].

To understand the cause of phase separation, imagine to start covering the Aztec Diamond from the bottom corner and to place a vertical dimer. Then, there is just one choice of dimers for a whole side of the Diamond that do not leave any site unoccupied. On the other hand, starting with an horizontal dimer does not constrain any other dimer. Hence, we conclude that there are many more configurations for which the bottom corner is occupied by an horizontal dimer than configurations where the bottom corner is occupied by a vertical dimer. The argument can be iterated, explaining the observation of ordered dimers on the corners.

The Aztec Diamond is an example where the limit shapes phenomenon emerges from two competing instances: on one hand, the parameters of the system are tuned in such a way that at equilibrium the disordered phase should prevail (as observed in the square domain Fig. 1.2); on the other hand, boundary conditions are chosen so that ordered configurations are strongly encouraged in the proximity of the boundary. This induces ordered regions extending macroscopically from the

boundaries deeply inside the bulk of the system. These regions are sharply separated from a central disordered region by the arctic curve.

To conclude this short introduction to limit shapes, let us mention that the phenomenon appears in various topics of Mathematics and Physics, such as, in one dimension, Young diagrams with the Plancherel measure [7] and discrete random matrix models [8]. Other examples are the evaporation of a cubic crystal [9–11], boxed plane partitions [12] and Schur processes [13]. These last examples may all be viewed as dimer models on planar bipartite graphs, for which a general theory has been constructed [14–16]. An interesting connection between limit shape phenomena in such models and the out-of-equilibrium evolution of one-dimensional quantum free-fermion models has been discussed in [17]. Beyond free-fermionic models, limit shapes appear also in Alternating Sign Matrices [18, 19] and in various exactly solvable models of statistical mechanics [20], such as the six-vertex model [21, 22], the stochastic six-vertex model [23] and the twenty-vertex model [24]. Two examples are shown by Fig. 1.5 and Fig. 1.6. In our case, we will focus on the density profile of a fermionic model evolving in imaginary time. In particular, we will observe sharply-separated regions where the density behaves differently. In this case, the term *limit shapes* refers to such non-trivial density profiles. Note however that limit shapes are not, strictly speaking, defined for the density, but for another field, called *height function* [16]; they are however closely connected, the density being essentially the derivative of the height function.

1.2 Free fermions

Alongside the limit shape phenomenon, a main role in our work will be played by free fermions. We focus on fermion models defined on a one-dimensional lattice. For the sake of simplicity, we will first consider the lattice to be finite, with L being the total number of sites.

Recall that a set of (Dirac) *fermionic operators* is a set of linear operators acting on the anti-symmetric Fock space and satisfying the canonical anti-commutation relations:

$$[c_i, c_j^\dagger]_+ = \delta_{ij} \mathbb{I}, \quad [c_i, c_j]_+ = 0, \quad \forall i, j \in \{1, \dots, L\}. \quad (1.2)$$

The c_i 's are called *annihilation operators* and the c_i^\dagger 's are called *creation operators*.

These operators can be constructed explicitly. Here we present a construction due to Jordan and Wigner [29]. For $L = 1$, we introduce the \mathbb{C}^2 basis

$$\{|0\rangle, |1\rangle\} \equiv \left\{ \begin{pmatrix} 0 \\ 1 \end{pmatrix}, \begin{pmatrix} 1 \\ 0 \end{pmatrix} \right\}, \quad (1.3)$$

such that any state can be written as

$$|\psi\rangle = \alpha |0\rangle + \beta |1\rangle, \quad \alpha, \beta \in \mathbb{C}. \quad (1.4)$$

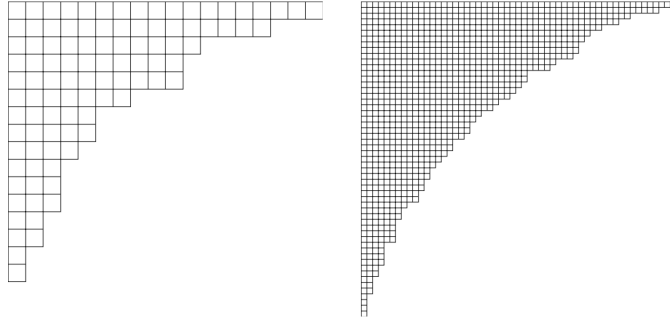


Figure 1.5: Young diagrams of orders $n = 100$ and $n = 1000$ sampled randomly from Plancherel measure. As explained in [25], from which the figure is taken, there exists a correspondence between the Plancherel-random Young diagrams of size n and the uniformly-random permutation of order n . It can be proved that, for $n \rightarrow \infty$, the typical configuration of Young diagrams undergoes the limit shape phenomenon [7]. This can be linked to the famous problem in integrable probability of the longest increasing subsequence in uniformly-random permutation [26, 27].

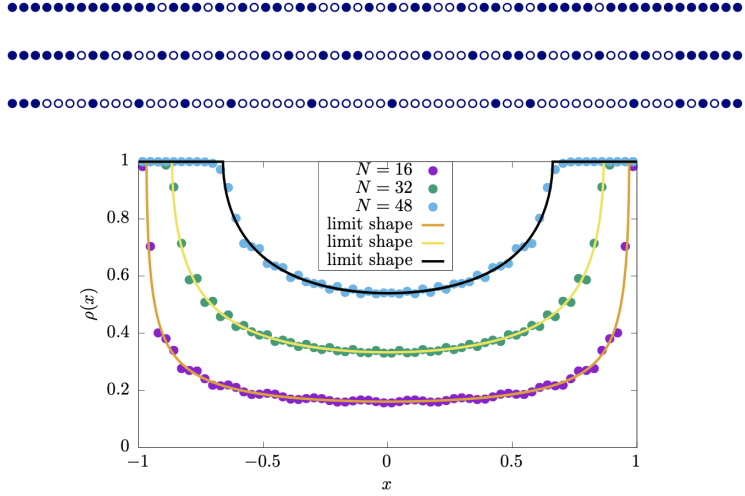


Figure 1.6: Figure taken from [28]. Density profile for N particles on a one-dimensional lattice $\{-1 + \frac{2j}{L-1} | j = 0, 1, \dots, L-1\}$. The particles interact via the 2d Coulomb interaction (logarithmic repulsion). Since we impose that two particles cannot simultaneously occupy the same site, density cannot exceed 1; on the other hand, particles tend to accumulate towards the edges of the box because of the repulsive long-range interaction. The density profile is discussed in [8] and exhibits the limit shape phenomenon. In the figure, $L = 64$.

The state $|0\rangle$ can be interpreted as describing the absence of particles and $|1\rangle$ as describing the presence of a particle. On this space we introduce the operators

$$c = \begin{pmatrix} 0 & 0 \\ 1 & 0 \end{pmatrix} \quad \text{and} \quad c^\dagger = \begin{pmatrix} 0 & 1 \\ 0 & 0 \end{pmatrix}. \quad (1.5)$$

It is easy to check that these two operators satisfy (1.2) for $L = 1$ (though it does not have much sense to talk about fermions with just one particle). Notice that $c^\dagger|0\rangle = |1\rangle$ and $c|1\rangle = |0\rangle$, from which the name of the operators.

If we consider now the tensor product of L copies of the space we have just introduced, a basis is given by all the states

$$|\sigma_1\sigma_2\dots\sigma_L\rangle \equiv |\sigma_1\rangle \otimes |\sigma_2\rangle \otimes \dots \otimes |\sigma_L\rangle, \quad (1.6)$$

where $\sigma_i \in \{0, 1\}$; we call this *position basis* and its elements *position states*. Given a position state, we interpret its 0's as describing empty lattice sites and its 1's as describing occupied lattice sites. For instance, $|0110\rangle$ is the state of a one-dimensional lattice of length $L = 4$ where the second and third sites are occupied and the others are empty.

On this space, we define the operators

$$\begin{aligned} c_1^\dagger &\equiv c^\dagger \otimes \underbrace{\mathbb{I}_2 \otimes \dots \otimes \mathbb{I}_2}_{L-1 \text{ times}} \\ &\dots \\ c_k^\dagger &\equiv \underbrace{\begin{pmatrix} -1 & 0 \\ 0 & 1 \end{pmatrix} \otimes \dots \otimes \begin{pmatrix} -1 & 0 \\ 0 & 1 \end{pmatrix}}_{k-1 \text{ times}} \otimes c^\dagger \otimes \underbrace{\mathbb{I}_2 \otimes \dots \otimes \mathbb{I}_2}_{L-k \text{ times}} \\ &\dots \\ c_L^\dagger &\equiv \underbrace{\begin{pmatrix} -1 & 0 \\ 0 & 1 \end{pmatrix} \otimes \dots \otimes \begin{pmatrix} -1 & 0 \\ 0 & 1 \end{pmatrix}}_{L-1 \text{ times}} \otimes c^\dagger, \end{aligned} \quad (1.7)$$

where the chain of $k - 1$ tensor products of $(-1)^{c^\dagger c}$ is called *Jordan-Wigner string*. By applying the tensor product property $(A \otimes B)(C \otimes D) = AC \otimes BD$, it can be proved that the set containing the operators c_j^\dagger and their adjoints is a set of fermionic operators.

Notice that, defining the *vacuum state* $|0\rangle \equiv \underbrace{|0\rangle \otimes \dots \otimes |0\rangle}_{L \text{ times}}$, the position basis can be built by applying all the possible products of the creation operators. However, since the action on $|0\rangle$ of permutations of the same set of creation operators gives the same state (modulo a sign), we need to decide the order in which the creation operators should be applied, to avoid having a redundancy of generators. The rule

we choose is that the creation operators act from the one with the largest index to the one with the smallest; for example $|1101\rangle = c_1^\dagger c_2^\dagger c_4^\dagger |0\rangle$. Thus, a generic position state reads $|\sigma_1 \sigma_2 \dots \sigma_L\rangle = c_{i_1}^\dagger \dots c_{i_n}^\dagger |0\rangle$, where $\sigma_i \in \{0, 1\}$, $n \leq L$, $i_1 < i_2 < \dots < i_n$ and the indices i_k are those for which $\sigma_{i_k} = 1$.

To conclude this introduction to free fermions, we define a *free model* (or *quadratic model*) a model whose Hamiltonian may be written as quadratic polynomial in the set of fermionic operators. Higher-than-quadratic terms are called *interactions* and the corresponding models are called *interacting*. As we will see in Section 2.1, the property of a theory to be free facilitates its analytic treatment.

For a more detailed introduction to many-particle models, see for instance [30].

1.3 From dimers to imaginary-time fermions

The model we will focus on is a model of fermions in imaginary time. Being the time imaginary, one should link it to a real time physical model or to a statistical mechanics model, to make sense of the quantities that are considered. The connection is usually done via the so called quantum-statistical mechanics correspondence, according to which a $(d + 1)$ -dimensional classical system at the equilibrium can be described as d -dimensional quantum system evolving in imaginary time, see e.g. [31]. Here, following [28], we will show how a dimer model is mapped to fermions and then, thanks to the transfer matrix method, we will show how the various equilibrium quantities of the dimer model can be derived as quantities of the fermion model considered at different imaginary times. Historically, the first solution of the a dimer model is due to [32] and [33], while the first mapping of dimers onto free fermions is due to [34], though the version that is presented here is more in the spirit of [17, 35, 36].

Let us start by considering a portion of the brick wall lattice as the one represented in Fig. 1.7a. Note that this can be viewed as a deformation of the regular hexagonal lattice, but the brick wall shape is more convenient for our purpose. We consider the portion of the lattice to have an odd number of horizontal rows of bricks, with every row containing the same odd number of bricks, and a periodicity every two rows in the vertical direction.

As concerns the boundary conditions of the system, we are interested in the domain wall geometry, which in the present case consists in removing all the lattice sites on the left half of the top and bottom lattice rows and one every two sites in the right half of such rows (cf. Fig 1.7a).

In the end, excluding the top and bottom (incomplete) rows, the lattice portion has size $(2R - 1) \times (2l - 1)$, where $2R - 1$ is the number of internal brick rows and $2l - 1$ is the number of bricks in each row. To fix a coordinate system, we set the origin in the center of the obtained portion.

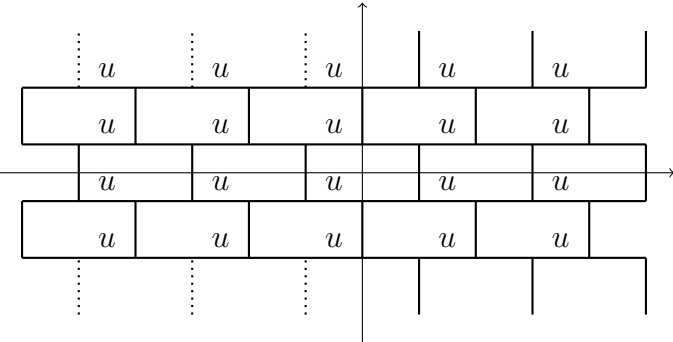
We consider now the dimer coverings of this lattice portion, as defined in Section 1.1. Notice that, in the geometry under consideration, the right half of top and bottom lattice sites can be covered by vertical dimers only, and many sites on the right are consequently constrained to be occupied by vertical dimers. So, as happened with the Aztec Diamond, the particular geometry under consideration has strong influence on macroscopically large regions near the boundaries.

Differently to what was done with the Aztec Diamond, rather than specifying a uniform distribution on the ensemble of dimer configurations, here we introduce some weights in the model. In particular, we associate a real number $u \in (0, 1)$ to one every two horizontal lattice links, as represented in Fig.1.7a. The weight of each dimer covering, modulo a normalization factor, is given by u to the number of weighted lattice links occupied by a dimer.

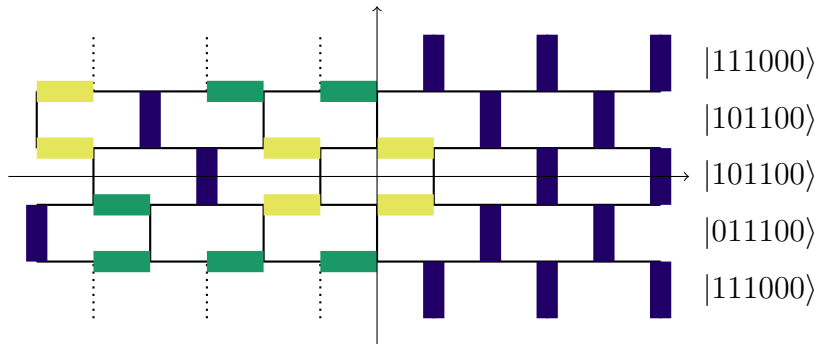
In this construction, we take first the limit $l \rightarrow +\infty$. Then we rescale every distance by R and only at this point we take the limit $R \rightarrow +\infty$. Finally, we end up with a model that has infinite size on the horizontal direction and goes from -1 to +1 in the vertical direction; note that in this limit the model is continuous in both directions. This is what we refer to as *scaling limit*. The model we have just introduced exhibits the limit shape phenomenon in the scaling limit. An illustration of the limit shape that one gets is represented in Fig. 1.7c, where we consider a large-size brick wall lattice before rescaling by R ; the analytic discussion of the problem can be found in [17].

One way to approach this problem is via a mapping to fermions. The peculiarity of this model that makes its mapping to fermions particularly easy is the fact that each of its dimers configuration can be exactly identified just specifying where the vertical dimers are: once the vertical dimers are placed, there is only a way to complete the dimer covering with the other types of dimers. Moreover, the number of vertical dimers is conserved in each of the brick rows. This naturally leads to the mapping to particles: we associate a certain configuration of particles on a one-dimensional lattice to each row of vertical lattice links. In particular, each vertical lattice link will correspond to a lattice site, taken to be occupied by a particle if and only if it is free of dimers. To extend the mapping to the top and the bottom rows, let us imagine that the removed lattice links are still there, but with no dimer on them. We have then that the top and bottom boundaries of the dimer model correspond both to a configuration of particles in which the left half of the lattice is completely occupied by particles and the right half is completely empty. Notice that the number of particles is conserved in each row, as the number of vertical dimers was, and that each lattice-link row corresponds to a configuration of a lattice of length $2l$. An illustration of the mapping to fermions is done in Fig.1.7b.

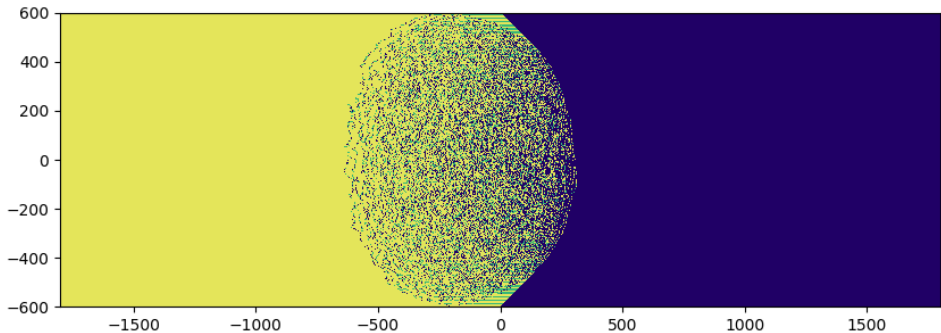
For what concerns the particle statistics, we take them to be fermions, just because we want each lattice site to be occupied by either one or zero particles. In



(a)



(b)



(c)

Figure 1.7: Brick-wall lattice. There are three classes of dimers in this lattice: one vertical dimer (blue in the figure) and two horizontal ones, the first type (green in the figure) occupying weighted lattice links and the other (yellow in the figure) occupying unweighted lattice links. (a) Representation of the weighted brick wall in the domain wall geometry; using conventions defined in the text, the lattice has size $(2R - 1) \times (2l - 1)$, with $l = 3$, $R = 2$. (b) Example of dimer covering for the brick wall in domain wall geometry. Some dimers on the right half of the lattice are forced to be vertical by the boundary conditions. The mapping onto fermion configurations is also shown. (c) Typical configuration for a lattice with $R = 600$ and weight $u = 1/2$, obtained via a Monte Carlo evolution similar to the one used for the Aztec Diamond.

this mapping, particles exchanges will not be involved, so that the anti-commuting nature of fermions is actually not important at this level, if not to impose a hard core constraint on particles.

Suppose now that there exists a $2l \times 2l$ matrix T , called *transfer matrix*, such that, given two configurations of fermions $|C\rangle$ and $|C'\rangle$, $\langle C|T|C'\rangle = u^n$ if the configurations are compatible – meaning they form a valid dimer configuration when stitched together and mapped back onto dimers – and zero otherwise; here n is the number of horizontal dimers occupying weighted lattice links in the configuration. If such a matrix exists, in principle all the interesting quantities of the model can be computed from it. For instance, assuming the states are normalized, we can compute the partition function of the original dimer model as

$$Z = \langle top|T^{2R}|bottom\rangle, \quad (1.8)$$

where $|top\rangle$ and $|bottom\rangle$ are the states corresponding to the top and bottom configurations respectively and $2R+1$ is the total number of fermionic configurations. This is because

$$\langle top|T^{2R}|bottom\rangle = \sum_{C_1, \dots, C_{2R-1}} \langle top|T|C_{2R-1}\rangle \dots \langle C_1|T|bottom\rangle \quad (1.9)$$

and $\langle C_j|T|C_{j-1}\rangle$ gives the weight of the j -th row if the configurations are compatible and zero otherwise, so this just counts the number of dimer coverings compatible with the top and bottom boundary condition, associating to each dimer configuration the proper weight. Similarly, the expectation value of two local observables can be written as

$$\langle top|O_{xy}O_{x'y'}|bottom\rangle = \frac{\langle top|T^{R-y}O_x^\dagger T^{y-y'}O_{x'}T^{R+y}|bottom\rangle}{\langle top|T^{2R}|bottom\rangle}. \quad (1.10)$$

There are actually some subtleties involved here. For instance, the periodicity of the lattice, being every two rows and not every row, implies that one has actually to consider two different transfer matrices, and the expressions we gave are slightly more complicated; for an accurate derivation see [17]. Anyway, it turns out that these formulas are correct if we consider y and R to be very large (that is the limit we are interested in).

In the limit $l \rightarrow +\infty$, the transfer matrix can be shown to be

$$T = \exp \left(- \int_{-\pi}^{+\pi} \frac{dk}{2\pi} \omega(k) d^\dagger(k) d(k) \right), \quad (1.11)$$

with $\omega(k) = -\frac{1}{2} \ln(1 + u^2 + 2u \cos k)$ and

$$\begin{aligned} c_x^\dagger &= \int_{-\pi}^{+\pi} \frac{dk}{2\pi} e^{-ikx} d^\dagger(k), \\ c_x &= \int_{-\pi}^{+\pi} \frac{dk}{2\pi} e^{ikx} d(k). \end{aligned} \tag{1.12}$$

The overall minus sign in the definition of $\omega(k)$ is chosen to make a connection with band theory and have the minimum of $\omega(k)$ in $k = 0$. We presented the transfer matrix already in its diagonalized form; the diagonalization is standard and can be found, for instance, in [37] and [38].

At this point we have a mapping from the brick wall lattice to a one-dimensional model of fermions evolving in discrete imaginary time. As a last step, we take the *Hamiltonian limit*. This limit is done before the scaling limit and consists in substituting first $R \rightarrow pR$, $y \rightarrow py$, $u \rightarrow 1/p$ and then taking the limit $p \rightarrow +\infty$. Since the original y was an integer, the new y takes discrete values separated by steps of $1/p$. It is clear, then, that in the Hamiltonian limit y takes continuous values from $-R$ to $+R$. An illustration of the Hamiltonian limit is given in Fig.1.8.

In this limit, the expression for the expectation value becomes

$$\langle top | O_x(y) O_{x'}(y') | bottom \rangle = \frac{\langle top | e^{-(R-y)H_0} O_x^\dagger e^{-(y-y')H_0} O_{x'} e^{-(R+y)H_0} | bottom \rangle}{\langle top | e^{-2RH_0} | bottom \rangle}, \tag{1.13}$$

with

$$H_0 \equiv \int_{-\pi}^{+\pi} \frac{dk}{2\pi} \epsilon(k) d^\dagger(k) d(k) \equiv \int_{-\pi}^{+\pi} \frac{dk}{2\pi} (-\cos k) d^\dagger(k) d(k). \tag{1.14}$$

Using the notation $O(\tau) = e^{\tau H} O e^{-\tau H}$, the expectation value that we wrote can be interpreted as the expectation value of two local operators associated to a one dimensional lattice and evolving in continuous imaginary time. However, it should be pointed out that the R at the exponent breaks the perfect parallelism with the evolution in real time, since it is not present in the definition of the two-point function in the real time problem.

Summarizing, we have mapped the problem of the dimer covering of the brick wall lattice in the Hamiltonian limit onto a system of fermions on a one dimensional lattice evolving in continuous imaginary time, whose expectation values are defined as in (1.13). The limit shapes of the dimer model can now be studied by looking at quantities of the fermion model such as the particle density.

As a final remark, we recognize in (1.14) the same Hamiltonian describing the XX quantum spin chain, modulo a Jordan-Wigner transformation; the Jordan-Wigner transformation for the XX-chain is treated for instance in [39], while more general

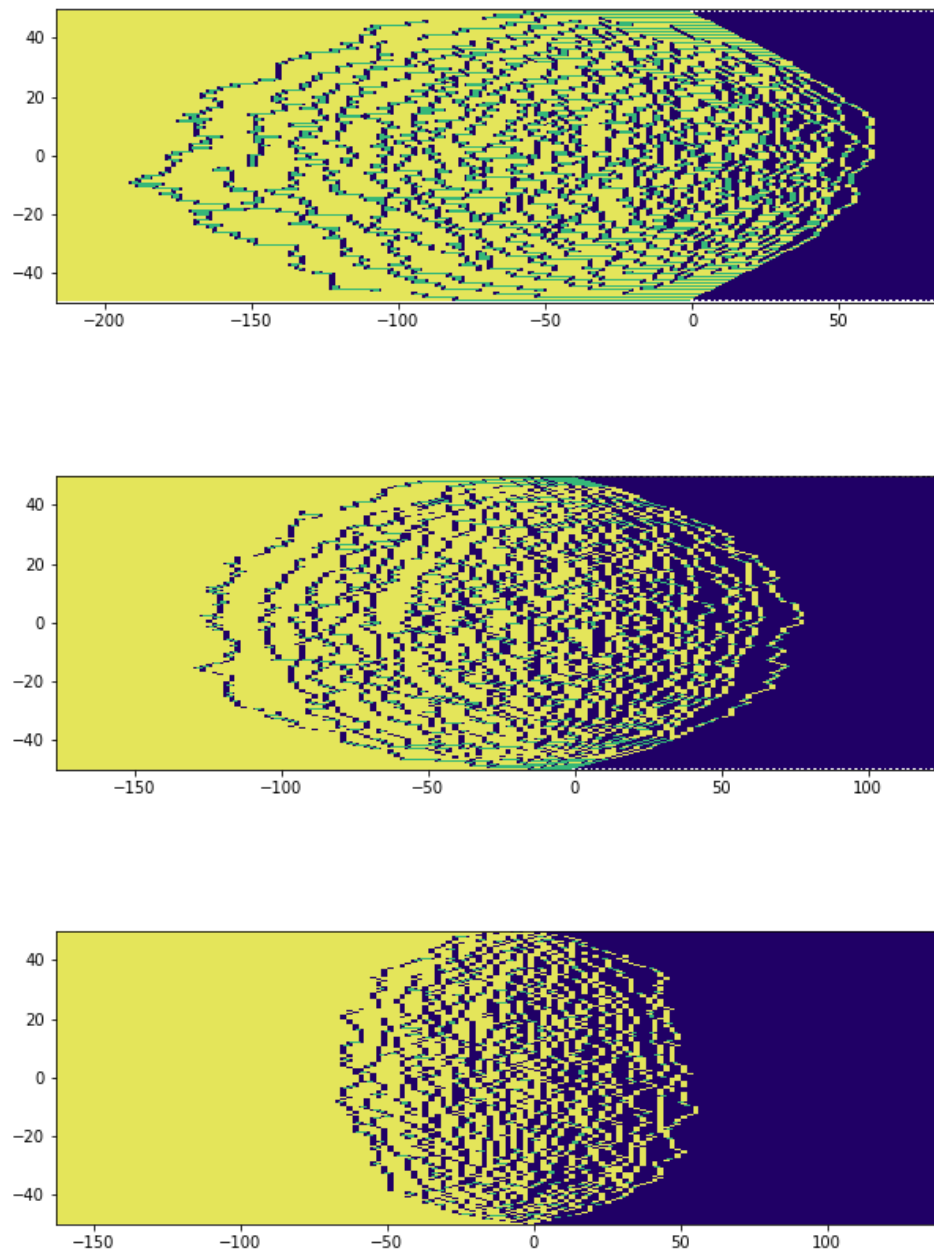


Figure 1.8: Illustration of the Hamiltonian limit for dimers on the brick-wall lattice. From top to bottom, $p = 2, 4, 8$. The horizontal axis reports the position x inside the lattice, while the vertical axis reports the (still discrete) imaginary time y , after the rescaling by a factor p has been done. In this limit the vertical direction becomes continuous and the arctic curve converges to a circle centred in the origin. The scale on the horizontal axis is the same in the three pictures, but it is shifted in order to center the limit shape. The colour code is the same of Fig. 1.7.

applications of transformation can be found in [40]; the general theory of spin and fermion chains can be found for instance in [41].

1.4 Our model

1.4.1 Definition

In the previous section we saw how a statistical mechanics model can be solved looking at a particular model of fermions in imaginary time, with a certain definition of the two-point function. Thanks to that mapping, quantities such as the density of the fermion model assume a probabilistic meaning. In our work, we start directly from a more general fermion model and investigate the limit shape phenomenon in this case. As we will see, the impossibility of doing the reverse procedure and obtain a statistical model from our general model of fermions will lead to an *ill-definition* of the density.

We work with a model of free fermions on lattice, assuming the lattice to be along the x -axis in such a way that the sites occupy the positions $\tilde{\mathbb{Z}} \equiv \mathbb{Z} + \frac{1}{2}$. We then consider the evolution of the system in imaginary time, taking the time axis to be the y -axis, and imposing that the evolution is ruled by a certain Hamiltonian H ; what we mean by evolution here will be clear when we will define the two-point correlation function. Notice that we are working in an intermediate situation between continuous and discrete, since the values on the x -axis are discrete and the values on the y -axis are continuous.

We initially consider the problem in the *domain wall geometry*, that is we impose the initial (imaginary time $y = -R$) and final state (imaginary time $y = +R$) to refer both to the configuration in which all the negative lattice sites are occupied and all the positive ones are empty (see Fig.1.9). We will identify the state corresponding to such configuration as $|\psi_1\rangle$ (where the 1 is present for future generalization). In the language of fermionic operators, it is the state such that

$$\rho_x |\psi_1\rangle = c_x^\dagger c_x |\psi_1\rangle = \Theta(-x) |\psi_1\rangle, \quad \forall x \in \tilde{\mathbb{Z}}, \quad (1.15)$$

where Θ is the Heaviside step function.

We finally define the fundamental object of our work, i.e. the two-point correlation function, as

$$\begin{aligned} \langle \psi_1 | c_x^\dagger(y) c_{x'}(y') | \psi_1 \rangle_R &\equiv \frac{\langle \psi_1 | e^{-HR} c_x^\dagger(y) c_{x'}(y') e^{-HR} | \psi_1 \rangle}{\langle \psi_1 | e^{-2HR} | \psi_1 \rangle} \\ &\equiv \frac{\langle \psi_1 | e^{-H(R-y)} c_x^\dagger e^{-H(y-y')} c_{x'} e^{-H(R+y')} | \psi_1 \rangle}{\langle \psi_1 | e^{-2HR} | \psi_1 \rangle}, \end{aligned} \quad (1.16)$$

The interest in this quantity is motivated by the mapping from the statistical problem we saw above and because it is one of the quantities of interest in quantum

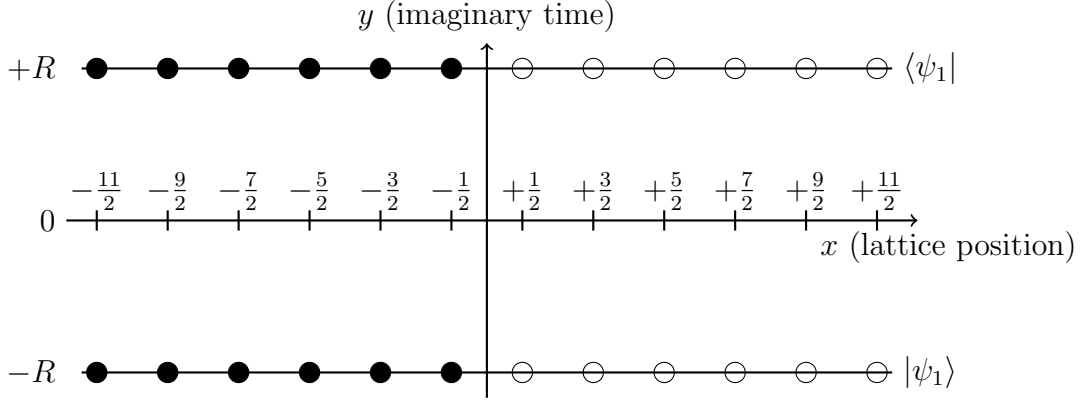


Figure 1.9: Representation of our model of fermions. The model is a chain of fermions hopping on the lattice $\tilde{\mathbb{Z}}$ in the domain wall geometry, in which the initial and final states are completely filled on the left, and completely empty on the right.

quenches literature, see e.g. [42–45]. Notice also that, if we formally take $R = 0$ and $y = it$, we get the usual definition of the two-point function in real time; this is actually the starting point for some techniques studying inhomogeneous real-time evolution.

For the evolution, we consider an Hamiltonian with nearest-neighbour and next-nearest-neighbour hoppings terms only (NN hopping and NNN hopping respectively):

$$\begin{aligned} H_\alpha &= -\frac{1}{2} \sum_{x \in \tilde{\mathbb{Z}}} \left((c_{x+1}^\dagger c_x + c_x^\dagger c_{x+1}) + \alpha(c_{x+2}^\dagger c_x + c_x^\dagger c_{x+2}) \right) \\ &= \int_{-\pi}^{+\pi} \frac{dk}{2\pi} \epsilon(k) d^\dagger(k) d(k), \end{aligned} \quad (1.17)$$

where $\epsilon(k) \equiv -\cos(k) - \alpha \cos(2k)$ is referred to as the *dispersion relation* and $d(k)$ and $d^\dagger(k)$ are defined as above (see (1.12)).

In fact, even though this is the Hamiltonian we have in mind, some of our results extend to a much more general family of quadratic Hamiltonians.

1.4.2 Symmetries of the density profile

We will be interested mainly in the density profile of the model, obtained by the two-point correlation function (1.16) setting $x = x'$ and $y = y'$. The best way to familiarize with it is to look at its symmetries. Beside being useful in the following, they can already provide intuition about what we are facing.

Time reflection

Any combination of creation and destruction operators acting on a linear combination of position states with real coefficients gives in general another linear combination of position states, whose coefficients are still real. This means that the two point function is a real scalar number, from which we have

$$\langle \psi_1 | e^{-(R-y)H_\alpha} c_x^\dagger c_x e^{-(R+y)H_\alpha} | \psi_1 \rangle^\dagger = \langle \psi_1 | e^{-(R+y)H_\alpha} c_x^\dagger c_x e^{-(R-y)H_\alpha} | \psi_1 \rangle.$$

This immediately implies

$$\rho_x(y) = \rho_x(-y), \quad (1.18)$$

i.e. that the density profile is symmetric by time reflection.

Particle-hole symmetry

Let us consider the expectation value of the hole density $\rho_x^h \equiv 1 - c_x^\dagger c_x$:

$$\langle \psi_1 | \rho_x^h(y) | \psi_1 \rangle_R = \frac{\langle 0 | c_{-\frac{1}{2}} \dots c_{-l+\frac{1}{2}} e^{(y-R)H_\alpha} (1 - c_x^\dagger c_x) e^{-(y+R)H_\alpha} c_{-l+\frac{1}{2}}^\dagger \dots c_{-\frac{1}{2}}^\dagger | 0 \rangle}{\langle 0 | c_{-\frac{1}{2}} \dots c_{-l+\frac{1}{2}} e^{-2RH_\alpha} c_{-l+\frac{1}{2}}^\dagger \dots c_{-\frac{1}{2}}^\dagger | 0 \rangle}. \quad (1.19)$$

First of all, notice that, if we reflect the boundary states with respect to the y axis, ρ_{-x} equals ρ_x in original conditions: it just corresponds to inverting the direction of the x -axis and a change in the coordinates system cannot alter the predictions. Hence we can write

$$\langle \psi_1 | \rho_x^h(y) | \psi_1 \rangle_R = \frac{\langle 0 | c_{\frac{1}{2}} \dots c_{l-\frac{1}{2}} e^{(y-R)H_\alpha} (1 - c_{-x}^\dagger c_{-x}) e^{-(y+R)H_\alpha} c_{l-\frac{1}{2}}^\dagger \dots c_{\frac{1}{2}}^\dagger | 0 \rangle}{\langle 0 | c_{\frac{1}{2}} \dots c_{l-\frac{1}{2}} e^{-2RH_\alpha} c_{l-\frac{1}{2}}^\dagger \dots c_{\frac{1}{2}}^\dagger | 0 \rangle}. \quad (1.20)$$

Now let us change point of view and introduce the *fermionic hole operators*:

$$c_x^\dagger = h_x, \quad c_x = h_x^\dagger, \quad |0\rangle = \left(\prod_{x \in \mathbb{Z}} h_x^\dagger \right) |0_h\rangle. \quad (1.21)$$

The expectation value pf ρ^h now reads

$$\langle \psi_1 | \rho_x^h(y) | \psi_1 \rangle_R = \frac{\langle 0_h | h_{-\frac{1}{2}} \dots h_{-l+\frac{1}{2}} e^{(y-R)H_\alpha} h_{-x}^\dagger h_{-x} e^{-(y+R)H_\alpha} h_{-l+\frac{1}{2}}^\dagger \dots h_{-\frac{1}{2}}^\dagger | 0_h \rangle}{\langle 0_h | h_{-\frac{1}{2}} \dots h_{-l+\frac{1}{2}} e^{-2RH_\alpha} h_{-l+\frac{1}{2}}^\dagger \dots h_{-\frac{1}{2}}^\dagger | 0_h \rangle}. \quad (1.22)$$

As for the Hamiltonian, when it is written in function of the fermionic hole operators, it maintains its form, changing just the overall sign:

$$H_\alpha = +\frac{1}{2} \sum_{x \in \mathbb{Z}} \left((h_{x+1}^\dagger h_x + h_x^\dagger h_{x+1}) + \alpha (h_{x+2}^\dagger h_x + h_x^\dagger h_{x+2}) \right) \quad (1.23)$$

As the original Hamiltonian of the model, this new Hamiltonian can also be diagonalized going to the momentum basis. This time, though, we choose a different convention to define momentum basis, and we take

$$h_x^\dagger = \int_0^{+2\pi} \frac{dk}{2\pi} e^{-ikx} f^\dagger(k) = \int_{-\pi}^{+\pi} \frac{dk}{2\pi} e^{-i(k+\pi)x} f^\dagger(k + \phi), \quad (1.24)$$

$$h_x = \int_0^{+2\pi} \frac{dk}{2\pi} e^{ikx} f(k) = \int_{-\pi}^{+\pi} \frac{dk}{2\pi} e^{i(k+\pi)x} (k + \phi). \quad (1.25)$$

With these conventions we have

$$\frac{1}{2} \sum_x (h_x^\dagger h_{x+a} + h_{x+a}^\dagger h_x) = \int_{-\pi}^{+\pi} \frac{dq}{2\pi} \cos(a(q + \pi)) f^\dagger(q + \pi) f(q + \pi) \quad (1.26)$$

$$\Rightarrow H_\alpha = \int_{-\pi}^{+\pi} \frac{dq}{2\pi} (-\cos(q) + \alpha \cos(2q)) f^\dagger(q + \pi) f(q + \pi). \quad (1.27)$$

As the last change of notation we take $g(q) = f(q + \pi)$ and, using

$$h_x^\dagger h_x = \int_{-\pi}^{+\pi} \frac{dq dp}{(2\pi)^2} e^{ix(p-q)} f^\dagger(q + \pi) f(p + \pi) = \int_{-\pi}^{+\pi} \frac{dq dp}{(2\pi)^2} e^{ix(p-q)} g^\dagger(q) g(p), \quad (1.28)$$

we find

$$\langle \psi_1 | \rho_x^h(y) | \psi_1 \rangle_R = \frac{\langle 0_h | h_{-\frac{1}{2}} \dots h_{-l+\frac{1}{2}} e^{(y-R)H_\alpha} \left(\int_{-\pi}^{+\pi} \frac{dq dp}{(2\pi)^2} e^{-ix(p-q)} g^\dagger(q) g(p) \right) e^{-(y+R)H_\alpha} h_{-l+\frac{1}{2}}^\dagger \dots h_{-\frac{1}{2}}^\dagger | 0_h \rangle}{\langle 0_h | h_{-\frac{1}{2}} \dots h_{-l+\frac{1}{2}} e^{-2RH_\alpha} h_{-l+\frac{1}{2}}^\dagger \dots h_{-\frac{1}{2}}^\dagger | 0_h \rangle},$$

with

$$H_\alpha = \int_{-\pi}^{+\pi} \frac{dq}{2\pi} (-\cos(q) + \alpha \cos(2q)) g^\dagger(q) g(q). \quad (1.29)$$

So far we did not make any transformation: we just rewrote the expectation value of the hole density in a new notation. Now notice that, taking $x \rightarrow -x$ and $\alpha \rightarrow -\alpha$, we find that the expression of $\langle \psi_1 | \rho_x^h(y) | \psi_1 \rangle_R$ is formally identical to $\langle \psi_1 | \rho_x(y) | \psi_1 \rangle_R$, so we can conclude that the system is symmetrical if we invert the roles of particles and holes, modulo reflecting the system with respect to the vertical axis and exchanging the sign of the NNN hopping term.

Conservation of the number of particles

This conservation law simply follows from the fact that the number operator $N = \sum_{i \in \mathbb{Z}} c_i^\dagger c_i$ commutes with the Hamiltonian:

$$\begin{aligned} [c_j^\dagger c_{j+a}, N] &= \sum_i \left([c_j, c_i^\dagger c_i] c_{j+a} + c_j^\dagger [c_{j+a}, c_i^\dagger c_i] \right) \\ &= \sum_i \left(-\delta_{ij} c_j^\dagger c_{j+a} + \delta_{i,j+1} c_j^\dagger c_{j+1} \right) = 0, \end{aligned}$$

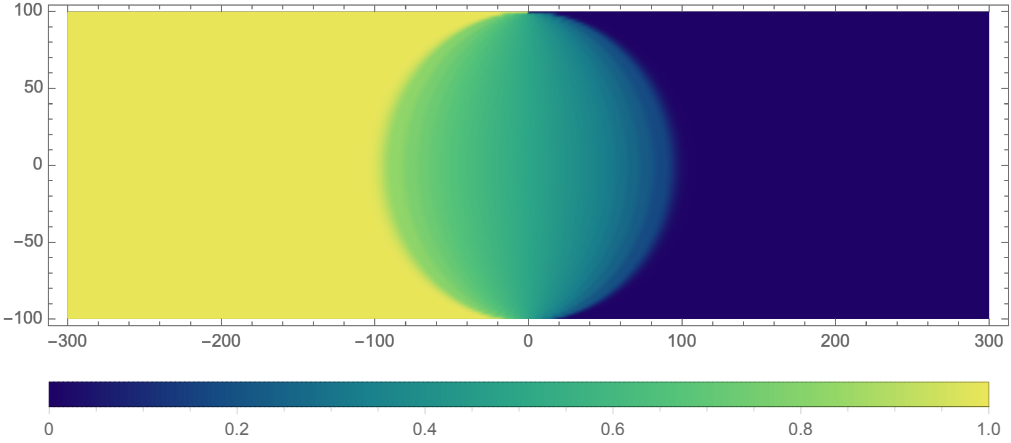


Figure 1.10: Density profile for the the fermion chain with NN hopping in domain wall geometry. The model exhibits the limit shape phenomenon; in this particular case the arctic curve is a circle. The procedure this profile was obtained will be explained in Section 3.4.

where we used

$$[A, BC] = [A, B]_+ C - B[A, C]_+. \quad (1.30)$$

This means that any application of the Hamiltonian cannot change the total number of particles, hence the total number of particles is constant in time.

1.4.3 Pure nearest-neighbour hopping limit

The case $\alpha = 0$ gives back the Hamiltonian (1.14) and, because of its connections to statistical models, deserves to be analysed on its own. This case has been already studied and many results about it are known [17]. For instance, the model is known to exhibit the limit shape phenomenon, the arctic curve being a circle. The density profile in the scaling limit has a frozen deterministic region, where the density is either zero or one and a fluctuating region, where the density is between zero and one. We will provide a detailed proof of the arctic curve in Section 4.2, after the necessary theoretical tools will have been introduced, but in Fig.1.10 we anticipate the density profile, to give an idea of what we are dealing with.

Here we are only interested in the density profile, but let us mention that the study of this model proceeded further. For instance, in [17] it is proven that large-scale correlations inside the critical region are expressed in terms of correlators in a (euclidean) two-dimensional massless Dirac field theory, which is observed to be inhomogeneous, that is to have a position-dependent metric (so it is in fact a Dirac theory in curved space).

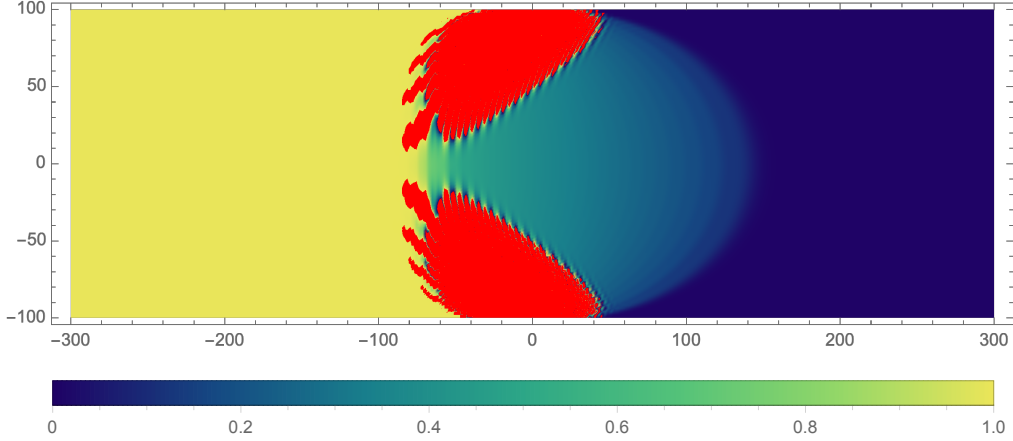


Figure 1.11: Density profile for our fermion model with $\alpha = 1/4$. The red-shaded regions represent the regions where the density is not well-defined. The procedure this profile was obtained will be explained in Section 3.4.

1.4.4 The density problem

Our model with H_α , for general values of α , lacks one of the greatest features of the $\alpha = 0$ case: it is not linked to any statistical mechanic model. This prevents us to interpret a priori the density that is inferred from the two-point function (1.16) as some kind of probability distribution or even a density in the usual meaning. Indeed, what we usually call *density* is a quantity defined between zero and one, which is a property that is not guaranteed for our density; when our density is between zero and one, we say that it is *well-defined* (*ill-defined* otherwise). As it turns out already from numerical simulations, the density of our model is ill-defined in some regions (see Fig. 1.11). We are interested in studying how the ill-definition of the density manifests itself in the scaling limit. More precisely, we are interested in finding a rule to identify those points x, y for which the density is not well-defined and characterize the limit shapes that those regions exhibit. This is what we call the *density problem*.

Since for $\alpha = 0$ we have a well defined density, the possible cause of the ill-definition of the density must be related to the NNN hopping. So let us examine what features the NNN hopping brings in that were not there with NN hopping only.

Let us start considering the sign of the density. The denominator is always positive, since

$$\langle \psi_1 | e^{-2RH_\alpha} | \psi_1 \rangle = \| e^{-RH_\alpha} | \psi_1 \rangle \|^2, \quad (1.31)$$

so

$$\text{sign}\left(\langle \psi_1 | \rho_x(y) | \psi_1 \rangle_R\right) = \text{sign}\left((e^{-(R-y)H_\alpha} | \psi_1 \rangle)^\dagger (c_x^\dagger c_x e^{-(R+y)H_\alpha} | \psi_1 \rangle)\right). \quad (1.32)$$

In fact, the term $c_x^\dagger c_x$, acting on a linear combination of position states, cannot change the sign of any coefficient: being nothing but the occupation operator of the site x , it just multiplies each component either by one or zero. So in the end

$$\text{sign}\left(\langle\psi_1|\rho_x(y)|\psi_1\rangle_R\right) = \text{sign}\left((e^{-(R-y)H_\alpha}|\psi_1\rangle)^\dagger(e^{-(R+y)H_\alpha}|\psi_1\rangle)\right). \quad (1.33)$$

We are interested in the application of all the possible powers of the Hamiltonian to a generic states (they come from the expansion of the exponential). A first trivial observation is that if the application of the Hamiltonian to all the possible position states gave a linear combination of position states whose coefficients were all positive, then, given the orthogonality of the states, the product $(e^{-(R-y)H_\alpha}|\psi\rangle)^\dagger(e^{-(R+y)H_\alpha}|\psi\rangle)$ would just be a sum of positive terms, and hence it would be positive. But this does not happen in our case.

Let us consider $\alpha = 0$ and discuss what are the consequences of the application of $(\frac{R\pm y}{2}H_0)^n = (\frac{R\pm y}{2}\sum_i(c_i^\dagger c_{i+1} + c_{i+1}^\dagger c_i))^n$, $\forall n \in \mathbb{N}$, to the generic state $|\psi\rangle$. A fact that comes in handy is that the coefficients $\frac{R\pm y}{2}$ are always positive, so we can just restrict our attention to the sign given by the application of $(\sum_i(c_i^\dagger c_{i+1} + c_{i+1}^\dagger c_i))^n$. The application of this Hamiltonian to any positive-coefficients linear combination of states gives another (possibly the same) positive-coefficients linear combination: $c_{i+1}^\dagger c_i$ gives zero if applied to a position state that does not involve c_i^\dagger , while substitutes c_i^\dagger with c_{i+1}^\dagger if c_i^\dagger is present (an analogous thing holds for $c_i^\dagger c_{i+1}$). In physical terms, we say that the number of fermions is kept constant and the fermions cannot jump over each other so they keep the initial order. So, in the end, the scalar product for the density is taken between two generally different linear combination of position states with positive coefficients; hence it gives a positive density for every y .

On the other hand, if we consider the NNN hopping, it is not true anymore that the application of the Hamiltonian to a general positive-coefficients linear combination of position states gives another positive-coefficients state. This is easily understood from the following example:

$$(c_{1+2}^\dagger c_1)|1100\rangle = (c_3^\dagger c_1)c_1^\dagger c_2^\dagger|0000\rangle = c_3^\dagger c_2^\dagger|0000\rangle = -c_2^\dagger c_3^\dagger|0000\rangle = -|0110\rangle. \quad (1.34)$$

In physical language, the NNN hopping allows fermions to jump over each other and hence, in doing so, to exchange their position. The position exchanging generates a minus sign due to the fermionic nature of the particles. Of course, this does not necessarily imply a negative output: if the components of $e^{-(R+y)H_\alpha}|\psi_1\rangle$ with a negative coefficient were the same in $e^{-(R-y)H_\alpha}|\psi_1\rangle$, then the minus signs would compensate each other in the full product (1.33). But this is not the case, since the same component can be generated from the same initial state with different signs:

consider for example

$$|1100\rangle \rightarrow |1010\rangle \rightarrow |0110\rangle , \quad (1.35)$$

$$|1100\rangle \rightarrow -|0110\rangle . \quad (1.36)$$

We conclude that there is nothing guaranteeing that the density is positive in the general case.

For what concerns the density being greater than one, we could apply the same arguments we just did to the hole density and then use the symmetry particles-holes, noticing that a negative hole density precisely implies a particle density greater than one.

Notice that, as implied by this arguments, problems in density arise due to the non-trivial signs introduced by fermions jumping over each other, so one can think to remove the density problem by diminishing the initial (and final) density of fermions. This will lead us, later on, to consider a generalization of the domain wall geometry.

1.4.5 Cases with well-defined density

Before tackling the density problem from an analytic point of view, it is useful to identify two situations in which the density is well defined even in presence of the NNN hopping term. This will provide a first check for the theoretical prediction that we shall make.

Horizontal axis

To show that the density is positive for $y = 0$, we simply rewrite it as the norm of a certain state:

$$\rho(x, y = 0) = \frac{\langle \psi_1 | e^{-RH_\alpha} c_x^\dagger c_x e^{-RH_\alpha} | \psi_1 \rangle}{\langle \psi_1 | e^{-2RH_\alpha} | \psi_1 \rangle} = \frac{\|c_x e^{-RH_\alpha} | \psi_1 \rangle\|^2}{\|e^{-RH_\alpha} | \psi_1 \rangle\|^2} \geq 0. \quad (1.37)$$

Then we can use the particle-hole symmetry to imply that it is also smaller than one: the density of particles is smaller than one if and only if the density of holes is positive, and to prove that the hole density is positive we can just employ the same trick we used above.

Note that this is true for any Hermitian Hamiltonian, but it does not hold for general imaginary time y .

Pure NNN hopping

Consider the Hamiltonian

$$H' \equiv -\frac{1}{2} \sum_{x \in \mathbb{Z}} \left(c_{x+2}^\dagger c_x + c_x^\dagger c_{x+2} \right). \quad (1.38)$$

Moving by steps of two sites each, one fermion that begins in the site $x \in \tilde{\mathbb{Z}}$ can end up just in sites $x + 2j$, with $j \in \mathbb{Z}$. So the lattice can be divided into two sub-lattices, described by the sites $i + \frac{1}{2}$, with i odd and even respectively, and the fermions into two classes, according to which sub-lattice they move within. The key-observation is that the order of fermions in each class does not change, in the sense that they cannot jump over each other.

Now consider any position state and look at it as obtained from a certain initial position state through a certain number of applications of the NNN hopping (to make this possible, the two states must have the same number of fermions in odd and even lattice sites). The relative sign between the two states is given by -1 to the differences in the alternation of fermions in odd and even lattice sites, so the coefficient will not be necessarily positive. But the fundamental point is that there is a unique way to reach one given final state, and this is because the order of the particles inside the two sub-lattices cannot change (and particles cannot change sub-lattice). So, provided that we start from the same initial state, the coefficient's sign of any component on the position basis is uniquely determined and always the same. In the end, this means that the minus signs will compensate each other in the full product (1.33), thus leading to a positive density.

Again, since this argument holds for the hole density as well and the particle density is smaller than one if and only if the hole density is positive, we conclude that the density for NNN hopping is between zero and one.

When considering the full Hamiltonian H_α , the argument we gave is not true anymore because the distinction between two (or more) ordering-preserving classes of fermions is not possible anymore.

CHAPTER 1. INTRODUCTION

Chapter 2

The Tools

2.1 Free fermions' techniques

2.1.1 Some useful properties

In Section 1.2 we recalled that a set of fermionic operators defined for a lattice obeys the canonical anti-commutation relations

$$\begin{aligned} [c_i^\dagger, c_j]_+ &= \delta_{ij}, \\ [c_i, c_j]_+ &= 0, \\ [c_i^\dagger, c_j^\dagger]_+ &= 0, \end{aligned} \tag{2.1}$$

for all $i, j \in \{1, \dots, L\}$, where L is the number of lattice sites. Then we introduced the *vacuum state* $|0\rangle$ as the state that is annihilated by all the annihilation operators: $c_i |0\rangle = 0, \forall i \in \{1, \dots, L\}$. In the following, we assume that it is normalized.

We also defined a *free*, or *quadratic*, lattice fermion theory as a quantum many-body system ruled by a Hamiltonian that can be written as a quadratic polynomial in the fermionic operators. The (Hermitian) Hamiltonian of a free theory thus reads

$$H = \sum_{i,j=1}^L \left(A_{ij} c_i^\dagger c_j + B_{ij}^* c_i^\dagger c_j^\dagger + B_{ij} c_i c_j \right), \tag{2.2}$$

where A is Hermitian. We are ignoring the irrelevant constant term, since it would just shift every energy level by the same amount, and we are considering that linear terms can be absorbed in bilinear ones by a redefinition of the fermionic operators.

When we restrict to models whose evolution conserve the number of particles (i.e. whose Hamiltonian commutes with the number operator $\sum_{i=1}^L c_i^\dagger c_i$), the most general free Hamiltonian is

$$H = \sum_{i,j=1}^L A_{ij} c_i^\dagger c_j, \tag{2.3}$$

where A is Hermitian. We will consider only this type of systems, since our model's Hamiltonian (1.17) belongs to this class.

Thanks to the spectral theorem, we know that the matrix A can be diagonalized by the means of an orthonormal basis. The eigenvalue equations read (assume no multiplicities for simplicity)

$$\sum_{j=1}^L A_{ij} u_j^{(k)} = \epsilon_k u_i^{(k)}, \quad \forall i, k \in \{1, \dots, L\}, \quad (2.4)$$

with the eigenvectors satisfying the orthonormality equation

$$\sum_{j=1}^L u_j^{(k)} u_j^{(q)} = \delta_{kq}, \quad \forall k, q \in \{1, \dots, L\}. \quad (2.5)$$

This allows also to rewrite the Hamiltonian in its diagonalized form, that is as a sum of occupation number operators multiplied by the respective single-particle energies ϵ_k : introducing the operators

$$d_k^\dagger \equiv \sum_{j=1}^L u_j^{(k)} c_j^\dagger, \quad d_k \equiv \sum_{j=1}^L \left(u_j^{(k)}\right)^* c_j, \quad k \in \{1, \dots, L\}, \quad (2.6)$$

we have

$$H = \sum_{k=1}^L \epsilon_k d_k^\dagger d_k. \quad (2.7)$$

The following property of the diagonalized Hamiltonian will prove itself very useful when we will consider the imaginary-time evolution of fermionic operators:

$$e^{\tau d_i^\dagger d_i} d_j^\dagger e^{-\tau d_i^\dagger d_i} = e^{\tau \delta_{ij}} d_i^\dagger, \quad (2.8)$$

where δ_{ij} is the Kronecker symbol.

Proof. It is a direct consequence of the canonical anti-commutation relations. For a start, notice that, due to the idempotence of the operator $d_i^\dagger d_i$ (that stems directly from the canonical anti-commutation relations), we have

$$e^{\tau d_i^\dagger d_i} = \sum_{n=0}^{\infty} \frac{(\tau d_i^\dagger d_i)^n}{n!} = 1 + \sum_{n=1}^{\infty} \frac{\tau^n d_i^\dagger d_i}{n!} = 1 + (e^\tau - 1) d_i^\dagger d_i. \quad (2.9)$$

Hence we obtain

$$e^{\tau d_i^\dagger d_i} d_j^\dagger e^{-\tau d_i^\dagger d_i} = \left(1 + (e^\tau - 1) d_i^\dagger d_i\right) d_j^\dagger \left(1 + (e^\tau - 1) d_i^\dagger d_i\right), \quad (2.10)$$

and now it is just a matter of computing the product and using again the idempotence of $d_i^\dagger d_i$ to get the assertion. □

As a simple application of the previous property, we have

$$e^{\sum_i \tau_i d_i^\dagger d_i} e^{-\sum_i \tau_i d_i^\dagger d_i} = e^{\tau_j} d_j^\dagger. \quad (2.11)$$

We will be mostly interested in a free fermion theory defined on an infinite lattice. This means that the indices of our set of fermionic operators c_i, c_i^\dagger will take values over an infinite set: rather than $i \in \{1, \dots, L\}$, we use $i \in \tilde{\mathbb{Z}}$. The canonical anti-commutation relations between these operators are still described by eq. (2.1). If the Hamiltonian is translational invariant (meaning that it is invariant by a shift of all the lattice indices), as will always be the case in the models we are interested in, it can be diagonalized by the means of Fourier series, going to what we will call *momentum basis* $\{d(k), d^\dagger(k)\}_{k \in [-\pi, \pi]}$. The momentum basis is defined by

$$\begin{aligned} c_x^\dagger &= \int_{-\pi}^{+\pi} \frac{dk}{2\pi} e^{-ikx} d^\dagger(k), \\ c_x &= \int_{-\pi}^{+\pi} \frac{dk}{2\pi} e^{ikx} d(k). \end{aligned} \quad (2.12)$$

Indeed we have

$$\begin{aligned} H &= \sum_{m,n \in \mathbb{Z}} f(m-n) c_{m+\frac{1}{2}}^\dagger c_{n+\frac{1}{2}} \\ &= \sum_{n,r \in \mathbb{Z}} f(r) \int_{-\pi}^{+\pi} \frac{dp}{2\pi} \int_{-\pi}^{+\pi} \frac{dq}{2\pi} e^{-i(r+n+\frac{1}{2})p} d^\dagger(p) e^{i(n+\frac{1}{2})q} d(q) \\ &= \int_{-\pi}^{+\pi} \frac{dp}{2\pi} \epsilon(p) e^{-i(r+n)p} d^\dagger(p) d(p), \end{aligned} \quad (2.13)$$

where we used the Dirac comb representation $\sum_{s \in \mathbb{Z}} \delta(k - 2\pi s) = \frac{1}{2\pi} \sum_{n \in \mathbb{Z}} e^{ikn}$ and we defined the *dispersion relation* as $\epsilon(p) \equiv \sum_{r \in \mathbb{Z}} f(r) e^{irp}$. It can be shown that the canonical anti-commutation relations (2.1) imply the following algebra for the momentum-basis operators:

$$\begin{aligned} [d(k)^\dagger, d(k')]_+ &= 2\pi \delta(k - k'), \\ [d(k), d(k')]_+ &= 0, \\ [d^\dagger(k), d^\dagger(k')]_+ &= 0, \end{aligned} \quad (2.14)$$

$\forall k, k' \in [-\pi, +\pi]$. We call them *canonical anti-commutation relations* as well.

For these operators, it can be proved that

$$e^{\int_{-\pi}^{+\pi} \frac{dk}{2\pi} \tau(k) d^\dagger(k) d(k)} d^\dagger(q) e^{-\int_{-\pi}^{+\pi} \frac{dk}{2\pi} \tau(k) d^\dagger(k) d(k)} = e^{\tau(q)} d^\dagger(q), \quad (2.15)$$

which is a continuous version of eq. (2.11).

2.1.2 Wick's theorem

Wick's theorem in its original form [46] is essentially a way of rewriting the product of some operators obeying canonical commutation or anti-commutation rules in a way that involves just normal-ordered products and some quantities, called *contractions between commuting (or anti-commuting) operators*, that behave as *c*-numbers. This reorganization is particularly handy when one wants to evaluate the expectation value of the initial product over some state and, in the end, it allows to express it in terms of the two-point correlation functions. It will be sufficient for our purpose to state the theorem as applied to vacuum expectation values of fermionic operators' products, with the final task to evaluate (1.16). In this version, the theorem reads as follows:

Let f_j be linear combinations of some fermionic operators $\{d_i, d_i^\dagger\}$ with $i \in \{1, \dots, L\}$. Wick's theorem states that the vacuum expectation value of any product of the f_j can be written as a function of the two-point correlation function only; in particular, it can be non-zero only if we consider an even number of operators, in which case

$$\langle 0|f_1 f_2 \dots f_{2N}|0\rangle = \text{Pf}_{1 \leq i, j \leq 2N} (\langle 0|\mathcal{T}[f_i f_j]|0\rangle), \quad (2.16)$$

where

$$\mathcal{T}[f_i f_j] = \begin{cases} f_i f_j, & \text{if } i < j \\ 0, & \text{if } i = j \\ -f_j f_i, & \text{if } i > j \end{cases} \quad (2.17)$$

The operator Pf is called *Pfaffian* and, given an anti-symmetric $2N \times 2N$ matrix, is defined as

$$\text{Pf}A \equiv \text{Pf}_{1 \leq i, j \leq 2N} (A_{ij}) \equiv \sum_{\sigma \in S_{2N}} (-1)^\sigma \frac{1}{2^N N!} A_{\sigma(1)\sigma(2)} \dots A_{\sigma(2N-1)\sigma(2N)}, \quad (2.18)$$

where S_n and $(-1)^\sigma$ are the set of permutations of n elements and the signature of the permutation σ respectively (the signature of a permutation is -1 to the number of exchanges between couple of elements in the original sequence to get the particular permutation).

Proof. During this proof, we will simplify the notation using $\langle A \rangle \equiv \langle 0|A|0\rangle$. Let us start proving the theorem in the special case in which, instead of being a linear combination of fermionic operators, each f_i corresponds to just one of them. In other words, we begin the proof considering the particular case of the vacuum expectation value $\langle b_1 \dots b_{2N} \rangle$ of the operators

$$b_i \in \{d_1, d_2, \dots, d_L, d_1^\dagger, d_2^\dagger, \dots, d_L^\dagger\}.$$

2.1. FREE FERMIONS' TECHNIQUES

The first observation is that, if b_{2N} is an annihilation operator, then the identity we want to prove is trivially satisfied, since both sides give zero. So we have just to consider the vacuum expectation value

$$\langle b_1 b_2 \dots b_{2N-1} d_j^\dagger \rangle,$$

where $j \in \{1, \dots, L\}$. The proof that links this vacuum expectation value to a Pfaffian is done by induction; here we follow [47] and [48].

The case $N = 1$ is trivially satisfied: the vacuum expectation value is non-zero only if $b_1 = d_j$, in which case

$$\langle b_1 b_2 \rangle \equiv \langle d_j d_j^\dagger \rangle = \frac{1}{2} \left(\langle d_j d_j^\dagger \rangle - \langle d_j^\dagger d_j \rangle \right) = \text{Pf}_{1 \leq i, j \leq 2} (\langle \mathcal{T}[b_i b_j] \rangle).$$

Let us thus suppose that the result is true for $N - 1$ and turn back to $\langle b_1 b_2 \dots b_{2N-1} d_j^\dagger \rangle$. The idea is to (anti)commute d_j^\dagger with all the other operators and bring it to the leftmost position, where it annihilates the vacuum expectation value by acting on $|0\rangle$. We have

$$\langle b_1 b_2 \dots b_{2N-1} d_j^\dagger \rangle = \sum_{i=1}^{2N-1} (-1)^{S_i} \langle b_1 \dots b_{i-1} b_{i+1} \dots b_{2N-1} \rangle [b_i, d_j^\dagger]_+,$$

where $S_i = 2N - i$ is the number of exchanges between d_j^\dagger and its left neighbour that are required to bring d_j^\dagger from the rightmost position to the $(i + 1)$ -th position, or, equivalently, the number of exchanges between b_i and its right neighbour to bring b_i from the i -th position to the $(2N - 1)$ -th position (this is the interpretation we are going to use). Going back to the notation $d_j^\dagger \rightarrow b_{2N}$, we can write

$$\langle b_1 b_2 \dots b_{2N} \rangle = \sum_{i=1}^{2N-1} (-1)^{S_i} \langle b_1 \dots b_{i-1} b_{i+1} \dots b_{2N-1} \rangle \langle b_i b_{2N} \rangle.$$

At this point we use the induction hypothesis to compute $\langle b_1 \dots b_{i-1} b_{i+1} \dots b_{2N-1} \rangle$. From the induction hypothesis we get a sum over permutations $\sum_{\sigma \in S_{2(N-1)}} (-1)^\sigma$ that can be merged with the sum $\sum_{i=1}^{2N-1} (-1)^{S_i}$ that was already present, reconstructing the sum over permutations $\sum_{\sigma \in S_{2N-1}} (-1)^\sigma$; thanks to the interpretation we gave to S_i , it is not difficult to recognize that the signature of the new permutation is obtained correctly. So

$$\begin{aligned} \langle b_1 b_2 \dots b_{2N} \rangle &= \sum_{\sigma \in S_{2N-1}} (-1)^\sigma \frac{\langle \mathcal{T}[b_{\sigma(1)} b_{\sigma(2)}] \rangle \dots \langle \mathcal{T}[b_{\sigma(2N-3)} b_{\sigma(2N-2)}] \rangle \langle b_{\sigma(2N-1)} b_{2N} \rangle}{2^{N-1}(N-1)!} \\ &= \sum_{\sigma \in S_{2N-1}} (-1)^\sigma \frac{\langle \mathcal{T}[b_{\sigma(1)} b_{\sigma(2)}] \rangle \dots \langle \mathcal{T}[b_{\sigma(2N-3)} b_{\sigma(2N-2)}] \rangle \langle \mathcal{T}[b_{\sigma(2N-1)} b_{2N}] \rangle}{2^N(N-1)!} \\ &\quad - \sum_{\sigma \in S_{2N-1}} (-1)^\sigma \frac{\langle \mathcal{T}[b_{\sigma(1)} b_{\sigma(2)}] \rangle \dots \langle \mathcal{T}[b_{\sigma(2N-3)} b_{\sigma(2N-2)}] \rangle \langle \mathcal{T}[b_{2N} b_{\sigma(2N-1)}] \rangle}{2^N(N-1)!}. \end{aligned}$$

As the last step, notice that the numerators in the last equality are invariant by moving the last factor in any position (they must be, since only products between scalars are involved), so we can write the whole term as the sum over all the possible cases divided by their number, which is N and which reconstruct $N!$. In conclusion, the whole expression can be written as a sum over the permutation of $2N$ elements. To be sure that we found the right signs for the permutations, notice that the fact that $\langle \mathcal{T}[b_{\sigma(2N-1)}b_{2N}] \rangle$ moves in each possible position does not affect the signature of the permutation since we are moving couples of elements together. Summarizing, we have proven that

$$\langle b_1 b_2 \dots b_{2N} \rangle = \text{Pf}_{1 \leq i, j \leq 2N} \langle \mathcal{T}[b_i b_j] \rangle.$$

Let us turn now the general case. To simplify the notation, let us introduce the operators $a_i = d_i$ and $a_{L+i} = d_i^\dagger$, $\forall i \in \{1, \dots, L\}$. We can write the generic linear combinations as

$$f_j = \sum_{k_j=1}^{2L} \alpha_{k_j}^{(j)} a_{k_j}$$

and the general vacuum expectation value as

$$\langle f_1 \dots f_{2N} \rangle = \sum_{k_1=1}^{2L} \alpha_{k_1}^{(1)} \dots \sum_{k_{2N}=1}^{2L} \alpha_{k_{2N}}^{(2N)} \langle a_{k_1} \dots a_{k_{2N}} \rangle.$$

The factor $\langle a_{k_1} \dots a_{k_{2N}} \rangle$ satisfies the hypothesis of the previous result and it can be written as a Pfaffian:

$$\begin{aligned} & \langle f_1 \dots f_{2N} \rangle \\ &= \sum_{k_1=1}^{2L} \alpha_{k_1}^{(1)} \dots \sum_{k_{2N}=1}^{2L} \alpha_{k_{2N}}^{(2N)} \sum_{\sigma \in S_{2N}} (-1)^\sigma \frac{\langle \mathcal{T}[a_{\sigma(k_1)} a_{\sigma(k_2)}] \rangle \dots \langle \mathcal{T}[a_{\sigma(k_{2N-1})} a_{\sigma(k_{2N})}] \rangle}{2^N N!}. \end{aligned}$$

The sums over k_i can be brought inside the vacuum expectation values of the ordered products and used to reconstruct the various f -operators, which concludes the proof. \square

As an application of Wick's theorem, let us see how (2.16) simplifies when the first N operators are a linear combination of the annihilation operators only and the last N operators are a linear combination of the creation operators only. We can adapt the notation for this case using $g_i \equiv f_{N-i}$ for the first N operators and $h_i \equiv f_{N+i}$ for the other ones (the choice in the indices is done so that the sign of the expression we are going to get is the simplest possible). This case is simpler than the general one because all the permutations that involve the vacuum expectation value of a product of two g -operators (or, equivalently, of two h -operators) give a null contribution

thanks to the canonical anti-commutation relations; so each permutation which gives a non-zero contribution will involve the vacuum expectation value where each g -operator is coupled to an h -operator. Moreover, since by assumption the original product has the h operators on the right, we can drop the time ordering, just writing

$$\mathcal{T}[g_i h_j] - \mathcal{T}[h_j g_i] = 2g_i h_j, \quad \forall i, j \in \{1, \dots, N\}. \quad (2.19)$$

These observations imply that, in order to get all the permutations that give a non-zero contribution to the vacuum expectation value, it suffices to consider the permutations of the g -operators alone and the h -operators alone: all the (potentially) non-zero contributions are given by

$$\langle 0 | g_{\sigma(1)} h_{\tilde{\sigma}(1)} | 0 \rangle \dots \langle 0 | g_{\sigma(N)} h_{\tilde{\sigma}(N)} | 0 \rangle. \quad (2.20)$$

To fix the sign of each of these contributions, notice that the number of exchanges that have to be done to connect the two sequences

$$\sigma(N) \dots \sigma(1) \tilde{\sigma}(1) \dots \tilde{\sigma}(N) \rightarrow \sigma(1) \tilde{\sigma}(1) \dots \sigma(N) \tilde{\sigma}(N) \quad (2.21)$$

is always even. This means that the signature of the permutation between the f -operators of Wick's theorem that give $\langle g_{\sigma(1)} h_{\tilde{\sigma}(1)} \rangle \dots \langle g_{\sigma(N)} h_{\tilde{\sigma}(N)} \rangle$ is obtained as the product of the signature of σ and the signature of $\tilde{\sigma}$.

Finally, we get

$$\begin{aligned} \langle 0 | g_N \dots g_1 h_1 \dots h_N | 0 \rangle &= \sum_{\sigma \in S_N} (-1)^\sigma \sum_{\tilde{\sigma} \in S_N} (-1)^{\tilde{\sigma}} \frac{\langle 0 | g_{\sigma(1)} h_{\tilde{\sigma}(1)} | 0 \rangle \dots \langle 0 | g_{\sigma(N)} h_{\tilde{\sigma}(N)} | 0 \rangle}{N!} \\ &= \frac{1}{N!} \sum_{\mu_1=1}^N \dots \sum_{\mu_N}^N \sum_{\nu_1=1}^N \dots \sum_{\nu_N}^N \varepsilon_{\mu_1 \dots \mu_N} \varepsilon_{\nu_1 \dots \nu_N} \langle 0 | g_{\mu_1} h_{\nu_1} | 0 \rangle \dots \langle 0 | g_{\mu_N} h_{\nu_N} | 0 \rangle \\ &= \det_{1 \leq i, j \leq N} \langle 0 | g_i h_j | 0 \rangle \\ \Rightarrow \boxed{\langle 0 | g_N \dots g_1 h_1 \dots h_N | 0 \rangle} &= \det M, \quad \text{where} \quad M_{ij} \equiv \langle 0 | g_i h_j | 0 \rangle. \end{aligned} \quad (2.22)$$

This result is the application of Wick's theorem we are mostly interested in.

So far the Hamiltonian never entered in our computation. This means that the validity of the result does not depend on the underlying being free. Indeed, the derivation is based just on the algebra of the operators. Now we want to apply the relations we found to time-dependent operators and the fact that the theory is free becomes important.

Suppose we want to compute the vacuum expectation value of a product of some operators f_i that can be written as a linear combination of the operators

diagonalizing the Hamiltonian $\{d_j, d_j^\dagger\}_{j \in \{1, \dots, L\}}$, but that are considered at different times. Thanks to the property (2.11), we have

$$\begin{aligned} f_i(\tau) &= e^{\tau H} f_i e^{-\tau H} = e^{\tau H} \left(\sum_{j=1}^L (\alpha_{ij} d_j + \beta_{ij} d_j^\dagger) \right) e^{-\tau H} \\ &= \sum_{j=1}^L \left(\alpha_{ij} e^{\tau \sum_k \epsilon_k d_i^\dagger d_k} d_j e^{-\tau \sum_k \epsilon_k d_i^\dagger d_k} + \beta_{ij} e^{\tau \sum_k \epsilon_k d_i^\dagger d_k} d_j^\dagger e^{-\tau \sum_k \epsilon_k d_i^\dagger d_k} \right) \\ &= \sum_{j=1}^L \left(\alpha_{ij} e^{-\tau \epsilon_j} d_j + \beta_{ij} e^{\tau \epsilon_j} d_j^\dagger \right), \end{aligned}$$

which means that the operators f_i at different times are still a linear combination of anti-commuting operators at the same time (the operators diagonalizing the Hamiltonian). Notice also that if we consider real time instead of imaginary time, this conclusion still apply and we can state the following:

For a free theory, Wick's theorem (in both the formulations (2.16) and (2.22) that we saw) holds for operators $f_i = \sum_{j=1}^L (\alpha_{ij} d_j + \beta_{ij} d_j^\dagger)$, even when they are considered at different times.

We remark that this statement relies on the theory being free, since we used (2.11).

2.2 Semi-infinite Toeplitz matrices

2.2.1 Definition

A semi-infinite Toeplitz matrix is a matrix $T = (T_{ij})_{i,j \in \mathbb{N} \cup \{0\}}$ whose elements depend only on the difference between the indices $i - j$: $T_{ij} = [g]_{i-j}$ (following the traditional notation in Toeplitz matrices' literature, we index the matrix elements starting from zero). In the following, it will be convenient to interpret $[g]_l$ as the l -th Fourier coefficient of a function $g(k)$, called *symbol* (the square brackets are indeed the usual notation for Fourier coefficient in the Toeplitz matrix literature) In formulas:

$$[f]_l = \int_{-\pi}^{+\pi} \frac{dk}{2\pi} e^{-ilk} f(k) \quad , \quad f(k) = \sum_{l \in \mathbb{Z}} e^{ikl} [f]_l. \quad (2.23)$$

To identify the Toeplitz matrix whose elements are the Fourier coefficients of the symbol $g(k)$, we use the notation $T(g)$; for more detailed theory of Toeplitz matrices, see e.g. [49].

This definition could be generalized to a *semi-infinite block Toeplitz matrix*, where the elements' property of depending only on the difference of the indices holds just

for the blocks of the matrix. In fact, all the properties we are going to see still hold if the symbol is a matrix, in which case the various products should be read as matrix products (we paid attention to the factors' order).

In the remainder of the section, we will introduce some notation and show some properties of the semi-infinite Toeplitz matrices that will be useful later.

2.2.2 Wiener-Hopf decomposition

The central role in the properties of semi-infinite Toeplitz matrices is played by the Wiener-Hopf decomposition of a function $g(k)$, which consists in writing $g(k)$ as the product of two functions

$$g(k) = g^-(k)g^+(k), \quad (2.24)$$

where g^+ (resp. g^-) only has non-negative (resp. non-positive) Fourier coefficients. In other words, the Wiener-Hopf decomposition of the function $g(k)$ consists in finding two functions $g^+(k)$ and $g^-(k)$ such that

$$[g^-]_{-m} = 0 \quad \wedge \quad [g^+]_m = 0, \quad \forall m \in \mathbb{Z}^-, \quad (2.25)$$

and such that their product gives $g(k)$. The two function $g^\pm(k)$ can be written as

$$g^+(k) = \sum_{m=0}^{+\infty} [g^+]_m e^{imk} \quad \text{and} \quad g^-(k) = \sum_{m=-\infty}^0 [g^-]_m e^{imk}. \quad (2.26)$$

The way the Wiener-Hopf decomposition is usually obtained, at least when $g(k)$ is scalar and has a well defined logarithm, is by writing

$$\begin{aligned} g(k) &= \exp(\log g(k)) \\ &= \exp\left(\sum_{m \in \mathbb{Z}} [\log g]_m e^{ikm}\right) \\ &= \exp\left(\sum_{m<0} [\log g]_m e^{ikm}\right) \exp\left(\sum_{m \geq 0} [\log g]_m e^{ikm}\right) \end{aligned} \quad (2.27)$$

and then identifying $g^-(k)$ with the first factor and $g^+(k)$ with the second one (since the sums in the exponents have either non-negative or non-positive modes, the same thing will be hold for the series obtained by expanding the two exponentials individually).

Finding a Wiener-Hopf factorization is in general tremendously difficult, especially when we consider the case in which the functions are not scalar.

The Wiener-Hopf decomposition $g(k) = g^-(k)g^+(k)$ is essentially the Toeplitz matrices version of the UL decomposition, where we recall that the UL decomposition of given a matrix consists in writing the matrix as the product of an upper

triangular matrix, a lower triangular matrix and, potentially, a permutation. In particular, the claim is that

$$T(g) = T(g^-)T(g^+), \quad (2.28)$$

with $T(g^-)$ and $T(g^+)$ being upper and lower triangular respectively.

Proof. First of all, notice that, by definition of $g^-(k)$ and $g^+(k)$, the statement about $T(g^-)$ and $T(g^+)$ being upper triangular and lower triangular is trivial.

Then notice also that the Wiener-Hopf decomposition is in principle always possible for integrable $\ln(g(k))$, since it just relies on the possibility of Fourier-decomposing $\ln(g(k))$ and then separate its modes. Let us show that it does indeed reconstruct the matrix:

$$(T(g^-)T(g^+))_{mn} = \sum_{l=0}^{+\infty} T(g^-)_{ml} T(g^+)_{ln} = \sum_{l=0}^{+\infty} [g^-]_{m-l} [g^+]_{l-n} \quad (2.29)$$

Now, since $n \geq 0$, a necessary (though not sufficient) condition for the matrix element $[g^+]_{l-n}$ to be non-zero is $l \geq 0$. This means that we can extend the sum over all the integers: it just amounts to add to the sum we already have infinite zeros. So

$$\begin{aligned} (T(g^-)T(g^+))_{mn} &= \sum_{l \in \mathbb{Z}} [g^-]_{m-l} [g^+]_{l-n} \\ &= \sum_{l \in \mathbb{Z}} \int_{-\pi}^{+\pi} \frac{dk}{2\pi} e^{-ik(m-l)} g^-(k) \int_{-\pi}^{+\pi} \frac{dk'}{2\pi} e^{-ik'(l-n)} g^+(k') \\ &= \int_{-\pi}^{+\pi} \frac{dk}{2\pi} g^-(k) g^+(k) e^{-ikm} e^{ikn} \\ &= \int_{-\pi}^{+\pi} \frac{dk}{2\pi} g(k) e^{-ik(m-n)} = [g]_{m-n} = (T(g))_{mn}, \end{aligned} \quad (2.30)$$

□

where we used the Dirac comb representation $\sum_{s \in \mathbb{Z}} \delta(k - 2\pi s) = \frac{1}{2\pi} \sum_{l \in \mathbb{Z}} e^{ilk}$.

The UL decomposition is a key step when inverting a matrix or computing the determinant of a matrix in many numerical and theoretical techniques and this is precisely what we will use the Wiener-Hopf decomposition for. (Actually the LU decomposition is usually used rather than the UL decomposition, but they have the same properties.)

2.2.3 Inversion formula

Consider an invertible semi-infinite Toeplitz matrix $T(g)$ and let

$$g(k) = g^-(k)g^+(k) \quad (2.31)$$

be the Wiener-Hopf decomposition of the symbol $g(k)$. The inverse of T can be computed as follows:

$$(T^{-1}(g))_{mn} = \sum_{r=0}^{\infty} [(g^+)^{-1}]_{m-r} [(g^-)^{-1}]_{-n+r}, \quad (2.32)$$

or, equivalently,

$$(T^{-1}(g))_{mn} = \sum_{r=0}^{\min(m,n)} [(g^+)^{-1}]_{m-r} [(g^-)^{-1}]_{-n+r}. \quad (2.33)$$

We prefer to work with the infinite sum version because infinite sums are usually easier to treat. The second version of the inversion formula can be more useful for numerical computation.

Proof. The first step is to imply that $(T(g^\pm))^{-1} = T((g^\pm)^{-1})$. First of all, notice that $(g^+(k))^{-1}$ has itself just positive Fourier coefficients. This is because

$$(g^+(k))^{-1} = \frac{1}{\sum_{l=0}^{+\infty} e^{ikl} [g^+]_l}, \quad (2.34)$$

which, if $[g^+]_0 \neq 0$, is expanded as the geometric series and is again a series in positive powers of e^{ikl} .¹ In fact, we know that $[g^+]_0 \neq 0$ since otherwise the triangular matrix $T(g^+)$ would have zeros on the principal diagonal and it would not be invertible, implying that neither $T(g)$ is and invalidating the hypothesis. An analogous thing holds for $g^-(k)$. This tells us that, for $l < 0$, either $[g^\pm]_{m-l}$ or $[(g^\pm)^{-1}]_{l-m}$ is zero $\forall m \geq 0$ and allows to write

$$\begin{aligned} (T(g^\pm)T((g^\pm)^{-1}))_{mn} &= \sum_{l=0}^{+\infty} [g^\pm]_{m-l} [(g^\pm)^{-1}]_{l-n} = \sum_{l \in \mathbb{Z}} [g^\pm]_{m-l} [(g^\pm)^{-1}]_{l-n} \\ &= \sum_{l \in \mathbb{Z}} \int_{-\pi}^{+\pi} \frac{dk}{2\pi} e^{-ik(m-l)} g^\pm(k) \int_{-\pi}^{+\pi} \frac{dk'}{2\pi} e^{-ik'(l-n)} (g^\pm(k'))^{-1} \\ &= \int_{-\pi}^{+\pi} \frac{dk}{2\pi} e^{-ikm} e^{ikn} = \delta_{mn}, \end{aligned} \quad (2.35)$$

where we used again where we used the Dirac comb representation $\sum_{s \in \mathbb{Z}} \delta(k - 2\pi s) = \frac{1}{2\pi} \sum_{l \in \mathbb{Z}} e^{ilk}$. Summarizing

$$(T^{-1}(g))_{mn} = (T^{-1}(g^+)T^{-1}(g^-))_{mn} = \sum_{r=0}^{\infty} [(g^+)^{-1}]_{m-r} [(g^-)^{-1}]_{-n+r}. \quad (2.36)$$

¹This should be taken more as an heuristic argument than as a formal statement, since we are not discussing the convergence issues that arise in the summation of the geometric series. We refer to [49] for a formal discussion. In any case, this will not be relevant in all the cases that will be treated later on.

We can use again the fact that $(g^-(k))^{-1}$ has only non-positive Fourier coefficients to restrict the sum's domain:

$$(T^{-1}(g))_{mn} = (T^{-1}(g^+)T^{-1}(g^-))_{mn} = \sum_{r=0}^{\min(m,n)} [(g^+)^{-1}]_{m-r}[(g^-)^{-1}]_{-n+r}. \quad (2.37)$$

This gives also the second representation of T^{-1} that we anticipated. \square

Notice that in this proof it was important that the matrix under consideration was semi-infinite: without the infinite sums we could not have reconstructed the various delta functions that we used. Let us just cite that a similar result holds for finite Toeplitz matrices and it is usually referred to as *Widom's formula* [50].

Similar to what we did for the inverse, the Wiener-Hopf decomposition could be employed to find a determinant formula for Toeplitz matrices. We are not going to do that, since we are interested in the inversion formula only, but it can be found in [51].

Chapter 3

Exact Two-point Function

3.1 Scope of the chapter

We start from the definition (1.16) of the two-point correlation function in domain wall geometry that we gave in Chapter 1; it is repeated here for convenience:

$$\langle \psi_1 | c_x^\dagger(y) c_{x'}(y') | \psi_1 \rangle_R \equiv \frac{\langle \psi_1 | e^{-(R-y)H} c_x^\dagger e^{(y'-y)H} c_{x'} e^{-(R+y')H} | \psi_1 \rangle}{\langle \psi_1 | e^{-2RH} | \psi_1 \rangle}. \quad (3.1)$$

where $x, x' \in \tilde{\mathbb{Z}}$ and $|\psi_1\rangle$ is the state in which the lattice is completely filled on the left of the origin and completely empty on the right. The particular Hamiltonian H of the system will not be important in this chapter, provided it is quadratic, time independent and invariant by a shift in the lattice indices (so that it can be diagonalized by Fourier series).

In this chapter we aim at constructing an exact integral formula for this quantity, providing an alternative derivation of a known result. The usual derivation uses a procedure known as *bosonization*, see e.g. [28, 52], while here we provide a derivation in two steps: first we use Wick's theorem to write the correlation function as a product of semi-infinite matrices; then we exploit semi-infinite Toeplitz matrices' properties to simplify the result. With respect to bosonization, our derivation may be extended straightforwardly to other geometries.

3.2 Two-point function as a product of matrices

We consider the quantity

$$I \equiv \frac{\langle \psi_1 | e^{\beta H} c_x^\dagger e^{\gamma H} c_{x'} e^{\delta H} | \psi_1 \rangle}{\langle \psi_1 | e^{(\beta+\gamma+\delta)H} | \psi_1 \rangle}, \quad (3.2)$$

which is a concise way to write the two-point function (3.1). We are going to rewrite it as a product of semi-infinite matrices via Wick's theorem (2.22). The first step to

apply the theorem is to reorder the fermionic operators according to the convention we used to state (2.22). To do that, we first go to the momentum basis, obtaining

$$\begin{aligned} e^{\beta H} c_x^\dagger e^{\gamma H} c_{x'} e^{\delta H} &= \int_{-\pi}^{+\pi} \frac{dk}{2\pi} \int_{-\pi}^{+\pi} \frac{dk'}{2\pi} e^{-ikx} e^{ik'x'} e^{\beta H} d^\dagger(k) e^{\gamma H} d(k') e^{\delta H} \\ &= \int_{-\pi}^{+\pi} \frac{dk}{2\pi} \int_{-\pi}^{+\pi} \frac{dk'}{2\pi} e^{-ikx} e^{ik'x'} e^{(\beta+\gamma)H} e^{-\gamma H} d^\dagger(k) e^{\gamma H} d(k') e^{\delta H}. \end{aligned} \quad (3.3)$$

Then we apply the free-fermions property (2.15) to get

$$\begin{aligned} e^{\beta H} c_x^\dagger e^{\gamma H} c_{x'} e^{\delta H} &= \int_{-\pi}^{+\pi} \frac{dk}{2\pi} \int_{-\pi}^{+\pi} \frac{dk'}{2\pi} e^{-ikx} e^{ik'x'} e^{(\beta+\gamma)H} e^{-\gamma\epsilon(k)} d^\dagger(k) d(k') e^{\delta H} \\ &= \int_{-\pi}^{+\pi} \frac{dk}{2\pi} \int_{-\pi}^{+\pi} \frac{dk'}{2\pi} e^{ik(x'-x)} e^{(\beta+\gamma)H} e^{-\gamma\epsilon(k)} e^{\delta H} \langle 0 | d(k) d^\dagger(k) | 0 \rangle \quad (3.4) \\ &\quad - \int_{-\pi}^{+\pi} \frac{dk}{2\pi} \int_{-\pi}^{+\pi} \frac{dk'}{2\pi} e^{-ikx} e^{ik'x'} e^{(\beta+\gamma)H} e^{-\gamma\epsilon(k)} d(k') d^\dagger(k) e^{\delta H}, \end{aligned}$$

where we used the canonical anti-commutation relations (2.14) and we wrote the Dirac delta function coming from them as $\langle 0 | d(k) d^\dagger(k) | 0 \rangle = 2\pi\delta(k - k')$ (remember we are assuming $\langle 0 | 0 \rangle = 1$). Finally, using again (2.15), this time in the opposite direction, and going back to the position basis, we finally have

$$e^{\beta H} c_x^\dagger e^{\gamma H} c_{x'} e^{\delta H} = \langle 0 | c_{x'} c_x^\dagger (-\gamma) | 0 \rangle e^{(\beta+\gamma+\delta)H} - e^{(\beta+\gamma)H} c_{x'} e^{-\gamma H} c_x^\dagger e^{(\gamma+\delta)H} \quad (3.5)$$

and

$$I = \langle 0 | c_{x'} c_x^\dagger (-\gamma) | 0 \rangle - \frac{\langle \psi_1 | e^{(\beta+\gamma)H} c_{x'} e^{-\gamma H} c_x^\dagger e^{(\gamma+\delta)H} | \psi_1 \rangle}{\langle \psi_1 | e^{(\beta+\gamma+\delta)H} | \psi_1 \rangle}, \quad (3.6)$$

which is suitable for the application of Wick's theorem (2.22):

Now, just for the following intermediate step, we will assume the number of lattice sites to be finite and equal to $2l$, to simplify the notation. With this convention, the sites $\{-1/2, -3/2, \dots, -l + 1/2\}$ are filled and the sites $\{1/2, 3/2, \dots, l - 1/2\}$ are empty. After the application of Wick's theorem we will take the limit $l \rightarrow +\infty$. In this way, we can explicitly turn our expectation values in vacuum expectation values:

$$\begin{aligned} &\langle \psi_1 | e^{(\beta+\gamma)H} c_{x'} e^{-\gamma H} c_x^\dagger e^{(\gamma+\delta)H} | \psi_1 \rangle \\ &= \langle 0 | c_{-\frac{1}{2}} \dots c_{-l+\frac{1}{2}} e^{(\beta+\gamma)H} c_{x'} e^{-\gamma H} c_x^\dagger e^{(\gamma+\delta)H} c_{-l+\frac{1}{2}}^\dagger \dots c_{-\frac{1}{2}}^\dagger | 0 \rangle \quad (3.7) \\ &= \langle 0 | c_{-l+\frac{1}{2}}(0) \dots c_{-\frac{1}{2}}(0) c_{x'} (\beta + \gamma) c_x^\dagger (\beta) c_{-\frac{1}{2}}^\dagger (\beta + \gamma + \delta) \dots c_{-l+\frac{1}{2}}^\dagger (\beta + \gamma + \delta) | 0 \rangle, \end{aligned}$$

where we used $e^H | 0 \rangle = | 0 \rangle$ and we reordered the fermionic operators in the last equality to make the Wick's theorem expression look nicer (this operation does not introduce any sign because we do the same permutation on both the right and the left).

3.2. TWO-POINT FUNCTION AS A PRODUCT OF MATRICES

Finally, from Wick's theorem (2.22) and using

$$\langle 0 | c_m(y_1) c_n^\dagger(y_2) | 0 \rangle = \langle 0 | c_m c_n^\dagger(y_2 - y_1) | 0 \rangle, \quad (3.8)$$

we have

$$\langle \psi_1 | e^{(\beta+\gamma)H} c_{x'} e^{-\gamma H} c_x^\dagger e^{(\gamma+\delta)H} | \psi_1 \rangle = \det M, \quad (3.9)$$

with

$$M = \begin{pmatrix} \langle 0 | c_{x'} c_x^\dagger(-\gamma) | 0 \rangle & u^T \\ v & T \end{pmatrix}. \quad (3.10)$$

Here u and v are l -components column vector and T is a $l \times l$ -matrix, defined as

$$v_n \equiv \langle 0 | c_{-n-\frac{1}{2}} c_x^\dagger(\beta) | 0 \rangle, \quad (3.11)$$

$$u_m \equiv \langle 0 | c_{x'} c_{-m-\frac{1}{2}}^\dagger(\delta) | 0 \rangle, \quad (3.12)$$

$$T_{mn} \equiv \langle 0 | c_{-m-\frac{1}{2}} c_{-n-\frac{1}{2}}^\dagger(\beta + \gamma + \delta) | 0 \rangle, \quad (3.13)$$

where we indexed the matrix and vector elements starting from zero, as usually done in Toeplitz matrices literature.

A similar computation leads to

$$\langle \psi_1 | e^{(\beta+\gamma+\delta)H} | \psi_1 \rangle = \det T, \quad (3.14)$$

with T defined as above.

Summarizing:

$$I = \langle 0 | c_{x'} c_x^\dagger(-\gamma) | 0 \rangle - \frac{\det M}{\det T}. \quad (3.15)$$

At this point it comes in handy to define the matrix $\tilde{T} = \begin{pmatrix} 1 & 0 \\ 0 & T \end{pmatrix}$, so that

$$\begin{aligned} \frac{\det M}{\det T} &= \frac{\det M}{\det \tilde{T}} = \det(M\tilde{T}^{-1}) = \det \begin{pmatrix} \langle 0 | c_{x'} c_x^\dagger(-\gamma) | 0 \rangle & u^T T^{-1} \\ v & \mathbb{I}_l \end{pmatrix} \\ &= \langle 0 | c_{x'} c_x^\dagger(-\gamma) | 0 \rangle + \sum_{n=0}^{l-1} (-1)^n (u^T T^{-1})_n \det(v|A_n), \end{aligned} \quad (3.16)$$

where A_n is a $l \times (l-1)$ -matrix such that the n -th row is composed only by zeros and without the n -th row the matrix equals \mathbb{I}_{l-1} . Now, if we expand $\det(v|A_n)$ with respect to the first column, the only non-zero contribution comes from the n -th element, which means

$$\det(v|A_n) = (-1)^{n+1} v_n. \quad (3.17)$$

This implies

$$\begin{aligned} \frac{\det M}{\det \tilde{T}} &= \langle 0 | c_{x'} c_x^\dagger(-\gamma) | 0 \rangle + \sum_{n=0}^{l-1} (-1)^n (-1)^{n+1} (u^T T^{-1})_n v_n \\ &= \langle 0 | c_{x'} c_x^\dagger(-\gamma) | 0 \rangle - \sum_{m,n=0}^{l-1} u_m T_{mn}^{-1} v_n, \end{aligned} \quad (3.18)$$

so that, going back to infinite size,

$$I = \sum_{m,n=0}^{+\infty} u_m T_{mn}^{-1} v_n, \quad (3.19)$$

with

$$\begin{aligned} u_m &= \langle 0 | c_{x'} c_{-m-\frac{1}{2}}^\dagger(\delta) | 0 \rangle, \\ v_n &= \langle 0 | c_{-n-\frac{1}{2}} c_x^\dagger(\beta) | 0 \rangle, \\ T_{mn} &= \langle 0 | c_{-m-\frac{1}{2}} c_{-n-\frac{1}{2}}^\dagger(\beta + \gamma + \delta) | 0 \rangle. \end{aligned} \quad (3.20)$$

The application of this result to the two-point correlation function straightforwardly gives

$$\langle \psi_1 | c_x^\dagger(y) c_{x'}(y') | \psi_1 \rangle_R = \sum_{m,n=0}^{+\infty} u_m T_{mn}^{-1} v_n,$$

where

$$(3.21)$$

$$\begin{aligned} u_m &= \langle 0 | c_{x'} c_{-m-\frac{1}{2}}^\dagger(-(R + y')) | 0 \rangle \\ v_n &= \langle 0 | c_{-n-\frac{1}{2}} c_x^\dagger(-(R - y)) | 0 \rangle \\ T_{mn} &= \langle 0 | c_{-m-\frac{1}{2}} c_{-n-\frac{1}{2}}^\dagger(-2R) | 0 \rangle \end{aligned}$$

As anticipated, Wick's theorem allowed us to write the two-point correlation function as a product of semi-infinite matrices. At this point, though, the expression for the inverse of T remains implicit, but we can fix this using the results of Section 2.2.

3.3 Two-point function as a double integral

We start by showing that the matrix T introduced in the previous section is indeed a semi-infinite Toeplitz matrix. To do so, we use the momentum basis and

3.3. TWO-POINT FUNCTION AS A DOUBLE INTEGRAL

employ the property (2.15) of free fermions to write the matrix elements as integrals:

$$\begin{aligned} T_{mn} &= \int_{-\pi}^{+\pi} \frac{dk}{2\pi} \int_{-\pi}^{+\pi} \frac{dq}{2\pi} e^{iq(-m-\frac{1}{2})} e^{-ik(-n-\frac{1}{2})} \langle 0 | d(q) e^{-2RH} d^\dagger(k) e^{2RH} | 0 \rangle \\ &= \int_{-\pi}^{+\pi} \frac{dq}{2\pi} e^{-iq(m-n)} e^{-2R\epsilon(q)}, \end{aligned} \quad (3.22)$$

where we have also used the canonical anti-commutation relations (2.14). Since the generic element of T depends on the indices difference only (once the dispersion relation and R are fixed), we conclude that T is a semi-infinite Toeplitz matrix. Thus, following the notation introduced in Section 2.2, we can introduce a symbol $g(k)$ whose Fourier coefficients define the matrix elements of T as $T_{mn} = [g]_{m-n}$. For convenience, recall that our conventions on symbols and Fourier coefficients are

$$[g]_l = \int_{-\pi}^{+\pi} \frac{dk}{2\pi} e^{-ikl} g(k) \quad , \quad g(k) = \sum_{l \in \mathbb{Z}} e^{ikl} [g]_l. \quad (3.23)$$

In the present case we have trivially

$$g(k) = e^{-2R\epsilon(k)}. \quad (3.24)$$

To highlight the dependence on the imaginary time of the symbol, it is useful to introduce the notation

$$g_\tau(k) \equiv e^{-\tau\epsilon(k)}, \quad (3.25)$$

such that

$$T_{mn} = \int_{-\pi}^{+\pi} \frac{dq}{2\pi} e^{-iq(m-n)} g_{2R}(q). \quad (3.26)$$

Notice that also the elements of the two vectors involved in the expression of the two-point function (3.21) can be expressed in function of the symbol $g_\tau(k)$ for certain imaginary times:

$$\begin{aligned} u_m &\equiv \langle 0 | c_{x'} c_{-m-\frac{1}{2}}^\dagger(-(R+y')) | 0 \rangle \\ &= \int_{-\pi}^{+\pi} \frac{dk}{2\pi} \int_{-\pi}^{+\pi} \frac{dq}{2\pi} e^{iqx'} e^{-ik(-m-\frac{1}{2})} \langle 0 | d(q) e^{-(R+y')H} d(k)^\dagger e^{(R+y')H} | 0 \rangle \\ &= \int_{-\pi}^{+\pi} \frac{dq}{2\pi} e^{iq(x'+m+\frac{1}{2})} e^{-(R+y')\epsilon(q)} \\ &= \int_{-\pi}^{+\pi} \frac{dq}{2\pi} e^{iq(x'+m+\frac{1}{2})} g_{R+y'}(q) = [g_{R+y'}]_{-m-x'-\frac{1}{2}}, \end{aligned} \quad (3.27)$$

and, analogously,

$$\begin{aligned} v_n &\equiv \langle 0 | c_{-n-\frac{1}{2}} c_x^\dagger(R-y) | 0 \rangle \\ &= \int_{-\pi}^{+\pi} \frac{dq}{2\pi} e^{-iq(n+\frac{1}{2}+x)} g_{R-y}(q) = [g_{R-y}]_{n+x+\frac{1}{2}}, \end{aligned} \quad (3.28)$$

where, again, we used (2.15) and the canonical anti-commutation relations.

Now that we have identified T as a semi-infinite Toeplitz matrix, we can use the property (2.32) to compute its inverse. Consider the Wiener-Hopf decomposition of $g_\tau(k)$, namely $g_\tau(k) = g_\tau^-(k)g_\tau^+(k)$; thanks to (2.32), we have

$$(T^{-1})_{mn} = \sum_{r=0}^{\infty} [(g^+)^{-1}]_{m-r} [(g^-)^{-1}]_{-n+r}. \quad (3.29)$$

Using this and representing the vectors u and v via the respective symbols, we can rewrite two-point function (3.21) as

$$\langle \psi_1 | c_x^\dagger(y) c_{x'}(y') | \psi_1 \rangle_R = \sum_{m,n,r=0}^{+\infty} [g_{R+y'}]_{-m-x'-\frac{1}{2}} [(g_{2R}^+)^{-1}]_{m-r} [(g_{2R}^-)^{-1}]_{-n+r} [g_{R-y}]_{n+x+\frac{1}{2}}. \quad (3.30)$$

In the expression above, the indices m, n assume only non-negative integer values, since they are matrices' indices. But the sum can be extended to all \mathbb{Z} : since $r \geq 0$, all the additional terms will be zero due to either $[(g^+)^{-1}]_{m-r}$ or $[(g^-)^{-1}]_{-n+r}$. So, writing the Fourier coefficients as integrals, one gets

$$\begin{aligned} & \langle \psi_1 | c_x^\dagger(y) c_{x'}(y') | \psi_1 \rangle_R \\ &= \sum_{m,n \in \mathbb{Z}} \sum_{r=0}^{+\infty} \int_{-\pi}^{+\pi} \frac{dp ds dk dq}{(2\pi)^4} e^{im(p-q)+in(k-s)+ir(q-k)-is(x+\frac{1}{2})+ip(x'+\frac{1}{2})} \frac{g_{R+y'}(p)g_{R-y}(s)}{g_{2R}^+(q)g_{2R}^-(k)}. \end{aligned} \quad (3.31)$$

Now we can use the two infinite sums to reconstruct two Dirac combs:

$$\sum_{m,n \in \mathbb{Z}} e^{im(q-p)+in(s-k)} = (2\pi)^2 \sum_{a \in \mathbb{Z}} \delta(p - q - 2\pi a) \sum_{b \in \mathbb{Z}} \delta(s - k - 2\pi b); \quad (3.32)$$

notice that this was possible only because we were able to extend the sums to the whole \mathbb{Z} , as a consequence of the Wiener-Hopf decomposition. As for the last sum,

$$\begin{aligned} e^{\frac{1}{2}i(q-k)} \sum_{r=0}^{+\infty} e^{ir(q-k)} &= e^{\frac{1}{2}i(q-k)} \sum_{r=0}^{+\infty} e^{ir(q-k+i0)} \\ &= e^{\frac{1}{2}i(q-k)} \frac{1}{1 - e^{i(q-k+i0)}} \\ &= \frac{1}{2i \sin(\frac{k-q}{2} - i0)}. \end{aligned} \quad (3.33)$$

Summarizing,

$$\langle \psi_1 | c_x^\dagger(y) c_{x'}(y') | \psi_1 \rangle_R = \int_{-\pi}^{+\pi} \frac{dk}{2\pi} \int_{-\pi}^{+\pi} \frac{dq}{2\pi} \frac{e^{-ikx+iqx'}}{2i \sin(\frac{k-q}{2} - i0)} \frac{g_{R+y'}(q)g_{R-y}(k)}{g_{2R}^+(q)g_{2R}^+(k)}. \quad (3.34)$$

3.3. TWO-POINT FUNCTION AS A DOUBLE INTEGRAL

This is already an interesting result, but it is still implicit, since it relies on the knowledge of the Wiener-Hopf decomposition of $g(k)$, which can be far from trivial.

To proceed, let us introduce the new function

$$\phi(k) \equiv e^{-\epsilon(k)}, \quad (3.35)$$

so that

$$g_\tau(k) = (\phi(k))^\tau. \quad (3.36)$$

Writing the Wiener-Hopf decomposition of $\phi(k)$ as $\phi(k) = \phi^-(k)\phi^+(k)$, we have that, for any $\tau > 0$,

$$g_\tau^\pm(k) = (\phi^\pm(k))^\tau, \quad (3.37)$$

since the power does not change the sign of Fourier modes. Thus

$$\frac{g_{R+y}(q)g_{R-y}(k)}{g_{2R}^+(q)g_{2R}^-(k)} = (\phi(q))^{y'}(\phi(k))^{-y} \frac{(\phi(q))^R(\phi(k))^R}{(\phi^+(q))^{2R}(\phi^-(k))^{2R}}. \quad (3.38)$$

Now, since we are dealing with scalar functions, we can employ the logarithm to formally write the Wiener-Hopf decomposition, as explained in Section 2.2. Note that here $\ln(\phi(k))$ is nothing but $-\epsilon(k)$. To exploit this, it is convenient to divide the Fourier modes of the dispersion relation according to their sign:

$$\epsilon(k) = \sum_{n=-\infty}^{-1} e^{ink}[\epsilon]_n + [\epsilon]_0 + \sum_{n=+1}^{+\infty} e^{ink}[\epsilon]_n \equiv \epsilon_-(k) + [\epsilon]_0 + \epsilon_+(k), \quad (3.39)$$

where, to avoid confusion, we remark that

$$\epsilon_-(k) = \sum_{n=-\infty}^{-1} e^{ink}[\epsilon]_n \quad \text{and} \quad \epsilon_+(k) = \sum_{n=+1}^{+\infty} e^{ink}[\epsilon]_n \quad (3.40)$$

are not the same as the two factors involved in our definition of the Wiener-Hopf decomposition of $\epsilon(k)$, which would read $\epsilon(k) = \epsilon^-(k)\epsilon^+(k)$. In this way we have

$$\phi^+(k) = e^{-\epsilon_+(k)+\epsilon_0} \quad \text{and} \quad \phi^-(k) = e^{-\epsilon_-(k)}, \quad (3.41)$$

implying

$$\frac{(\phi(q))^R(\phi(k))^R}{(\phi^+(q))^{2R}(\phi^-(k))^{2R}} = e^{+R(\epsilon_+(q)-\epsilon_-(q))} e^{-R(\epsilon_+(k)-\epsilon_-(k))}. \quad (3.42)$$

One can recognize in the two exponents the *Hilbert transform* $\tilde{\epsilon}(k)$ of the function $\epsilon(k)$, that, for a periodic function, can be defined precisely as the difference between the positive and the negative Fourier modes of the function over the imaginary unit (a discussion of the more traditional definition of the Hilbert transform in

mathematical literature can be found in [53], while [25, p. 48] contains a nice summary of Hilbert transform properties). We thus end up with

$$\langle \psi_1 | c_x^\dagger(y) c_{x'}(y') | \psi_1 \rangle_R = \int_{-\pi}^{+\pi} \frac{dk}{2\pi} \int_{-\pi}^{+\pi} \frac{dq}{2\pi} \frac{e^{-ikx+iqx'+y\epsilon(k)-y'\epsilon(q)+iR(\tilde{\epsilon}(q)-\tilde{\epsilon}(k))}}{2i \sin(\frac{k-q}{2} - i0)}. \quad (3.43)$$

As for the Hilbert transform, there is a simple way to compute it:

the Hilbert transform $\tilde{\epsilon}(k)$ of a periodic function with period T

$$\begin{aligned} \epsilon(k) &= \sum_{n \in \mathbb{Z}} e^{\frac{2\pi i}{T} nk} [\epsilon]_n \\ &= [\epsilon]_0 + \sum_{n=1}^{+\infty} \left[\cos\left(\frac{2\pi}{T} nk\right) ([\epsilon]_n + [\epsilon]_{-n}) + i \sin\left(\frac{2\pi}{T} nk\right) ([\epsilon]_n - [\epsilon]_{-n}) \right] \end{aligned} \quad (3.44)$$

can be computed by dropping the constant term and making the substitutions

$$\begin{aligned} \cos(nk) &\rightarrow & \sin(nk) \\ \sin(kn) &\rightarrow & -\cos(kn) \end{aligned} \quad (3.45)$$

in the Fourier modes. In other words

$$\tilde{\epsilon}(k) = \sum_{n=1}^{+\infty} \left[\sin\left(\frac{2\pi}{T} nk\right) ([\epsilon]_n + [\epsilon]_{-n}) - i \cos\left(\frac{2\pi}{T} nk\right) ([\epsilon]_n - [\epsilon]_{-n}) \right]. \quad (3.46)$$

Indeed, from the definition,

$$\epsilon_+(k) - \epsilon_-(k) = \sum_{n=1}^{+\infty} \left[i \sin\left(\frac{2\pi}{T} nk\right) ([\epsilon]_n + [\epsilon]_{-n}) + \cos\left(\frac{2\pi}{T} nk\right) ([\epsilon]_n - [\epsilon]_{-n}) \right] \quad (3.47)$$

Summarizing, starting from the result (3.21) obtained via Wick's theorem and using semi-infinite Toeplitz matrices' properties, we managed to get an exact integral formula for the two point function, in which every term is explicit.

To conclude this section, let us point out the importance of having considered the domain wall geometry in the computation we just completed. The choice of initial and final conditions manifests itself in the definition of the matrix and vectors elements in (3.21), since they are connected to the creation operators that reconstruct the initial and final states. Basically, we can imagine that there exists a function $S(n)$ from the set of non-negative integers to \mathbb{Z} that reconstructs the particular geometry, in the sense that the initial and final states are written as $|\psi\rangle = c_{S(1)-\frac{1}{2}}^\dagger c_{S(2)-\frac{1}{2}}^\dagger \dots |0\rangle$. Then, going through the same application of Wick's theorem we did in the previous section, one would end up with $T_{mn} \equiv \langle 0 | c_{S(m)-\frac{1}{2}}^\dagger c_{S(n)-\frac{1}{2}}^\dagger (\beta + \gamma + \delta) | 0 \rangle$. In the

domain wall case $S(n) = -n$, but for a generic geometry, the function $S(n)$ can be much more complicated. It can be shown that the generic element T_{mn} depends only on the difference $S(m) - S(n)$, but this does not necessarily make T a Toeplitz matrix. As a consequence, we are not able, in general, to use semi-infinite Toeplitz matrices' properties. Moreover, even if T were indeed Toeplitz, the identification of the symbol $g(k)$ defining the matrix could be not as straightforward as was in the domain wall geometry. We are going to tackle this issue in Chapter 5.

3.4 Finite-size two-point correlation function

Before looking at the applications of the formula (3.43) we just found, let us give a finite-size version of the result. This is particularly useful for the numerical study of the density profile because numerical simulations are done in large but finite size. The derivation still uses Wick's theorem but it assumes that the matrix T is inverted by some linear algebra algorithm for finite-size square matrices, hence we do not need semi-infinite Toeplitz matrices' properties here.

In the following, the lattice sites will be indexed from 1 to $2l$. They can trivially be linked to the indexing $\tilde{\mathbb{Z}}$ that we used above by shifting the labels of $-l - \frac{1}{2}$ and taking the limit $l \rightarrow +\infty$.

Let us start by recalling the discussion about finite-size free-fermions models that we had in Section 2.1.1. We implied that a Hamiltonian $H = \sum_{i,j=1}^{2l} A_{ij} c_i^\dagger c_j$ can be diagonalized to $H = \sum_{k=1}^{2l} \epsilon_k d_k^\dagger d_k$ using an ortho-normalized basis of eigenvectors $\{u^{(k)}\}_{k=\{1,\dots,2l\}}$ of A and defining a new set of fermionic operators

$$d_k^\dagger \equiv \sum_{j=1}^{2l} u_j^{(k)} c_j^\dagger, \quad d_k \equiv \sum_{j=1}^{2l} \left(u_j^{(k)}\right)^* c_j, \quad k \in \{1, \dots, 2l\}. \quad (3.48)$$

We can also define the unitary matrix of the change of basis S , with elements $S_{kj} \equiv (u_k)_j^*$, that allows to write

$$c_i^\dagger = \sum_{q=1}^{2l} d_q^\dagger S_{qi}, \quad c_i = \sum_{q=1}^{2l} S_{iq}^\dagger d_q. \quad (3.49)$$

The Wick's theorem result (3.21) can be easily adapted to this finite-size problem

as follows:

$$\langle \psi_1 | c_x^\dagger(y) c_{x'}(y') | \psi_1 \rangle_R = \sum_{m,n=1}^l u_m T_{mn}^{-1} v_n,$$

$$\text{where} \quad . \quad (3.50)$$

$$\begin{aligned} u_m &= \langle 0 | c_{x'} c_m^\dagger(-(R+y')) | 0 \rangle \\ v_n &= \langle 0 | c_n c_x^\dagger(-(R-y)) | 0 \rangle \\ T_{mn} &= \langle 0 | c_m c_n^\dagger(-2R) | 0 \rangle \end{aligned}$$

At this point, we can use the eigenvectors basis and the free fermion property (2.11) to write the generic quantity $\langle 0 | c_m c_n^\dagger(\tau) | 0 \rangle$ as

$$\begin{aligned} \langle 0 | c_m c_n^\dagger(\tau) | 0 \rangle &= \sum_{q,p=1}^{2l} S_{mq}^\dagger S_{pn} \langle 0 | d_q e^{-\tau \sum_{k=1}^{2l} \epsilon_k d_k^\dagger d_k} d_p^\dagger e^{\tau \sum_{k=1}^{2l} \epsilon_k d_k^\dagger d_k} | 0 \rangle \\ &= \sum_{q=1}^{2l} S_{mq}^\dagger S_{qn} e^{-\tau \epsilon_q}. \end{aligned} \quad (3.51)$$

This means that T , u and v can be constructed completely from the knowledge of the eigenvalues and the eigenvectors of the matrix A . Hence, if one has the algorithms to find eigenvalues and eigenvectors and compute the inverse of a matrix, the knowledge of the matrix A is enough to explicitly evaluate the two-point correlation function everywhere. This is well done by a computer. Taking the system sizes $l \gg R \gg 1$ to minimize finite-size effects, one can assume that numerical predictions for finite size are not essentially different from analytical ones for infinite size. All the numerical simulations for the density profile that are presented in this work are done following this method.

Note that, unlike the infinite-size derivation, this procedure is easily generalized to geometries different from domain wall: we have the explicit value of any $\langle 0 | c_m c_n^\dagger(\tau) | 0 \rangle$ and, since we do not need any semi-infinite Toeplitz matrices' property, we do not care if the matrix T is Toeplitz nor, in case it is, which symbol defines it.

Chapter 4

The Density Problem

4.1 Asymptotics: the starting point

In this chapter we present some examples where the representation (3.43) for the two-point correlation function can be employed to find the limit shapes of the model of fermions we introduced in Section 1.4. Incidentally, we are also going to tackle the *density problem* discussed there, namely the characterization of regions where the density (that we infer from the correlation function) is not between zero and one.

As discussed in Chapter 1, the limit shape phenomenon occurs in the scaling limit. In our particular model, the scaling limit consists in taking $R, x, y \rightarrow +\infty$, while keeping the ratios $\frac{x}{R}$ and $\frac{y}{R}$ fixed (remember the lattice horizontal size is already considered infinite). We also adapt the expression of the density to the scaling limit, defining

$$\varrho(X, Y) \equiv \lim_{R \rightarrow +\infty} \rho(XR, YR) = \lim_{R \rightarrow +\infty} \langle \psi_1 | c_{XR}^\dagger(YR) c_{XR}(YR) | \psi_1 \rangle_R, \quad (4.1)$$

where $X, Y \in \mathbb{R}$, $Y \in (-R, R)$ and $XR \in \tilde{\mathbb{Z}}$.

From (3.43), we have, in the scaling limit,

$$\varrho(X, Y) = \lim_{R \rightarrow +\infty} \int_{-\pi}^{+\pi} \frac{dk}{2\pi} \int_{-\pi}^{+\pi} \frac{dq}{2\pi} \frac{e^{iR(\varphi_\alpha(q, X, Y) - \varphi_\alpha(k, X, Y))}}{2i \sin(\frac{k-q}{2} - i0)}, \quad (4.2)$$

where

$$\varphi_\alpha(q, X, Y) \equiv qX + iY\epsilon(q) + \tilde{\epsilon}(q). \quad (4.3)$$

This representation of the correlation function is particularly convenient for the asymptotics: it is an integral formula where the large parameter R is factorized at the exponent, suitable for a saddle-point method analysis, see e.g. [54, Ch. III] and [55, Ch. VIII].

Recall that the dispersion relation for our model is

$$\epsilon(k) = -\cos(k) - \alpha \cos(2k). \quad (4.4)$$

Our analysis will be specialized to this particular dispersion relation, instead of being general as the discussion in the previous chapter. In the following, we assume $\alpha \geq 0$, since the density profile for $\alpha < 0$ can be recovered from the former thanks to the particle-hole symmetry.

Let us introduce the complex variables

$$z = e^{ik} \quad \text{and} \quad w = e^{i(q+i0)}. \quad (4.5)$$

After this substitution, we may rewrite (4.2) as

$$\varrho(X, Y) = \lim_{R \rightarrow +\infty} \int_{\mathcal{C}_z} \frac{dz}{2\pi i \sqrt{z}} \int_{\mathcal{C}_w} \frac{dw}{2\pi i \sqrt{w}} \frac{e^{R(f_\alpha(w, X, Y) - f_\alpha(z, X, Y))}}{z - w}, \quad (4.6)$$

where \mathcal{C}_z is the circumference around the origin of unitary radius, \mathcal{C}_w is a circumference around the origin with radius smaller than one and the exponent is defined as

$$f_\alpha(z, X, Y) \equiv X \ln z - \frac{1}{2} \left(z - \frac{1}{z} + \alpha \left(z^2 - \frac{1}{z^2} \right) \right) + \frac{Y}{2} \left(z + \frac{1}{z} + \alpha \left(z^2 + \frac{1}{z^2} \right) \right). \quad (4.7)$$

To write the explicit form of f_α , the Hilbert transform $\tilde{\epsilon}(k)$ was evaluated using (3.46) and the $+i0$ prescription is now hidden in the definition of the integration contours. Notice also that, during this limit operation, $XR \in \tilde{\mathbb{Z}}$; this implies that no branch points appear in the integrand; indeed

$$\frac{e^{RX \ln z}}{\sqrt{z}} = z^{XR + \frac{1}{2}} \quad (4.8)$$

is an integer power of z . Due to the analiticity properties of the integrand, the exact form of the integration contours is not essential: deforming the two contours \mathcal{C}_z and \mathcal{C}_w to homotopically equivalent curves does not change the value of the integral.

In order to show how the asymptotic behaviour of the density can be extracted from eq. (4.6), we will start finding the limit shapes for $\alpha = 0$. This will allow to understand how the computation works without the complications of the density problem, that will be tackled in the remainder of the chapter.

4.2 Pure nearest-neighbour hopping

4.2.1 Revisiting the exact formulas

Before turning to the limit shapes, it is worth to show what form the exact formulas we found in the previous chapter assume for $\alpha = 0$. For the asymptotics of

the model, the equations we already have are actually enough, but revisiting some of them adds some insight on the problem.

Let us start, then, from the result (3.21) obtained from Wick's theorem, that we write again for convenience:

$$\langle \psi_1 | c_x^\dagger(y) c_{x'}(y') | \psi_1 \rangle_R = \sum_{m,n=0}^{+\infty} u_m T_{mn}^{-1} v_n, \quad (4.9)$$

where

$$\begin{aligned} u_m &= \langle 0 | c_{x'} c_{-m-\frac{1}{2}}^\dagger(-(R+y')) | 0 \rangle, \\ v_n &= \langle 0 | c_{-n-\frac{1}{2}} c_x^\dagger(-(R-y)) | 0 \rangle, \\ T_{mn} &= \langle 0 | c_{-m-\frac{1}{2}} c_{-n-\frac{1}{2}}^\dagger(-2R) | 0 \rangle. \end{aligned} \quad (4.10)$$

Having specialized to $\epsilon(k) = -\cos(k)$, we can recognize in the various vectors and matrix elements some known special functions:

$$\begin{aligned} \langle 0 | c_m c_n^\dagger(-\tau) | 0 \rangle &= \int_{-\pi}^{+\pi} \frac{dk}{2\pi} \int_{-\pi}^{+\pi} \frac{dq}{2\pi} e^{iqm} e^{-ikn} \langle 0 | d(q) e^{-\tau H_0} d(k)^\dagger e^{\tau H_0} | 0 \rangle \\ &= \int_{-\pi}^{+\pi} \frac{dq}{2\pi} e^{iq(m-n)} e^{\tau \cos(q)} = I_{m-n}(\tau), \end{aligned} \quad (4.11)$$

where

$$I_n(z) = \int_0^\pi \frac{dk}{\pi} \cos(nk) e^{z \cos(k)} = \int_{-\pi}^{+\pi} \frac{dk}{2\pi} e^{\pm ink} e^{z \cos(z)}, \quad (4.12)$$

with $n \in \mathbb{Z}$, is the modified Bessel function [56, p. 376]. Hence everything can be formulated in terms of modified Bessel functions and the crucial point is now to compute the inverse of the semi-infinite Toeplitz matrix T whose elements are defined by modified Bessel function.

Notice also that, for $\alpha = 0$, the Wiener-Hopf decomposition of the symbol $g(k) = e^{2R \cos(k)}$ defining T can be performed explicitly without much effort: taking the logarithm, we have

$$\log g(k) = R e^{+ik} + R e^{-ik} \Rightarrow \begin{cases} \log g^+(k) = R e^{+ik} \\ \log g^-(k) = R e^{-ik} \end{cases} \Rightarrow \begin{cases} g^+(k) = e^{R e^{+ik}} \\ g^-(k) = e^{R e^{-ik}} \end{cases}. \quad (4.13)$$

Now, since we have the explicit expressions of $[(g^+)^{-1}]_m$ and $[(g^-)^{-1}]_m$, we can explicitly write the elements of T^{-1} using the semi-infinite Toeplitz matrices' property (2.32):

$$[(g^+)^{-1}]_m = \int_{-\pi}^{+\pi} \frac{dk}{2\pi} e^{-imk} e^{-R e^{+ik}} \quad , \quad [(g^-)^{-1}]_{-m} = \int_{-\pi}^{+\pi} \frac{dk}{2\pi} e^{imk} e^{-R e^{-ik}}. \quad (4.14)$$

Expanding the complex exponential, one can show that the real part of the functions under integration is even, while the imaginary part is odd; this implies that the two integrals are real and in particular

$$[(g^+)^{-1}]_m = [(g^-)^{-1}]_{-m}. \quad (4.15)$$

The integral for $[(g^+)^{-1}]_m$ can be evaluated with the residue theorem:

$$[(g^+)^{-1}]_m = \int_{-\pi}^{+\pi} \frac{dk}{2\pi} e^{-imk} e^{-Re^{ik}} = \oint \frac{dz}{2\pi i} \frac{e^{-Rz}}{z^{m+1}} = \begin{cases} \frac{(-R)^m}{m!}, & \forall m \geq 0 \\ 0, & \forall m < 0 \end{cases}. \quad (4.16)$$

So, thanks to (2.32), we end up with

$$(T^{-1})_{mn} = \sum_{r=0}^{\min(m,n)} \frac{(-R)^{m-r}}{(m-r)!} \frac{(-R)^{n-r}}{(n-l)!} \quad (4.17)$$

and, finally, from (3.21),

$$\langle \psi_1 | c_x^\dagger(y) c_{x'}(y') | \psi_1 \rangle_R = \sum_{m,n=0}^{+\infty} \sum_{r=0}^{\min(m,n)} I_{x'+m+\frac{1}{2}}(R+y') I_{n+x+\frac{1}{2}}(R-y) \frac{(-R)^{m+n-2r}}{(m-r)!(n-r)!}. \quad (4.18)$$

This relation is exact and it is interesting because every term in the sum is now explicit.

This result shows another possible (and sometimes used) approach to this kind of problems, i.e. writing everything through special functions and use their property to proceed with the computation. Moreover, it may be useful for numerical simulations of the correlation function: thanks to the property of Bessel functions

$$\lim_{n \rightarrow +\infty} I_n(\tau) = 0, \quad (4.19)$$

that holds for any finite $\tau \in \mathbb{R}^+$, the infinite sums can be truncated after a few terms. Even though the approximation gets worse and worse in the limit we are interested in ($R, x, y, x', y' \rightarrow +\infty$), meaning that we have to keep more and more terms to get the same precision, this is a good alternative option to the method described in Section 3.4. We still prefer the method of Section 3.4 because the approach with Bessel functions holds just for the particular case $\alpha = 0$, but we presented it for completeness.

4.2.2 Limit shapes

Let us finally turn to the study of the asymptotic behaviour of the density in the scaling limit for $\alpha > 0$, i.e. the evaluation of the limit

$$\varrho(X, Y) = \lim_{R \rightarrow +\infty} \int_{C_z} \frac{dz}{2\pi i \sqrt{z}} \int_{C_w} \frac{dw}{2\pi i \sqrt{w}} \frac{e^{R(f_0(w, X, Y) - f_0(z, X, Y))}}{z - w}. \quad (4.20)$$

Recall that \mathcal{C}_z and \mathcal{C}_w are two simple contours around the origin, \mathcal{C}_w is enclosed in \mathcal{C}_z and

$$f_0(z, X, Y) \equiv X \ln z - \frac{1}{2} \left(z - \frac{1}{z} \right) + \frac{Y}{2} \left(z + \frac{1}{z} \right). \quad (4.21)$$

The asymptotic analysis will be based on [13, 57].

Suppose we are able to deform \mathcal{C}_z and \mathcal{C}_w to two contours \mathcal{C}'_z and \mathcal{C}'_w respectively such that the following condition is satisfied almost everywhere¹

$$\operatorname{Re}[f_0(w, X, R) - f_0(z, X, Y)] < 0, \quad \forall z \in \mathcal{C}'_z \wedge \dot{\forall} w \in \mathcal{C}'_w. \quad (4.22)$$

Thanks to the lemma

$$\int dz g(z) \leq \int dz |g(z)|, \quad (4.23)$$

we have

$$\varrho(X, Y) \leq \lim_{R \rightarrow +\infty} \int_{\mathcal{C}'_z} \frac{dz}{2\pi\sqrt{|z|}} \int_{\mathcal{C}'_w} \frac{dw}{2\pi\sqrt{|w|}} \frac{e^{R \operatorname{Re}[f_0(w, X, Y) - f_0(z, X, Y)]}}{|z - w|}, \quad (4.24)$$

which, under (4.22), vanishes. The crucial point in this asymptotic analysis will be to find such deformation.

In the process of deformation, it is important to consider the singularities of the function under integration, namely the origin and the pole in $z = w$. In particular, the pole in $z = w$ means that, whenever the two integration contours cross, we have to consider an additional contribution to the integral that can be evaluated using the residue theorem.

In order to find the points for which condition (4.22) holds, we study the real-valued function of real variables

$$u(a, b) \equiv \operatorname{Re}[f_0(a+ib, X, Y)] = \frac{1}{2} X \log(a^2 + b^2) + \frac{aY}{2(a^2 + b^2)} + \frac{a}{2(a^2 + b^2)} + \frac{aY}{2} - \frac{a}{2}, \quad (4.25)$$

starting with the description of its stationary points.

From complex analysis, see e.g. [54], we know that, where $f_0(z)$ is analytic, the stationary points of u can be only saddle points and they correspond to stationary points of $f_0(z)$. The equation for the stationary points of f_0 is

$$0 = \frac{\partial}{\partial z} f_0(z, X, Y) = -\frac{1}{2z^2} \left((1-Y)z^2 - 2Xz + 1 + Y \right). \quad (4.26)$$

Once we exclude the origin from the possible solutions, the equation above is equivalent to the polynomial equation

$$(1-Y)z^2 - 2Xz + 1 + Y = 0, \quad (4.27)$$

¹By almost everywhere, we mean everywhere except at most a set of null measure. To represent this in symbols, we use $\dot{\forall}$.

with the two solutions

$$z = \frac{X \pm \sqrt{-1 + X^2 + Y^2}}{1 - Y} \quad \text{for } X^2 + Y^2 > 1, \quad (4.28)$$

$$z = \frac{X \pm i\sqrt{1 - X^2 - Y^2}}{1 - Y} \quad \text{for } X^2 + Y^2 \leq 1. \quad (4.29)$$

We can identify three regimes, according to the type of saddle points we get in function of X and Y . Noticing that, when the two saddle points are real, they have both the same sign of X (recall $-1 < Y < 1$) we define:

- *Regime I* the case $X^2 + Y^2 > 1 \wedge X > 0$, where the two saddle points are real and positive;
- *Regime II* the case $X^2 + Y^2 \leq 1$, where the two saddle points are complex conjugated;
- *Regime III* the case $X^2 + Y^2 > 1 \wedge X < 0$, where the two saddle points are real and negative.

Turning back to the problem of deforming the contours, we consider initially Regime I and only the saddle point

$$a_1 \equiv \frac{X + \sqrt{-1 + X^2 + Y^2}}{1 - Y}. \quad (4.30)$$

We define a blue (orange) region in the plane a, b as the region of the plane where $u(a, b)$ is bigger (smaller) than $u(a_1, 0)$. One can show that, for any X and Y in Regime I, the two regions are qualitatively similar to the ones represented in 4.1a, i.e. one can prove that the level curves with value $u(a_1, 0)$ intersect the negative real semi-axis just once and the positive real semi-axis only in the saddle point a_1 .

By transitivity, u is greater in the blue region than in the orange region. This implies that, if we take a contour \mathcal{C}'_z in the blue region and a contour \mathcal{C}'_w in the orange one, the condition (4.22) is satisfied. Since the original contours \mathcal{C}_z and \mathcal{C}_w can be deformed to these new contours without intersecting (\mathcal{C}'_z and \mathcal{C}'_w are still simple contours around the origin and \mathcal{C}'_w is enclosed in \mathcal{C}'_z as \mathcal{C}_w was enclosed in \mathcal{C}_z), we conclude that the double integral gives zero in the scaling limit. A possible choice of contours \mathcal{C}'_z and \mathcal{C}'_w is showed in the figure.

Before going on, let us make a disclaimer about the role of the saddle point in this deformation. First of all, notice that we are not using the saddle-point method: our deformed contours need not be the steepest descent paths in the neighbourhood of the saddle point; in fact, we used the saddle point just as a convenient way to define the coloured regions. To understand this point, consider $\bar{u} \in \mathbb{R}$ and define the blue and the orange regions such that $u(a, b) > \bar{u}$ and $u(a, b) < \bar{u}$ respectively;

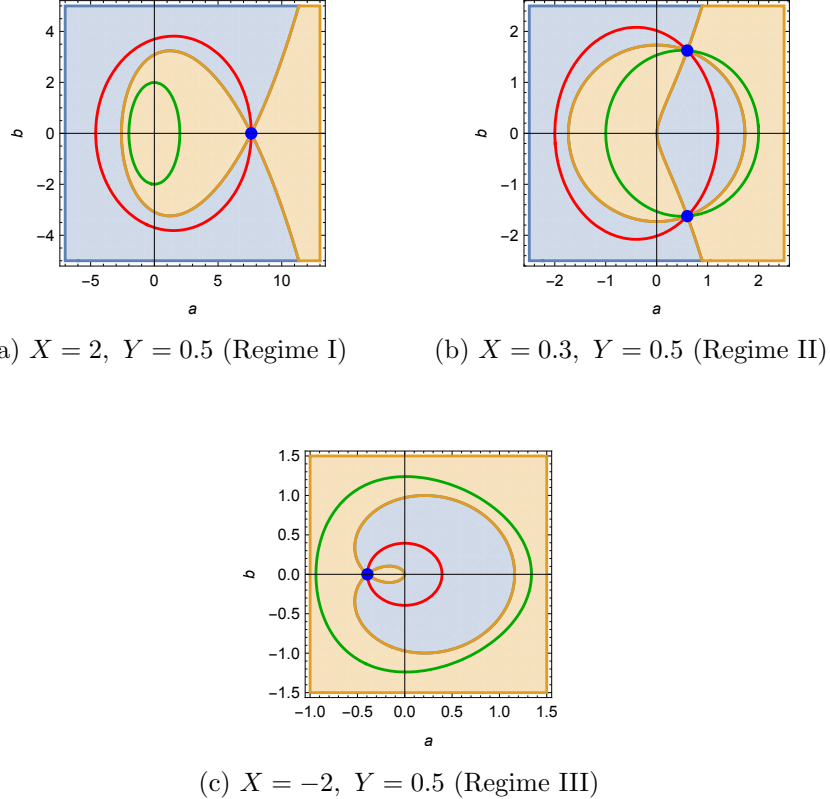


Figure 4.1: Plots of $u(a, b) \equiv \text{Re}[f_0(a + ib, X, Y)]$ for different values of X, Y . The blue points represent the location of the saddle point chosen as benchmark (in Regime II there are two saddle points because u has the same value in both of them). The blue (orange) regions of the plane are those for which $u(a, b)$ is bigger (smaller) than u evaluated in the benchmark saddle point. The red and the green lines represent the integration contours \mathcal{C}'_z and \mathcal{C}'_w respectively, obtained by the deformation described in the text; by definition of the coloured regions, all the points (a, b) belonging to the red line have $u(a, b)$ bigger than all the points belonging to the green line. Every plot of this kind in the respective regime looks qualitatively the same.

if it is possible to close two simple contours around the origin \mathcal{C}'_z and \mathcal{C}'_w such that the first is enclosed in the blue region and the second is enclosed in the orange one, then we can draw the same conclusion about the density going to zero in the limit without having even mentioned the saddle points (the condition (4.22) would still be satisfied). Taking $\bar{u} = u(a_1, 0)$ is convenient, but it is not the only possibility: we used it to show that at least one value \bar{u} such the one described above exists and this is what is important to state that the density goes to zero.

Let us now consider Regime II. We have two saddle points, $z_1 \equiv a_1 + ib_1$ and $z_2 \equiv z_1^* = a_1 - ib_1$, with $a_1 = \frac{X}{1-Y}$ and $b_1 = \frac{\sqrt{1-X^2-Y^2}}{1-Y}$. Since $u(a, b)$ is even in b , it takes the same value in the two saddle points. It can be shown that, for any value of X and Y in this regime, a construction similar to the one reported in Fig.4.1b holds. As in Regime I, we can draw two contours \mathcal{C}'_z and \mathcal{C}'_w such that the first is enclosed in the blue region and the second is enclosed in the orange one, but this time the deformation requires the two contours to cross each other, so we have to carefully consider the residue contribution in the deformation.

To evaluate the residue contribution let us consider the integral in w for some fixed z . During the deformation of the integration contour, if the pole in z is crossed, a new singularity is included inside the integration contour and to correctly account for this we should subtract its residue contribution:

$$\int_{\mathcal{C}_1} dw \frac{f(w)}{w-z} = \int_{\mathcal{C}_2} dw \frac{f(w)}{w-z} - 2\pi i \text{Res}_z \frac{f(w)}{w-z} = \int_{\mathcal{C}_2} dw \frac{f(w)}{w-z} - 2\pi i f(z), \quad (4.31)$$

where \mathcal{C}_1 is a contour that does not include z , \mathcal{C}_2 is a contour that includes z and f is a generic function that is analytic in the neighbourhood of z . Hence, during the deformation we pick up the residue of the integrand at $z = w$ whenever we push the z -contour inside the the w -contour, so that

$$\varrho(X, Y) = \lim_{R \rightarrow +\infty} \int_{\mathcal{C}'_z} \frac{dz}{2\pi i \sqrt{z}} \int_{\mathcal{C}'_w} \frac{dw}{2\pi i \sqrt{w}} \frac{e^{R(f_0(w, X, Y) - f_0(z, X, Y))}}{z-w} + \int_{\gamma} \frac{dz}{2\pi i z}, \quad (4.32)$$

where γ is a curve that connects the two saddle points passing on the right of the origin (and without wrapping around it) because of the singularity.

The double integral now gives zero in the scaling limit because condition (4.22) is satisfied. The other integral can be evaluated choosing, for instance, γ as the arc of circumference of radius $\sqrt{\frac{1-Y}{1+Y}}$ centred in the origin connecting the two saddle points. So in the end

$$\varrho(X, Y) = \int_{\gamma} \frac{dz}{2\pi i z} = 2 \int_0^{\arccos\left(\frac{X}{\sqrt{1-Y^2}}\right)} \frac{d\theta}{2\pi} = \frac{1}{\pi} \arccos\left(\frac{X}{\sqrt{1-Y^2}}\right). \quad (4.33)$$

Notice that the density is simply related to the argument of the saddle points, i.e. $\varrho(X, Y) = \text{Arg}(z_1)/\pi$. There are alternative methods, such as the hydrodynamic

approach, to obtain the density in the fluctuating region that relies on this fact, see e.g. [28].

Finally, Regime III can be treated similarly. The typical coloured regions are shown in Fig. 4.1c. The deformation we are looking for is possible and it essentially requires to exchange the two contours. Along the line of the computation done for Regime II one can show that

$$\varrho(X, Y) = 2 \int_0^\pi \frac{d\theta}{2\pi} = 1 \quad (4.34)$$

for any X, Y in Regime III. Notice that this is the maximum value that we can get from the residue contribution because it is an increasing function of the portion of the contours that is exchanged in the deformation, so it is maximum when the two contours are completely exchanged.

Putting everything together, we have the following result for $\alpha = 0$ and imaginary time $y \in (-R, R)$:

$$\boxed{\varrho(X, Y) = \begin{cases} 0, & X^2 + Y^2 \geq 1 \wedge X \geq 0 \\ \frac{1}{\pi} \arccos \left(\frac{X}{\sqrt{1 - Y^2}} \right), & X^2 + Y^2 < 1 \\ 1, & X^2 + Y^2 \geq 1 \wedge X < 0 \end{cases}}. \quad (4.35)$$

This result was already known [17, 58], but we obtained it with a different asymptotic analysis. The density profile is presented in Fig. 4.2.

Summarizing, we have learned that, when a deformation such as the one described above is possible, the contribution from the residues gives the finite part of ρ , which takes values between zero and one. This will be the guiding idea to tackle the asymptotic study of the generic- α case too.

One last remark before going on. We saw how different regimes correspond to different possibilities for the density: in Regime I the density is zero, in the second it is between zero and one and in the third it is one. As a consequence, the interfaces between the regimes are nothing less than the arctic curves. Now, the regimes can be identified simply looking at the discriminant of the polynomial involved in the saddle-point equation (and the sign of X), since when it is positive we have two real solutions and when it is negative we have two imaginary solutions: the interfaces between regimes are just the zeros of the discriminant. We conclude that, if one is interested only in the arctic curve and not on the precise value of the density in the fluctuating region, it is sufficient to look at the discriminant. We will see in the following that the discriminant is not enough to find the arctic curves for generic α .

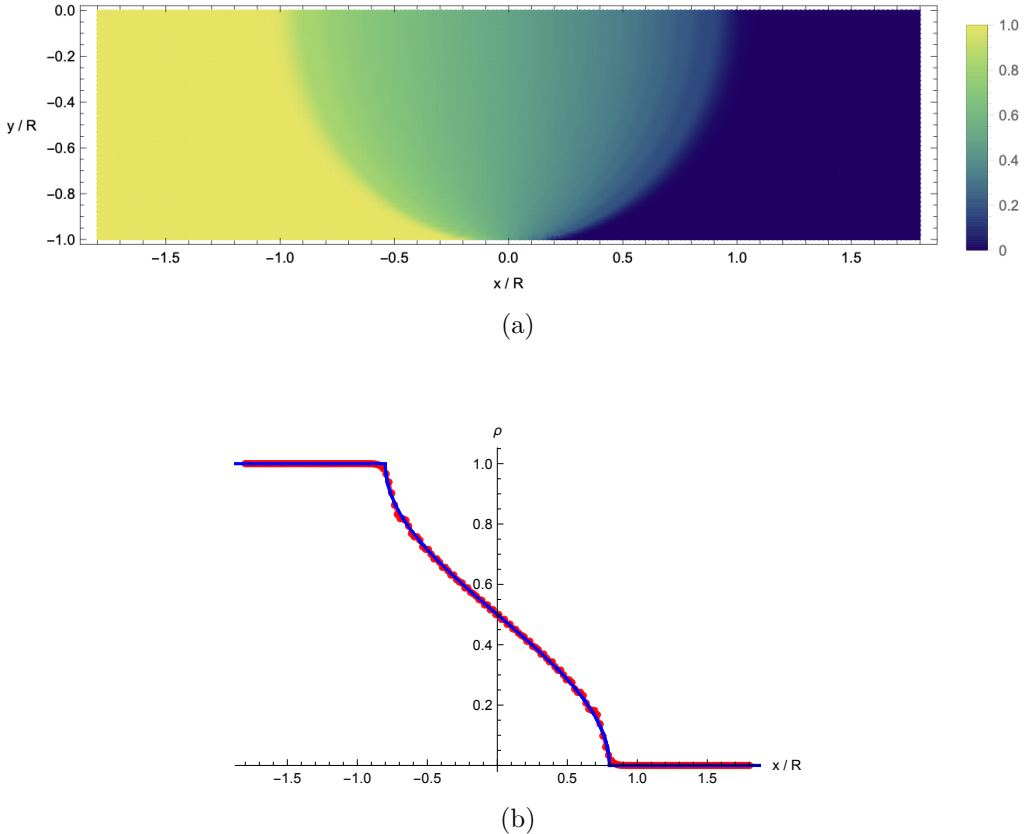


Figure 4.2: Density profile for pure NN hopping. (a): Density profile for a finite-size system, obtained as explained in Section 3.4. Only half of the imaginary time is presented, since the other half is just a reflection with respect to the axis $Y = 0$. (b): Density profile for the time slice $Y = -3/5$. The blue line is the theoretical prediction, while the red points are obtained in finite size.

4.3 Density profile at zero time

We now turn to $\alpha \neq 0$. Before discussing the full density profile for generic α , let us focus for simplicity on the time slice $Y = 0$.

We consider the density expressed as a double integral in real variables, as in (4.2):

$$\varrho(X, 0) = \lim_{R \rightarrow +\infty} \int_{-\pi}^{+\pi} \frac{dk}{2\pi} \int_{-\pi}^{+\pi} \frac{dq}{2\pi} \frac{e^{iR(\varphi_\alpha(q, X, 0) - \varphi_\alpha(k, X, 0))}}{2i \sin(\frac{k-q}{2} - i0)}, \quad (4.36)$$

with

$$\varphi_\alpha(q, X, 0) \equiv qX - \sin(q) - \alpha \sin(2q). \quad (4.37)$$

We will not need the properties of complex integration that we used in the previous section.

The asymptotic of this kind of integrals in the limit $R \rightarrow +\infty$ is usually studied via the stationary-phase approximation, the exponent being purely imaginary; see e.g. [59]. In our case, we do not need to apply the approximation in details: it is enough to know that, from the stationary-phase approximation, any integral of the form

$$\int dx e^{iRh(x)} g(x) \quad (4.38)$$

goes to zero for $R \rightarrow +\infty$, if g and h are suitably regular functions. Thus, in the large R limit, the only non-vanishing contribution to the density may rise from the singularity of the integral, i.e. the points $k \simeq q$. So we can compute the density expanding over $p \equiv \frac{k-q}{2}$:

$$\begin{aligned} \varrho(X, 0) &= \lim_{R \rightarrow +\infty} \int_{-\pi}^{+\pi} \frac{dk}{2\pi} \int_{-\pi}^{+\pi} \frac{dp}{2\pi i} \frac{e^{-2iRp \frac{\partial}{\partial k} \varphi_\alpha(k, X, 0)}}{p - i0} \\ &= \lim_{R \rightarrow +\infty} \int_{-\pi}^{+\pi} \frac{dk}{2\pi} \int_{-\infty}^{+\infty} \frac{dp}{2\pi i} \frac{e^{-2iRp \frac{\partial}{\partial k} \varphi_\alpha(k, X, 0)}}{p - i0} \\ &= \int_{-\pi}^{+\pi} \frac{dk}{2\pi} \Theta\left(-\frac{\partial}{\partial k} \varphi_\alpha(k, X, 0)\right), \end{aligned} \quad (4.39)$$

where we used the integral representation of the Heaviside step function

$$\Theta(x) = \int_{-\infty}^{+\infty} \frac{d\tau}{2\pi i} \frac{e^{i\tau x}}{\tau - i0}. \quad (4.40)$$

Now everything boils down to study the sign of $\frac{\partial \varphi_\alpha}{\partial k}$:

$$-\frac{\partial \varphi_\alpha}{\partial k} > 0 \iff 4\alpha \cos^2(k) + \cos(k) - X - 2\alpha > 0, \quad (4.41)$$

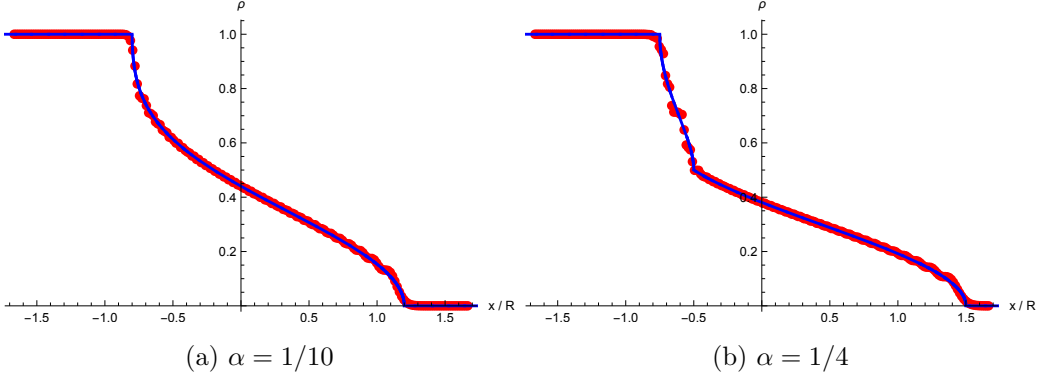


Figure 4.3: Density profile in our model for null imaginary time. The blue line is the theoretical prediction, while the red points are obtained from a numerical simulation in finite size as described in Section 3.4.

which holds for

$$\cos(k) > \frac{-1 + \sqrt{1 + 16X\alpha + 32\alpha^2}}{8\alpha} \quad \vee \quad \cos(k) < \frac{-1 - \sqrt{1 + 16X\alpha + 32\alpha^2}}{8\alpha}. \quad (4.42)$$

Clearly, the second equation has solutions only if $\alpha > \alpha_c \equiv \frac{1}{8}$. The critical value α_c separates two different behaviours for the density and will play an important role in the general-imaginary-time case as well. Completing the computation, we get that the density profile for $\alpha < \alpha_c$ is

$$\varrho(X, 0) = \begin{cases} 0 & , \quad 1 + 2\alpha \leq X \\ \frac{1}{\pi} \arccos \left(\frac{-1 + \sqrt{1 + 32\alpha^2 + 16X\alpha}}{8\alpha} \right) & , \quad -1 + 2\alpha < X < 1 + 2\alpha \\ 1 & , \quad X \leq -1 + 2\alpha \end{cases}, \quad (4.43)$$

while for $\alpha > \alpha_c$ is

$$\varrho(X, 0) = \begin{cases} 0 & , \quad +1 + 2\alpha \leq X \\ \frac{1}{\pi} \arccos \left(\frac{-1 + \sqrt{1 + 32\alpha^2 + 16X\alpha}}{8\alpha} \right) & , \quad -1 + 2\alpha \leq X < +1 + 2\alpha \\ 1 + \frac{1}{\pi} \arccos \left(\frac{-1 + \sqrt{1 + 32\alpha^2 + 16X\alpha}}{8\alpha} \right) - \frac{1}{\pi} \arccos \left(\frac{-1 - \sqrt{1 + 32\alpha^2 + 16X\alpha}}{8\alpha} \right) - \frac{1+32\alpha^2}{16\alpha} & , \quad -\frac{1+32\alpha^2}{16\alpha} < X < -1 + 2\alpha \\ 1 & , \quad X \leq -\frac{1+32\alpha^2}{16\alpha} \end{cases}. \quad (4.44)$$

Examples of the density profiles in the two cases are reported in Fig. 4.3.

By this simple method we are already able to evaluate the density profile in the scaling limit for generic α and imaginary time $Y = 0$. Unfortunately, the argument we used in this section strongly relied on the exponent being imaginary, so that we

have to adopt a different strategy for generic imaginary time. Anyway, this result provides a useful check for the prediction of the general treatment that we shall present in the next section, since the two methods must give the same results for $Y = 0$.

4.4 Full limit shapes

Let us now consider the density profile in our model for a generic imaginary time Y and $\alpha \neq 0$. The idea is trying to apply the same argument of contour deformation that we used for $\alpha = 0$. We will see that the complication in the saddle-point equation due to the presence of the NNN hopping term brings a new feature in the computation. Many of the following results were obtained using computer algebra systems and their explicit expression is messy more than instructive, so we omitted several intermediate passages, focusing on the underlying idea. Various figures will be shown to help visualize the general argument.

Let us recall that

$$\varrho(X, Y) = \lim_{R \rightarrow +\infty} \int_{\mathcal{C}_z} \frac{dz}{2\pi i \sqrt{z}} \int_{\mathcal{C}_w} \frac{dw}{2\pi i \sqrt{w}} \frac{e^{R(f_\alpha(w, X, Y) - f_\alpha(z, X, Y))}}{z - w}, \quad (4.45)$$

where \mathcal{C}_w is enclosed in \mathcal{C}_z and

$$f_\alpha(z, X, Y) \equiv X \ln z - \frac{1}{2} \left(z - \frac{1}{z} + \alpha \left(z^2 - \frac{1}{z^2} \right) \right) + \frac{Y}{2} \left(z + \frac{1}{z} + \alpha \left(z^2 + \frac{1}{z^2} \right) \right). \quad (4.46)$$

We try to deform the contours of integration to two contours \mathcal{C}'_z and \mathcal{C}'_w in such a way that the phase obeys the following condition (analogous to (4.22)) almost everywhere:

$$\text{Re}[f_\alpha(w, X, Y) - f_\alpha(z, X, Y)] < 0, \quad \forall z \in \mathcal{C}'_z \wedge \forall w \in \mathcal{C}'_w. \quad (4.47)$$

If this condition holds, we can claim that the double integral is zero in the scaling limit and the finite part of the density is given by the potential residue contribution.

What changes with respect to the $\alpha = 0$ case is that, as we will see, there are values of X, Y for which such deformation is not possible, i.e. there are some values X, Y for which we cannot find a combination of contours such that (4.47) holds. We will see that for these values the double integral diverges.

To investigate the possibility to perform the deformation, we study the real function of real variables $u(a, b) \equiv \text{Re}[f_\alpha(a + ib, X, Y)]$. The saddle-point equation reads now

$$0 = \frac{\partial}{\partial z} f_\alpha(z, X, Y) = 2\alpha(1-Y)z^4 + (1-Y)z^3 - 2Xz^2 + (1+Y)z + 2\alpha(1+Y); \quad (4.48)$$

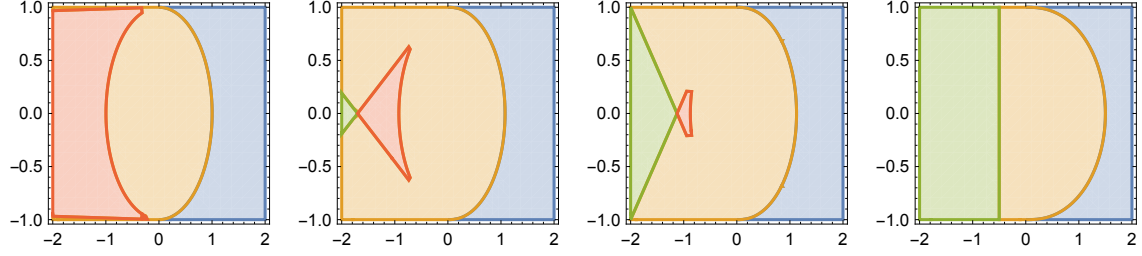


Figure 4.4: The four possible connected regions identified by the sign of the discriminant of the saddle-point equation. The plots have X on the horizontal line and Y on the vertical one and differ in the value of α : $\alpha = 1/1000, 1/26, 1/16, 1/4$ from left to right.

recall that the origin, being a singularity, is excluded from the possible solutions.

Being a quartic equation with real coefficients, the saddle-point equation is still exactly solvable, with explicit expressions for its solutions. In general, there are four different saddle points, so it is clear that the panorama of the solutions will be richer than for $\alpha = 0$.

First of all, we can define the various regimes, similarly to what we did for $\alpha = 0$, according to the nature of the saddle points we get in function of X and Y , i.e. if the saddle points are all real or there are one or two couples of complex-conjugated solutions. This can be done via the discriminant: for a quartic polynomial whose coefficients are real numbers, the discriminant is zero if two or more roots are equal, it is negative if there are two real roots and two complex conjugate roots, and it is positive if the roots are either all real or all non-real. The discriminant's sign of the polynomial involved in the saddle-point equation (for fixed $\alpha > 0$) gives four different connected regions, as shown in Fig. 4.4. We define:

- *Regime I* the region of the X, Y plane for which all the saddle points are real and $X \geq 0$ (blue in the figure);
- *Regime II* the region of the X, Y plane for which two of the saddle points are real and two are not (yellow in the figure);
- *Regime III* the region of the X, Y plane for which all the saddle points are real and $X \leq 0$ (red in the figure);
- *Regime IV* the region of the X, Y plane for which all the saddle points are not real (green in the figure).

Comparing with the pure NN hopping case, Regime IV has no counterpart, while the others tend to the respective regimes for $\alpha \rightarrow 0$.

It can be shown that for $\alpha > \alpha_c \equiv 1/8$, Regime III disappears. It is not a coincidence that it is the same critical value we encountered in the previous section in the computation of $\varrho(X, 0)$, as we shall see later on.

Notice that there is no trace of ill-behaviour of the density in the plot of the discriminant, i.e. we cannot recognize the limit shapes of regions with ill-defined density in the areas delimited by the discriminant's sign. This means that the fact that two saddle points develop (or loose) an imaginary part cannot characterize the limit shapes we are interested in: unlike what happened for $\alpha = 0$, finding the zeros of the discriminant will not be enough to describe the arctic curves. (Anyway, we will see that the interface between frozen regions and normally-fluctuating ones is still described by zeros of the discriminant, as can also be heuristically inferred from Fig. 4.4, where the separation between yellow and blue regions and the rightmost interface between red and yellow regions give the limit shapes that one observes in numerical simulations.)

Once all the saddle points are computed, the idea is to deform the integration contours in the way described for $\alpha = 0$, so that (4.47) holds. To find such deformation, we choose a saddle point $z_0 = a_0 + ib_0$, where $a_0, b_0 \in \mathbb{R}$, and shade in blue (resp. orange) the regions where $u(a, b) > u(a_0, b_0)$ (resp. $u(a, b) < u(a_0, b_0)$) in the plane a, b . Then let us explore the possibility to draw two contours around the origin such that one is enclosed in the blue region and the other in the orange one; if this is possible, even for just one saddle point, then the deformation we are looking for is possible. Let us examine this possibility regime by regime.

In Regime I and Regime III, nothing essentially changes with respect to the corresponding regimes of the pure NN hopping case: it is always possible to find a saddle point for which Fig. 4.1a and Fig. 4.1c hold, giving a value for the density of zero and one respectively.

Let us consider Regime II. For those points whose X is close (in a sense that will be specified soon) to Regime I the situation is actually not essentially different from the pure NN hopping case, as represented in Fig. 4.5a (compare it with Fig. 4.1b). Hence here the deformation is still possible and gives a finite result from the residue contribution. But, choosing Y_0 such that the line $Y = Y_0$ never enters Regime III, there are always some values of X in Regime II such that it is impossible to draw a contour as desired. What changes is the relation between the saddle points: referring to Fig. 4.5b, we see that $\text{Re}[f_\alpha]$ of the red saddle point is bigger than $\text{Re}[f_\alpha]$ of the blue ones, disabling the possibility to close a contour in the orange region (remember that we are not allowed to draw contours across the origin, since it is singular). One can show that we cannot close the contour as desired even considering the other saddle points as the benchmark to shade the regions in the picture.

The value of the integral for those X, Y that do not allow to close the contour as we want can be approximated using the saddle-point method. The explicit computation is reported in Appendix A and gives, for large R ,

$$\varrho(X, Y) \sim e^{R(\text{Re}[f_\alpha(a_3, X, Y) - f_\alpha(z_1, X, Y)])} \text{Im} \left[\frac{e^{-iR \text{Im}[f_\alpha(z_1, X, Y)]} e^{i\varphi}}{\sqrt{z_1}(a_3 - z_1)} \right], \quad (4.49)$$

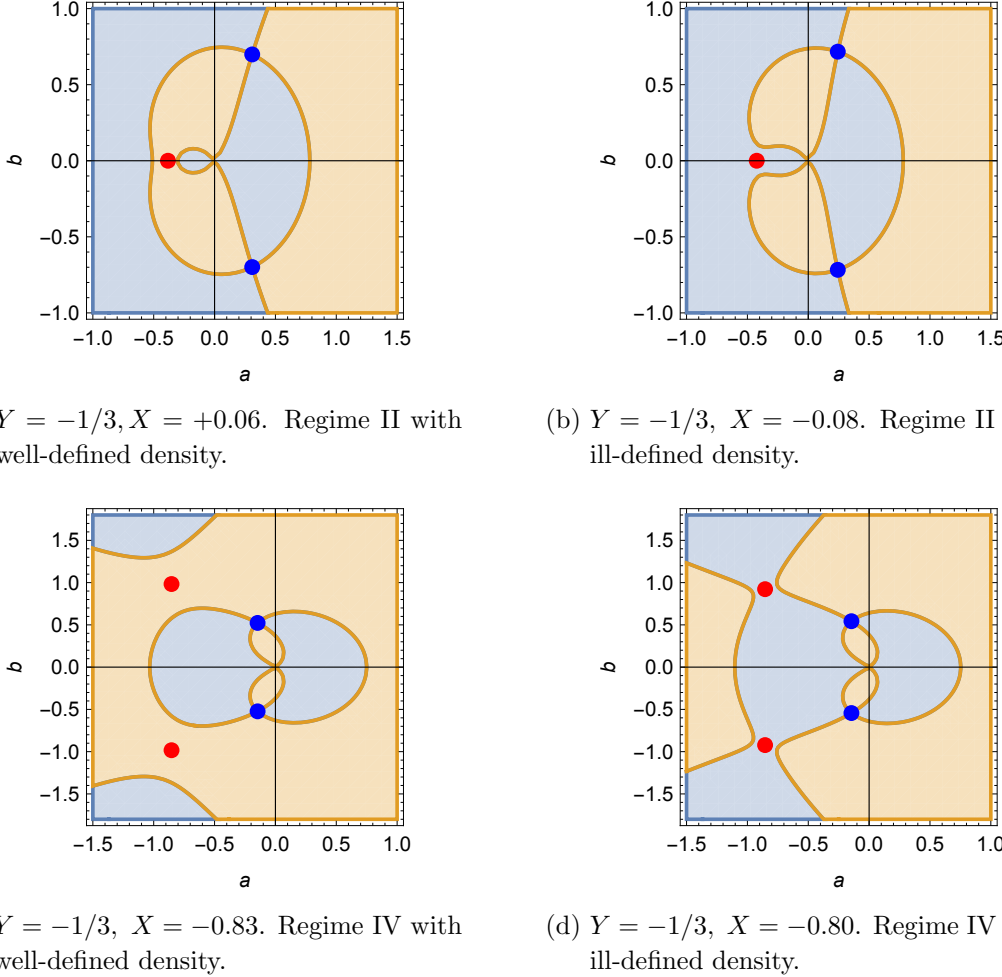


Figure 4.5: Representations of $u(a, b) \equiv \text{Re}[f_\alpha(a + ib, X, Y)]$ in Regime II (top) and Regime IV (bottom) for $\alpha = 1/4$. The coloured points represent the saddle points (in Regime II one point is too far on the left to enter the picture); we drew with the same colour the couples of complex-conjugated saddle points. The blue (orange) region represents the region of the plane (a, b) where $u(a, b)$ is bigger (smaller) than u evaluated in the blue saddle points. In the configurations (a) and (c) we can trace a contour enclosed in the blue region and a contour enclosed in the orange region; this means that a deformation that satisfies condition (4.47) exists and the density is between zero and one. In the configurations (b) and (d) it is not possible to close a contour in the orange region: this represents the typical situation for points X, Y with an ill-defined density.

where a_3 is the closest saddle point to the origin on the negative real semi-axis, z_1 is the saddle point in the lower half plane and $\varphi \in (-\pi/2, \pi/2)$ is a phase such that

$$\operatorname{Arg} \left[\frac{\partial^2}{\partial z^2} f_\alpha(z, X, Y) \Big|_{z=z_1} \right] + 2\varphi = 2n\pi, \quad (4.50)$$

for some $n \in \mathbb{Z}$. Since $\operatorname{Re}[f_\alpha(a_3, X, Y) - f_\alpha(z_1, X, Y)] > 0$, this proves the divergence of the density in the regions where it is not between zero and one.

Notice also that the frequency of oscillations grows with R because of the factor $\operatorname{Im} \left[\frac{e^{-iR \operatorname{Im}[f_\alpha(z_1, X, Y)]} e^{i\varphi}}{\sqrt{z_1}(a_3 - z_1)} \right]$. This implies that ρ violently oscillates between $+\infty$ and $-\infty$, meaning that the precise limit ρ does not even exist in these regions. Note that the oscillating behaviour was expected from the conservation of the particle number that we noticed in Section 1.4, since, heuristically, we need a $-\infty$ to compensate each $+\infty$ to keep the number of particles the same we started with.

The same application of the saddle-point method could also be done in the case, described Fig. 4.5a, where the density is well defined. What changes is the relation between the saddle points, which is inverted. One would find that the double integral goes exponentially fast to zero. Of course, this does not imply that the density is zero because of the residue contribution.

However, these are not all the possibilities that are encountered in Regime II. If X_0, Y_0 is a point of Regime II where the density is not well defined, it can happen that there is a range of X smaller than X_0 that, for the same Y_0 , allows the deformation we are looking for. In particular, this configuration of the saddle points requires the two contours to completely exchange, giving a final density equal to one. An example of this type of configuration is represented in Fig. 4.6. Notice the difference with the $\alpha = 0$ case: there, each regime was either frozen or fluctuating; here, in the same regime, we can have a piece of fluctuating region, a piece of frozen region and a piece of the region where the density is not well-defined. This characteristic, clearly due to the richness of the saddle points scenario that one has, also implies that the discriminant is not enough to characterize the arctic curves: the nature of the saddle points never changes within Regime II, but there may be different arctic curves separating three different phases.

Finally, let us consider Regime IV. It can be proved that, for $\alpha > 0$ and any fixed $Y = Y_0$, there is always a value of the position X_0 such that any point (X, Y_0) belongs to Regime IV if and only if $X < X_0$. For values of X in Regime IV that are enough on the left (in a sense that will be specified soon), we are not that far from the configuration that gives a density equal to one in Regime III of the pure NN hopping case, as reported in Fig. 4.5c (compare it with Fig. 4.1c). For such points, then, the density equals one. But also here for some value of X, Y it can happen that the saddle-points morphology changes and the possibility to close the contour as we want disappears, as shown in Fig. 4.5d. By a similar saddle-point method application

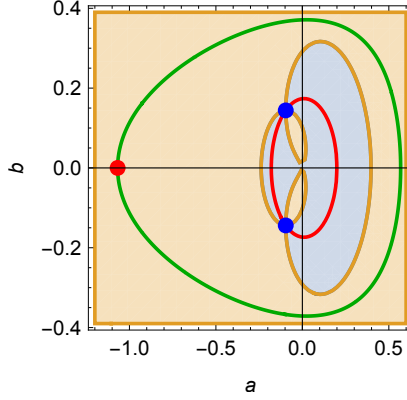


Figure 4.6: Representation of $u(a, b) \equiv \text{Re}[f_\alpha(a + ib, X, Y)]$ for $\alpha = 1/15$, $Y = -2/3$, $X = -0.9$. For some points of Regime II, a deformation like this is possible, giving a density equal to one. The blue points represent again a couple of complex conjugated saddle points, while the red point is a third one (the fourth saddle point is far on the negative real semi-axis).

to the one we did for Regime II, it can be shown that the density for such points diverges exponentially and has the same oscillating behaviour of the divergence in Regime II. So we can see different behaviours for the density in Regime IV as well: it can be either 1 or ∞ (but, differently from Regime II, not in the interval $(0, 1)$).

Let us summarize what we found. First of all, the density in the point (X_0, Y_0) can be ill-defined only if (X_0, Y_0) belongs to either Regime II or Regime IV. For any imaginary time $Y_0 \neq 0$, there exists X_0 such that (X_0, Y_0) is one of such point if and only if the line $Y = Y_0$ does not intersect Regime III. The density for the point (X_0, Y_0) is ill-defined if it is impossible to deform the integration contours in the way described above. The signature of this impossibility is $\text{Re}[f_\alpha]$ of a certain saddle point (red in Fig. 4.5) being bigger than $\text{Re}[f_\alpha]$ of a certain other one (blue in Fig. 4.5). After having identified the saddle points (recall that they have an explicit expression), it is thus sufficient to compare $\text{Re}[f_\alpha]$ between them to characterize the region where the density is ill-defined. We can test the condition numerically on an arbitrary dense grid of points in the space X, Y to find our theoretical prediction of the limit shape for the regions with ill-defined density. A comparison with the numerical simulation in finite size is shown in Fig. 4.7.

Notice that, since for $\alpha > \alpha_c$ Regime III disappears, as soon as $\alpha > \alpha_c$ the regions of ill-definition for the density touch the axis $Y = 0$. Combined with the previous observations about α_c , we have that, $\forall X \in [-1 + 2\alpha, +1 + 2\alpha)$ and $Y = 0$, there is a neighbourhood of $(X, 0)$ where the density is well-defined.

To conclude, let us say something more about the points with well-defined density. For such points, the density is still between zero and one and can be computed in the same way we obtained the density for $\alpha = 0$: after the deformation we are left with a double integral that gives zero in the scaling limit and a simple inte-

gral accounting for the residue contribution. It is not hard to evaluate the latter, properly choosing the integration contours; but, given the messy expression of the saddle points, we think it is not worth it to report the explicit result. Instead, we just present the plot in Fig. 4.7.

4.5 Pure next-nearest-neighbour hopping limit

In the previous section we saw that, starting with $\alpha = 0$ and turning on the NNN hopping term in the Hamiltonian, the regions where the density is not well-defined grow bigger and bigger. For $\alpha > \alpha_c$, we even found that the only imaginary time for which density $\varrho(X, Y)$ is well defined $\forall X$ is $Y = 0$. In Section 1.4 we have shown that in the case of pure NNN hopping the density is well-defined everywhere. Since these two statements seem in contrast, it is interesting to look at what happens in the limit $\alpha \rightarrow \infty$.

In order to evaluate the limit $\alpha \rightarrow \infty$, it is convenient to rescale the Hamiltonian, so that it does not diverge in the limit, while it still yields H_α at small α . We thus introduce the Hamiltonian

$$\begin{aligned} H' &= -\frac{1}{2\sqrt{1+\alpha^2}} \sum_{x \in \tilde{\mathbb{Z}}} \left(c_x^\dagger c_{x+1} + c_{x+1}^\dagger c_x + \alpha c_x^\dagger c_{x+2} + \alpha c_{x+2}^\dagger c_x \right) \\ &\simeq -\frac{1}{2} \sum_{x \in \tilde{\mathbb{Z}}} \left(\beta c_x^\dagger c_{x+1} + \beta c_{x+1}^\dagger c_x + c_x^\dagger c_{x+2} + c_{x+2}^\dagger c_x \right), \end{aligned} \quad (4.51)$$

with $\beta \equiv 1/\alpha$.

The computation goes on as in the last section. All the integration contours arguments still hold and one can show that the regions with ill-defined density tend to occupy all the fluctuating region (a comparison between the theoretical prediction and the numerical simulation is presented in Fig. 4.8). In the limit $\beta \rightarrow 0$ the density of the model is either one, zero or divergent (no fluctuating region).

On the other hand we know that starting directly with the NNN hopping term alone in the Hamiltonian, the density would be well-defined everywhere. We conclude that the scaling limit and the limit $\beta \rightarrow 0$ do not commute and this solves the possible ambiguity arising in combining the two previous statements. This issue with the order of limits reflects in a milder divergence for the scaling limit density as β goes to zero (it still diverges, though).

CHAPTER 4. THE DENSITY PROBLEM

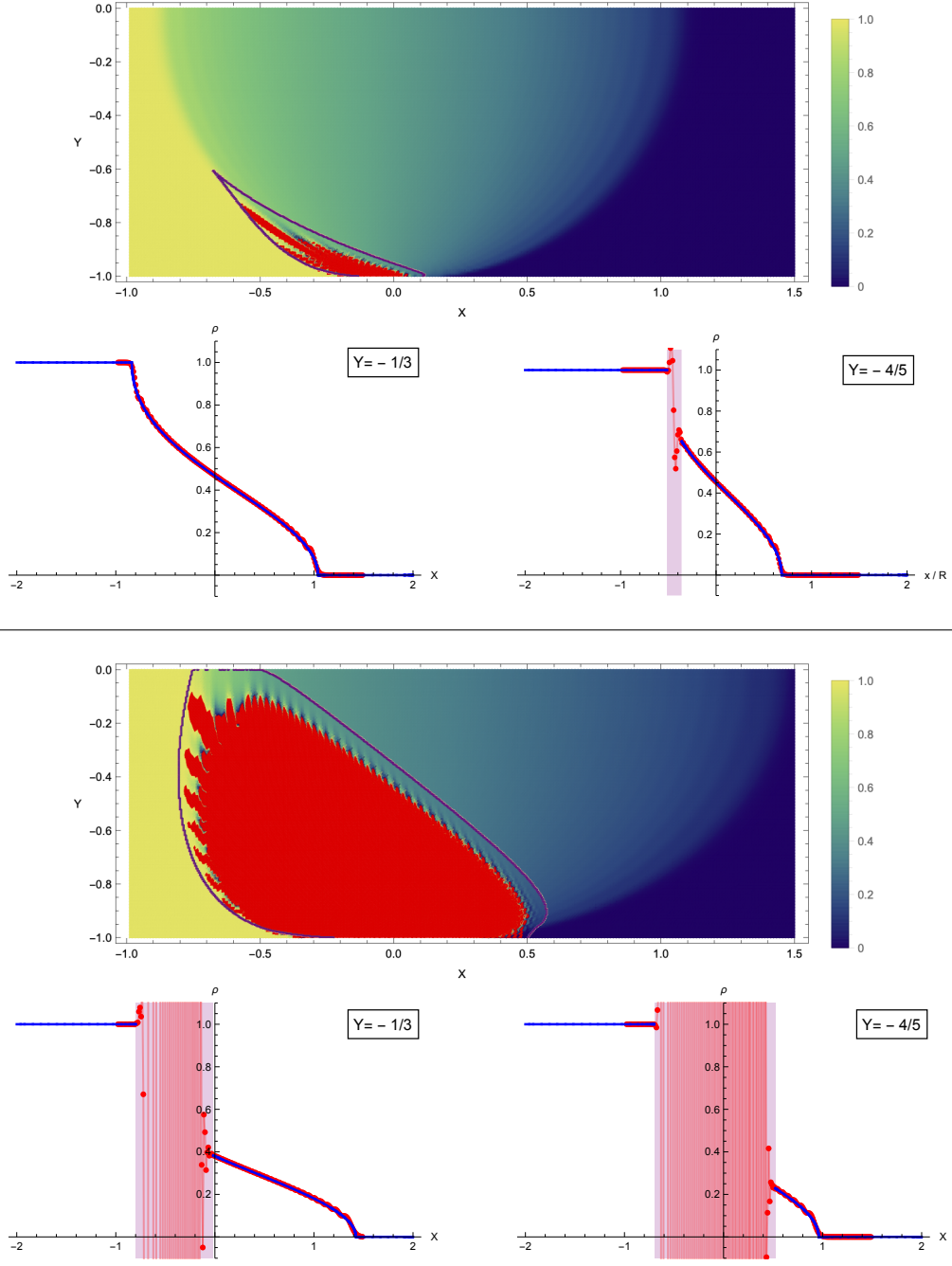


Figure 4.7: Comparison between the theoretical prediction for the density in the scaling limit and the density obtained numerically in finite size. The values of α are $1/20$ (top) and $1/4$ (bottom). The purple lines and the shaded purple regions represent the theoretical prediction for the regions where the density is ill-defined. The red regions represent the points whose simulated density is not between zero and one; we see that the red region does not perfectly coincide with the theoretical limit shape, but this is only a finite size effect (the matching gets better increasing R). The red points in the plots for fixed imaginary time represent the simulated density, while the blue lines represent its theoretical prediction.

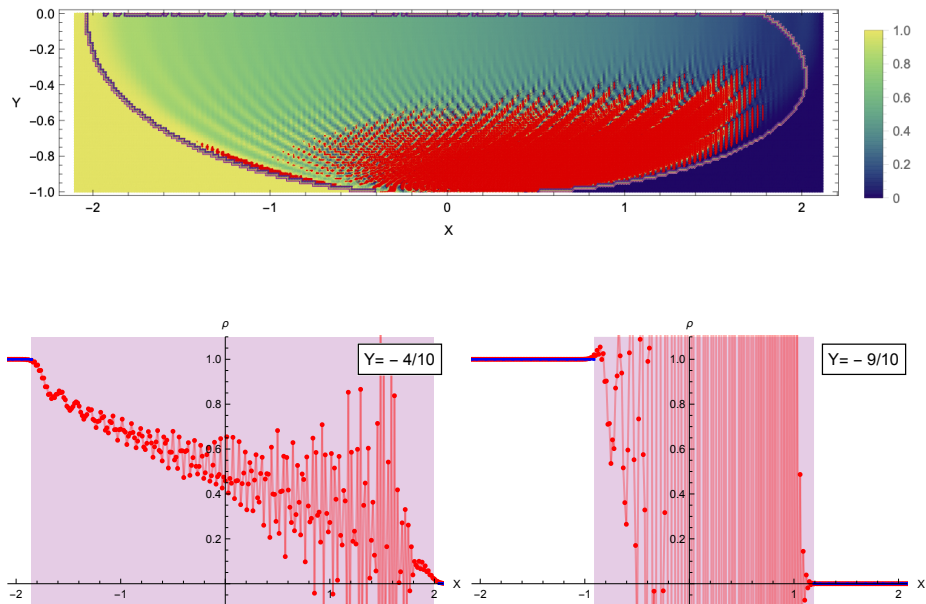


Figure 4.8: Comparison between the theoretical prediction for the density in the scaling limit and the density simulated in finite size for $\beta = 1/4$. The colour code is the same of Fig. 4.7. The error induced by finite size is bigger in this case because the density diverges more slowly in the scaling limit.

CHAPTER 4. THE DENSITY PROBLEM

Chapter 5

Alternative Geometries

5.1 Beyond domain wall geometry

So far, we always restricted ourselves to models in the domain wall geometry. In fact, when one wants to generate limit shapes imposing inhomogeneous boundary conditions, domain wall is the simplest geometry that can be considered. On the other hand, we showed in the previous chapter that, for NN hopping and NNN hopping in domain wall geometry, the quantity we identified as the density is not between zero and one everywhere. In Section 1.4, we argued that the possibility for the density not to be well defined arises from the non-trivial signs coming from fermions jumping over each other. This observation is consistent with the fact that regions of ill-defined density are contiguous to regions of well-defined density close to one.

A natural question arising from this observation is whether, choosing a geometry that induce a smaller total density, the density problem does not manifest, even considering both NN hopping and NNN hopping.

In this chapter we investigate our model of fermions (Section 1.4) in slightly more general geometries. Namely, we impose that the initial and final states refer both to a lattice configuration that is empty on the right and has constant density smaller than one on the left. In particular, we focus on having one particle every $p \in \mathbb{N} \setminus \{0\}$ sites, dubbing $|\psi_{1/p}\rangle$ the corresponding boundary states. Clearly, the case $p = 1$ gives back the domain wall geometry. We will refer to such geometries as *domain-wall-like* geometries. An illustration of the boundary states in domain-wall-like geometry is presented in Fig. 5.1.

To start with, we will generalize the exact formula for the two-point correlation function (3.43) to domain-wall-like geometries; as in Chapter 3, this derivation will hold for general dispersion relation. Then we will discuss the scaling limit for our specific dispersion relation and show that the density problem does not arise in these geometries.

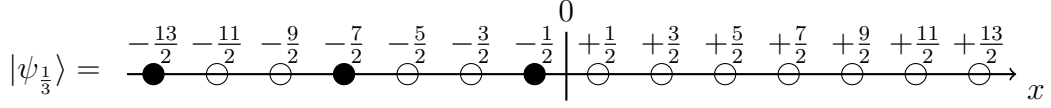


Figure 5.1: Representation of the boundary state in a domain-wall-like geometry in the case $p = 3$.

The computation that follows is similar in spirit to some typical computations where the problem of limit shapes in general boundary conditions is addressed, such as [60–63].

Before going on, notice that all the general observation we made in Section 1.4 about the symmetry of the model still hold, except for the particle-hole symmetry, since that one relied on having symmetric boundary states with respect to the particle-hole transformation. As a consequence, now the density for $\alpha < 0$ cannot be derived simply by the result for $\alpha > 0$. Nonetheless, for simplicity, we will consider only the case $\alpha > 0$.

5.2 Correlation function for domain-wall-like geometries

We start from the definition of the correlation function (1.16) adapted to the new geometry:

$$\langle \psi_{\frac{1}{p}} | c_x^\dagger(y) c_{x'}(y') | \psi_{\frac{1}{p}} \rangle_R \equiv \frac{\langle \psi_{\frac{1}{p}} | e^{-H(R-y)} c_x^\dagger e^{H(y'-y)} c_{x'} e^{-H(R+y')} | \psi_{\frac{1}{p}} \rangle}{\langle \psi_{\frac{1}{p}} | e^{-2HR} | \psi_{\frac{1}{p}} \rangle}, \quad (5.1)$$

where $|\psi_{\frac{1}{p}}\rangle$ is the state where the lattice is empty on the right of the origin and has a particle every p sites on the left, starting from the site $-1/2$ (see Fig. 5.1). With the notation introduced in Section 2.1,

$$|\psi_{\frac{1}{p}}\rangle \equiv \left(\prod_{m=0}^{+\infty} c_{-pm-\frac{1}{2}}^\dagger \right) |0\rangle. \quad (5.2)$$

We aim at finding an exact integral formula for this correlation function, following the same steps we did for the domain wall geometry. As we will see, some new features arise.

The first step is the application of Wick's theorem to express the correlation function as a product of semi-infinite matrices. Nothing essentially new appears at this level. The only thing worth noticing is that, as far as the size of the system is finite, one should take the length of the lattice $L = 2pl$, to end up with $l \times l$ matrices and l -components vectors. Without going again through the full derivation, we just

5.2. CORRELATION FUNCTION FOR DOMAIN-WALL-LIKE GEOMETRIES

report the result:

$$\langle \psi_{\frac{1}{p}} | c_x^\dagger(y) c_{x'}(y') | \psi_{\frac{1}{p}} \rangle_R = \sum_{m,n=0}^{+\infty} u_m T_{mn}^{-1} v_n, \quad (5.3)$$

where

$$\begin{aligned} u_m &= \langle 0 | c_{x'} c_{-pm-\frac{1}{2}}^\dagger(-(R+y')) | 0 \rangle, \\ v_n &= \langle 0 | c_{-pn-\frac{1}{2}} c_x^\dagger(-(R-y)) | 0 \rangle, \\ T_{mn} &= \langle 0 | c_{-pm-\frac{1}{2}} c_{-pn-\frac{1}{2}}^\dagger(-2R) | 0 \rangle. \end{aligned} \quad (5.4)$$

This expression generalizes (3.21) to domain-wall-like geometries.

Now, using the free fermions' property, one can show that

$$T_{mn} = \langle 0 | c_{-pm-\frac{1}{2}} c_{-pn-\frac{1}{2}}^\dagger(-2R) | 0 \rangle = \int_{-\pi}^{+\pi} \frac{dq}{2\pi} e^{-ipq(m-n)} e^{-2R\epsilon(q)}. \quad (5.5)$$

This means that T is still a Toeplitz matrix. However, at variance with the domain wall case, the symbol defining the matrix cannot be immediately read from the elements of T , because of the presence of the factor p . So, before being able to apply the semi-infinite Toeplitz matrices' properties, we have to properly identify the symbol related to the matrix T .

To tackle this problem, let us first introduce some notation. Following Chapter 3, let

$$[g_\tau]_m \equiv \int_{-\pi}^{+\pi} \frac{dq}{2\pi} e^{-ipq(m-n)} e^{-\tau\epsilon(q)}, \quad g_\tau(k) \equiv \sum_{l \in \mathbb{Z}} e^{ikl} [g_\tau]_l. \quad (5.6)$$

We also define the auxiliary function

$$h_\tau(q) \equiv e^{-\tau\epsilon(q)}, \quad (5.7)$$

so that we can look at $g_\tau(k)$ as a function constructed from $h_\tau(k)$ by keeping only one every p Fourier modes:

$$[g_\tau]_m = [h_\tau]_{pm}. \quad (5.8)$$

We can use the relation between the functions $g_\tau(k)$ and $h_\tau(k)$ to find the explicit expression of $g_\tau(k)$ we are looking for:

$$\begin{aligned} g_\tau(k) &= \sum_{n \in \mathbb{Z}} [h_\tau]_{pn} e^{-ikn} \\ &= \sum_{n \in \mathbb{Z}} \int_{-\pi}^{+\pi} \frac{dq}{2\pi} h_\tau(q) e^{iqpn} e^{-ikn} \\ &= \int_{-\pi}^{+\pi} dq h_\tau(q) \left(\sum_{m \in \mathbb{Z}} \delta(pq - k - 2\pi m) \right) \\ &= \frac{1}{p} \sum_{m \in \mathbb{Z}} \int_{-\pi}^{+\pi} dq h_\tau(q) \delta \left(q - \frac{1}{p}k - \frac{2\pi}{p}m \right), \end{aligned} \quad (5.9)$$

where we used the representation of the Dirac comb

$$\sum_{s \in \mathbb{Z}} \delta(k - 2\pi s) = \frac{1}{2\pi} \sum_{n \in \mathbb{Z}} e^{-ikn}. \quad (5.10)$$

Now, of the infinite number of terms in the sum we obtained, only few of them are different from zero, namely those for which the argument of the delta function has a zero in the integration interval, i.e. those for which $\frac{1}{p}k + \frac{2\pi}{p}m \in [-\pi, \pi]$; in other words, the m -th term is non-zero only if

$$k_- \leq k < k_+, \quad \text{with} \quad k_{\pm} \equiv \pi(-2m \pm p) \quad (5.11)$$

(notice that, since $p \geq 1$, we always have $k_+ > k_-$). On the other hand, we are interested only in $k \in [-\pi, +\pi]$, so, in order to have solutions, we need both conditions to hold. We can distinguish between three cases:

- the whole interval $[-\pi, \pi]$ is included in $[k_-, k_+]$, in which case

$$k_+ \geq \pi \wedge k_- \leq -\pi \iff -\frac{p-1}{2} \leq m \leq \frac{p-1}{2}; \quad (5.12)$$

- there are some values of $[-\pi, \pi]$ that are left out close to $-\pi$, in which case

$$-\pi < k_- < +\pi \iff -\frac{p}{2} - \frac{1}{2} < m < -\frac{p}{2} + \frac{1}{2}; \quad (5.13)$$

- there are some values of $[-\pi, \pi]$ that are left out close to $+\pi$, in which case

$$-\pi < k_+ < +\pi \iff +\frac{p}{2} - \frac{1}{2} < m < +\frac{p}{2} + \frac{1}{2}. \quad (5.14)$$

Notice that the case in which $[k_-, k_+]$ is strictly included in $[-\pi, \pi]$ cannot arise because $k_+ - k_- = 2\pi p \geq 2\pi$. Notice also that the second and third conditions have solutions only in the case p is even, with $m = -p/2$ and $m = +p/2$ respectively.

It is a bit inconvenient that, for even p , there are two values of m that contribute or not depending on the values of k , but this can be solved as described below. Given an even p , we consider the two allowed values of $m = \pm \frac{p}{2}$ together:

$$\int_{-\pi}^{+\pi} dq h_{\tau}(q) \left[\delta \left(q - \frac{1}{p}k + \pi \right) + \delta \left(q - \frac{1}{p}k - \pi \right) \right] = \begin{cases} h_{\tau} \left(\frac{1}{p}k - \pi \right), & k \in [0, +\pi) \\ h_{\tau} \left(\frac{1}{p}k + \pi \right), & k \in [-\pi, 0) \end{cases}. \quad (5.15)$$

Since $h_{\tau}(k + 2n\pi) = h_{\tau}(k), \forall k \in [-\pi, +\pi] \wedge \forall n \in \mathbb{Z}$, we see that we get the right result considering the m 's that satisfies either the first or the third condition only and without restrictions on k (beside $k \in [-\pi, +\pi]$). Summarizing,

$$g_{\tau}(k) = \frac{1}{p} \sum_m h_{\tau} \left(\frac{k}{p} + \frac{2\pi m}{p} \right), \quad (5.16)$$

5.2. CORRELATION FUNCTION FOR DOMAIN-WALL-LIKE GEOMETRIES

where the sum is over $m \in \mathbb{Z}$ such that

$$-\frac{p-1}{2} \leq m < \frac{p+1}{2}. \quad (5.17)$$

As a final step, to make the expression look nicer, we split the sum into two parts and we change variable in the first one as $m \rightarrow m + p$:

$$\begin{aligned} & \sum_{-\frac{p-1}{2} \leq m < \frac{p+1}{2}} h_\tau \left(\frac{k}{p} + \frac{2\pi m}{p} \right) \\ &= \sum_{-\frac{p-1}{2} \leq m \leq -1} h_\tau \left(\frac{k}{p} + \frac{2\pi m}{p} \right) + \sum_{0 \leq m < \frac{p+1}{2}} h_\tau \left(\frac{k}{p} + \frac{2\pi m}{p} \right) \\ &= \sum_{\frac{p+1}{2} \leq m \leq p-1} h_\tau \left(\frac{k}{p} - 2\pi + \frac{2\pi m}{p} \right) + \sum_{0 \leq m < \frac{p+1}{2}} h_\tau \left(\frac{k}{p} + \frac{2\pi m}{p} \right); \end{aligned} \quad (5.18)$$

using the periodicity of h_τ , gives

$$g_\tau(k) = \frac{1}{p} \sum_{m=0}^{p-1} h_\tau \left(\frac{k}{p} + \frac{2\pi m}{p} \right). \quad (5.19)$$

Now that we showed how to find the explicit expression of the symbol, let us put it aside for a moment and turn to the application of semi-infinite Toeplitz matrices' properties to compute T^{-1} .

The computation of T^{-1} starts analogously to the derivation we saw in Chapter 3: one assumes to be able to Wiener-Hopf decompose the symbol as $g_\tau(k) = g_\tau^-(k)g_\tau^+(k)$, where the negative Fourier modes of g_τ^+ and the positive Fourier modes of g_τ^- are all zero, and uses eq. (2.32) to compute the inverse as

$$(T^{-1})_{mn} = \sum_{r=0}^{\infty} [(g_{2R}^+)^{-1}]_{m-r} [(g_{2R}^-)^{-1}]_{-n+r}. \quad (5.20)$$

This expression can be processed along the lines of Chapter 3, to be rewritten as an integral. However, there is something new that must be remarked. Since, due to the free fermions' properties, we have

$$\langle 0 | c_m c_n^\dagger(-\tau) | 0 \rangle = \int_{-\pi}^{+\pi} \frac{dq}{2\pi} e^{iq(m-n)} e^{-\tau\epsilon(q)}, \quad (5.21)$$

we would like to claim that this time

$$u_m = [g_{R+y'}]_{-m-(x'+\frac{1}{2})/p} \quad \text{and} \quad v_n = [g_{R-y}]_{n+(x+\frac{1}{2})/p}, \quad (5.22)$$

rather than being

$$u_m = [g_{R+y'}]_{-m-(x'+\frac{1}{2})} \quad \text{and} \quad v_n = [g_{R-y}]_{n+x+\frac{1}{2}} \quad (5.23)$$

as in the previous case. But it is not true in general: while the j -th Fourier coefficient of g_τ is indeed the pj -th Fourier coefficient of h_τ , it is not true that the j -th Fourier coefficient of h_τ is the “ j/p -th Fourier coefficient” of g_τ if j/p is not an integer (the very same notion of “ j/p -th Fourier coefficient” is not well defined in general). For this reason we will proceed assuming that $x + \frac{1}{2}$ and $x' + \frac{1}{2}$ are multiples of p . This will not affect the search for the limit shapes, since in the scaling limit we are not interested in the microscopic (i.e. site by site) variation of the density, but we look only to the coarse-grained density ϱ , that is assumed to be continuous.

In the end, the result of Chapter 3 is modified in two important ways: first of all, the positions x and x' are divided by p ; secondly, the recombination of the terms related to the geometric sum is not as nice as it was, since

$$\begin{aligned} e^{\frac{1}{2p}i(q-k)} \sum_{r=0}^{+\infty} e^{ir(q-k)} &= e^{\frac{1}{2p}i(q-k)} \sum_{r=0}^{+\infty} e^{ir(q-k+i0^+)} \\ &= e^{\frac{1}{2p}i(q-k)} \frac{1}{1 - e^{i(q-k+i0)}} \\ &= e^{-\frac{p-1}{2p}i(q-k)} \frac{1}{2i \sin(\frac{k-q}{2} - i0)}. \end{aligned} \quad (5.24)$$

Finally, we have

$$\boxed{\langle \psi_{\frac{1}{p}} | c_x^\dagger(y) c_{x'}(y') | \psi_{\frac{1}{p}} \rangle_R = \int_{-\pi}^{+\pi} \frac{dk dq}{(2\pi)^2} \frac{e^{-ik\frac{x}{p} + iq\frac{x'}{p}} e^{-\frac{p-1}{2p}i(q-k)}}{2i \sin(\frac{k-q}{2} - i0)} \frac{g_{R+y'}(q) g_{R-y}(k)}{g_{2R}^+(q) g_{2R}^-(k)}}, \quad (5.25)$$

valid for all $x + 1/2$ and $x' + 1/2$ that are multiples of p .

This result is exact and holds for any dispersion relation, but its application is based on the knowledge of the Wiener-Hopf decomposition of the symbol $g_\tau(k)$, which, as we have already mentioned, can be far from trivial. In Chapter 3 we managed to compute it thanks to the simplifications caused by the symbol $g_\tau(k)$ being an exponential with the imaginary time factorized at the exponent; this made the symbols in (5.25) combine in a nice way. Now the symbol is not one single exponential with the imaginary time factorized at the exponent but a linear combination of such exponentials. This is the greatest and essential difference with the domain wall case. We cannot get further simplification in the correlation function at this stage and to go on we have to consider the scaling limit and specify something more about the dispersion relation.

5.3 Scaling limit in domain-wall-like geometries

5.3.1 General treatment

Let us consider the scaling limit $R, x, y, x', y' \rightarrow +\infty$ with fixed $x/R, x'/R, y/R, y'/R$. The first thing we look at to simplify the correlation function (5.25) is which is the dominant contribution in the symbol $g_\tau(k)$ expressed by (5.19). To make any progress, we have to be more specific about the type of dispersion relation of the model.

The hypothesis we assume is the following:

$$\epsilon(k/p) < \epsilon(q/p), \quad \forall k \in \left(-\frac{\pi}{p}, \frac{\pi}{p}\right) \quad \wedge \quad \forall q \in [-\pi, \pi) \setminus \left(-\frac{\pi}{p}, \frac{\pi}{p}\right). \quad (5.26)$$

Notice that the dispersion relation we are interested in $\epsilon(k) = -\cos(k) - \alpha \cos(2k)$ satisfies the requirement $\forall \alpha \geq 0$. With this assumption, it is clear that, of all the terms involved in the sum (5.19) for $g_\tau(k)$, the one that dominates is the first, i.e. the one with $m = 0$, since it has the exponent bigger or equal to the exponent of any other term $\forall k \in (-\pi, +\pi)$. Hence, for g_τ in the double integral (5.25), we have

$$\lim_{\tau \rightarrow +\infty} g_\tau(k) = \frac{h_\tau(k/p)}{p}. \quad (5.27)$$

As for the Wiener-Hopf decomposition, notice that

$$g_\tau^-(k)g_\tau^+(k) = \frac{h_\tau^-(k/p)h_\tau^+(k/p)}{p} \implies g_\tau^\pm(k) = \frac{h_\tau^\pm(k/p)}{\sqrt{p}}, \quad (5.28)$$

so that

$$\langle \psi_{\frac{1}{p}} | c_x^\dagger(y) c_{x'}(y') | \psi_{\frac{1}{p}} \rangle_R = \frac{1}{p} \int_{-\pi}^{+\pi} \frac{dk dq}{(2\pi)^2} \frac{e^{-ik\frac{x}{p} + iq\frac{x'}{p} - \frac{p-1}{2p}i(q-k)}}{2i \sin(\frac{k-q}{2} - i0)} \frac{h_{R+y'}(q/p)h_{R-y}(k/p)}{h_{2R}^+(q/p)h_{2R}^-(k/p)}. \quad (5.29)$$

Now, since $h_\tau(k)$ is as a single exponent with the imaginary time factorized at the exponent, we can use the same procedure as in Chapter 3 to simplify the correlation function. Introducing

$$\xi(k) = \epsilon(k/p) \quad \text{and} \quad \phi(k) = e^{-\xi(k)}, \quad (5.30)$$

the situation is not different from the one we already encountered, with the only differences being:

- an overall factor $1/p$;
- x/p and x'/p instead of x and x' ;

- $\xi(k)$ instead of $\epsilon(k)$.

The final expression of the correlation function in the scaling limit is then

$$\boxed{\langle \psi_{\frac{1}{p}} | c_x^\dagger(y) c_{x'}(y') | \psi_{\frac{1}{p}} \rangle_R = \frac{1}{p} \int_{-\pi}^{+\pi} \frac{dk dq}{(2\pi)^2} \frac{e^{-ik\frac{x}{p} + iq\frac{x'}{p} + y\xi(k) - y'\xi(q) + iR(\tilde{\xi}(q) - \tilde{\xi}(k))}}{2i \sin(\frac{k-q}{2} - i0)} e^{-\frac{p-1}{2p}i(q-k)}}, \quad (5.31)$$

where $\tilde{\xi}(k)$ is the Hilbert transform of $\xi(k)$. As above, $x + 1/2$ and $x' + 1/2$ have to be multiples of p , but, as already noticed, this still allows to find the full density profile in the scaling limit, under the assumption it is continuous.

The Hilbert transform $\tilde{\xi}(k)$ is computed via (3.46), i.e. finding first its Fourier decomposition in the interval $[-\pi, \pi]$ and then substituting $\cos \rightarrow \sin$, $\sin \rightarrow -\cos$, leaving aside the constant term:

$$\begin{aligned} \xi(k) &= [\xi]_0 + \sum_{n=1}^{+\infty} \left[\cos\left(\frac{2\pi}{T}nk\right) ([\xi]_n + [\xi]_{-n}) + i \sin\left(\frac{2\pi}{T}nk\right) ([\xi]_n - [\xi]_{-n}) \right] \\ \Rightarrow \tilde{\xi}(k) &= \sum_{n=1}^{+\infty} \left[\sin\left(\frac{2\pi}{T}nk\right) ([\xi]_n + [\xi]_{-n}) - i \cos\left(\frac{2\pi}{T}nk\right) ([\xi]_n - [\xi]_{-n}) \right], \end{aligned} \quad (5.32)$$

where

$$\xi_n \equiv \int_{-\pi}^{+\pi} \frac{dk}{2\pi} e^{-ink} \xi(k). \quad (5.33)$$

Notice that, in general, the function $\xi(k)$ is not periodic with period equal to 2π as $\epsilon(k)$ was. It still can be written as a Fourier series in $k \in [-\pi, +\pi]$, being integrable in that interval, but the Fourier series will coincide with $\xi(k)$ on that interval only.¹ Notice also that $\cos(k/p)$ is not trivially transformed into $\sin(k/p)$ for $p \geq 2 \in \mathbb{Z}$, since the Fourier decomposition of $\cos(k/p)$ is not simply $\cos(k/p)$ itself; the same holds for $\sin(k/p)$. We are going to tackle the problem of computing the Hilbert transform in the next section.

5.3.2 Specialization to our dispersion relation

Let us now specialize to the particular case in which the dispersion relation is

$$\epsilon(k) = -\cos(k) - \alpha \cos(2k). \quad (5.34)$$

As already noticed, this dispersion relation satisfies the condition (5.26) under which eq. (5.25) was derived, so we can use (5.25) to compute the correlation function.

¹To be precise, in fact, since the original function gives the same in each period, ξ is still given by the repetition of the interval $[-\pi, \pi]$, so it is still periodic, but it is not differentiable at the boundaries. However, since we are interested in one period only, this observation will not affect our discussion.

5.3. SCALING LIMIT IN DOMAIN-WALL-LIKE GEOMETRIES

Having the explicit dispersion relation allows to compute exactly $\xi(k)$ and its Hilbert transform. Trivially,

$$\xi(k) = \epsilon(k/p) = -\cos(k/p) - \alpha \cos(2k/p). \quad (5.35)$$

Then, the Hilbert transform can be computed:

$$\tilde{\xi}(k) = \begin{cases} -\sin(k) - \alpha \sin(2k) & , p = 1 \\ -\frac{2}{\pi} \operatorname{arctanh}(\sin(k/2)) \cos(k/2) - \alpha \sin(k) & , p = 2 \\ -\frac{p}{\pi} \int_0^{+\infty} dx \frac{\sin(\frac{x}{p}) \sin(k) \sinh(x)}{\cosh(px) + \cos(k)} - \alpha \frac{p}{2\pi} \int_0^{+\infty} dx \frac{\sin(\frac{2x}{p}) \sin(k) \sinh(x)}{\cosh(\frac{p}{2}x) + \cos(k)} & , p > 2 \end{cases}; \quad (5.36)$$

the calculation is reported in Appendix B.

The remaining asymptotic analysis proceeds as in the previous case: we are interested in the limit shapes of the density profile in the scaling limit and to obtain them we will study the asymptotic behaviour of the correlation function (5.31) at equal times and equal positions.

5.3.3 Density profile for half-filled domain wall geometry

We specialize to the domain-wall-like geometry with $p = 2$. As in Chapter 4, we define the complex variables

$$z = e^{ik} \quad \text{and} \quad w = e^{i(q+i0)} \quad (5.37)$$

and the coarse grained density

$$\varrho(X, Y) \equiv \lim_{R \rightarrow +\infty} \rho(XR, YR) = \lim_{R \rightarrow +\infty} \langle \psi_1 | c_{XR}^\dagger(YR) c_{XR}(YR) | \psi_1 \rangle_R. \quad (5.38)$$

Then we proceed with the evaluation of ϱ using the representation of the two-point function (5.31), from which:

$$\varrho(X, Y) = \lim_{R \rightarrow +\infty} \frac{1}{2} \int_{C_z} \frac{dz}{2\pi i \sqrt{z}} \int_{C_w} \frac{dw}{2\pi i \sqrt{w}} \frac{e^{R(f_\alpha(w, X, Y) - f_\alpha(z, X, Y))}}{z - w} z^{\frac{1}{4}} w^{-\frac{1}{4}}, \quad (5.39)$$

where, as in domain wall geometry, C_z is the unitary circumference around the origin and C_w is a circumference around the origin with radius smaller than one. Here the exponent is defined as

$$f_\alpha(z, X, Y) \equiv \frac{X}{2} \ln z - 2 \arctan(z^{1/2}) \frac{z+1}{\pi \sqrt{z}} + \frac{z+1}{2\sqrt{z}} (1+Y) - \frac{\alpha}{2z} (z^2 - 1 - Y(z^2 + 1)), \quad (5.40)$$

and it is obtained from (5.35) and (5.36) and using

$$\begin{aligned}
 -\operatorname{arctanh}(\sin(k/2)) \cos(k/2) &= i \arctan\left(\frac{z-1}{2\sqrt{z}}\right) \frac{z+1}{2\sqrt{z}} \\
 &= i(\arctan(z^{1/2}) - \arctan(z^{-1/2})) \frac{z+1}{2\sqrt{z}} \\
 &= i(2\arctan(z^{1/2}) - \pi/2) \frac{z+1}{2\sqrt{z}}.
 \end{aligned} \tag{5.41}$$

The saddle-point equation in this case is

$$\begin{aligned}
 \pi\sqrt{z}(2x\sqrt{z} + y(z-1) + z-1) + 2\pi\alpha((y-1)z^2 - y-1) + \\
 - 4z - 4(z-1)\sqrt{z}\tan^{-1}(\sqrt{z}) = 0.
 \end{aligned} \tag{5.42}$$

Differently from the domain wall case, this equation does not have explicit solution. Nonetheless, the solutions can be approximated numerically and we find them to have the following characteristics:

- There are two solutions for any value of X and Y .
- For each $Y = Y_0$, there is a $X = X_0$ such that the two saddle points are real and positive $\forall X \geq X_0$ and complex conjugated $\forall X < X_0$.
- For any $Y = Y_0$ and $X \rightarrow -\infty$ the real part of the two complex conjugated saddle points is negative and their imaginary part goes to zero.

Some examples of the configuration of the saddle points are presented in Fig. 5.2.

We observe that the essential behaviour of the saddle points is the same as for $\alpha = 0$ in domain wall geometry, if one considers just Regime I and Regime II (compare Fig. 5.2 with Fig. 4.1a and Fig. 4.1b). Also, notice that the pole in $z = w$ plays the same role as in that case. Since the asymptotic study for $\alpha = 0$ in domain wall geometry did not rely on the explicit expression of the saddle points as much as on their *topological* configuration, the same arguments hold here. As a result, $\varrho = 0$ for those values of X, Y that have real saddle points and $0 < \varrho < 1/2$ for all the other point, approaching asymptotically the value of $1/2$ for $X \rightarrow -\infty$ (the residue contribution still gives a value between zero and one, but this time we have an overall factor of $1/2$ in front of the density (5.39)).

We emphasize that, for $p = 2$, the density profile in the scaling limit is well defined everywhere, even for the model H_α . The density profile in this case is represented in Fig. 5.3.

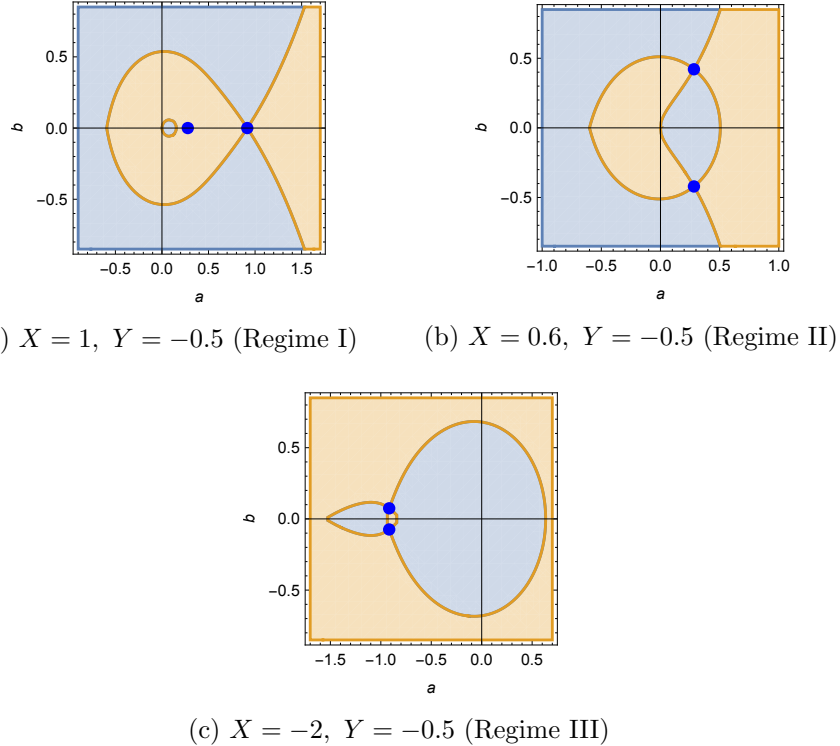
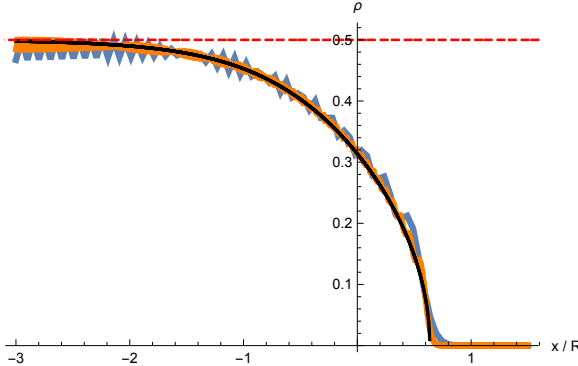
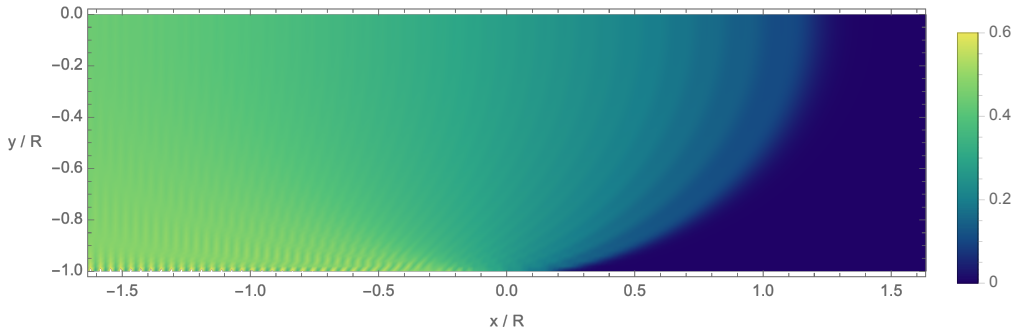


Figure 5.2: Plots of $u(a, b) \equiv \text{Re}[f_0(a + ib, X, Y)]$ for various values of X, Y and $\alpha = 0.2$. The blue (resp. orange) region represents the region of the plane a, b for which $u(a, b) > u(a_0, b_0)$ (resp. $u(a, b) < u(a_0, b_0)$), where (a_0, b_0) is one of the saddle points. The blue points represent the location of all the two saddle points. For each value of $Y = Y_0$, there is a value $X = X_0$ such that the two saddle points are real $\forall(X, Y_0)$ with $X \geq X_0$ and are complex conjugated $\forall(X, Y_0)$ with $X < X_0$. For $X \rightarrow -\infty$, the imaginary part of the saddle points for (X, Y) goes to zero.



- (a) Density profile for $\alpha = 0$ and $y = 0$. The black line is the theoretical prediction, obtained from the saddle-point treatment, solving numerically the transcendental equation for the saddle points and then computing the simple integral coming from the residue contribution (this integral is still simple as in domain wall geometry because the two phases cancel each other, precisely as we saw in Chapter 4). The blue and the orange lines are simulation for the density in finite size, obtained as explained in Section 3.4: the blue one is related to $R = 20$ and the orange one is related to $R = 68$. One can see that the oscillations around the theoretical prediction get smaller. The same computation could be done for any values of α and y .



- (b) Simulated density profile for $\alpha = 1/3$ in finite size. It shows all the characteristics we expected. In particular, the density is always well defined.

Figure 5.3: Density profile in the half-filled domain wall geometry.

5.3.4 Other geometries and hoppings

It is not difficult to extend our argument to geometries with $p \geq 3$. The saddle-point equation is even more complicated, but one can numerically show that the behaviour of the saddle points is the same as in the first two regimes of the $\alpha = 0$ case. This leads to very similar predictions for the density: zero where the two saddle points are real, $1/p$ far to the left and between 0 and $1/p$ where the two solutions are complex conjugated. So, $\forall p \geq 2$, the density in the scaling limit is well defined everywhere, even considering the full Hamiltonian H_α .

Let us now consider e.g. the case where the Hamiltonian contains a fourth-neighbours hopping term rather than the NNN hopping; the dispersion relation of the model is

$$\epsilon(k) = -\cos(k) - \alpha \cos(4k). \quad (5.43)$$

Since

$$\epsilon(k/p) > \epsilon(k/p + 2\pi j/p) \quad \forall k \in (-\pi, \pi), \forall j \in \{1, \dots, p-1\}, \quad (5.44)$$

the asymptotic analysis can be performed as above. In this case we have

$$\xi(k) = -\cos(k/p) - \alpha \cos(4k/p) \quad (5.45)$$

and

$$\tilde{\xi}(k) = \begin{cases} -\sin(k) - \alpha \sin(4k), & p = 1 \\ -\frac{p}{\pi} \int_0^{+\infty} dx \frac{\sin(\frac{\pi}{p}) \sin(k) \sinh(x)}{\cosh(px) + \cos(k)} - \alpha \sin\left(\frac{4}{p}k\right), & p \in \{2, 4\} \\ -\frac{p}{\pi} \int_0^{+\infty} dx \frac{\sin(\frac{\pi}{p}) \sin(k) \sinh(x)}{\cosh(px) + \cos(k)} - \alpha \frac{p}{4\pi} \int_0^{+\infty} dx \frac{\sin(\frac{4}{p}\pi) \sin(k) \sinh(x)}{\cosh(\frac{p}{4}x) + \cos(k)}, & p > 4 \text{ (even)} \end{cases}. \quad (5.46)$$

For odd p we have the complication that (5.44) does not hold for all k , so the approximation

$$g(k) \sim h(k/p) \quad (5.47)$$

must be revised and $g(k)$ has to be defined piecewise. Anyway, any portion of $g(k)$ is still an exponential with the imaginary time factorized at the exponent, so the argument is still valid. The phenomenology is essentially the same.

Let us focus the case of even p . The case $p = 4$ is analogous to the case of our model with NNN hopping in $p = 2$, since

$$\xi(k) = -\cos(k/4) - \alpha \cos(k). \quad (5.48)$$

Analogous considerations hold for all even p bigger than 4. But consider now $p = 2$. Here $\cos(2k)$ and $\sin(2k)$ are involved in the computation and they play a role

similar to the one they played in domain wall geometry for the initial dispersion relation, leading to two additional solutions for the saddle-point equation (it can be shown numerically). The richness in the saddle points' panorama leads again to the impossibility close the integration contours as we want in the complex plane, and finally to the divergence of the density $\varrho(X, Y)$ for some values of X and Y (the density profile is presented in Fig. 5.4).

In conclusion, given a Hamiltonian with a NN hopping and another arbitrary hopping we see that, increasing p , the number of solutions of the saddle-point equation decreases, until only two solutions are left, thus leading to a well-defined density.

5.4 Generalization of the domain-wall-like geometry

So far, we considered geometries where the boundary states are chosen such that the right half of the lattice is empty and the left part is filled with one particle every p sites. This can be generalized to the case where we consider s particles every p site (clearly, $s < p$, with $s, p \in \mathbb{N}$). Connecting with the discussion of the previous section, we expect this choice of geometry to yield an asymptotic density s/p for $x \rightarrow -\infty$. So this allows, in principle, to tune the asymptotic density to any rational value and, since rationals are dense in reals, close to any real value between zero and one. We call such geometries *general domain-wall-like* and their corresponding boundary states $|\psi_{\frac{s}{p}}\rangle$. In this section we will sketch for completeness how one should adapt our arguments to treat this kind of geometries.

Let us consider the semi-infinite succession of s fermions followed by $p - s$ holes on the left half of the lattice, as represented in Fig. 5.5. The occupied sites can be represented by the introduction of the function

$$S_{ps}(n) \equiv \frac{p}{s} (n - n \bmod s) + n \bmod s, \quad (5.49)$$

so that $-S_{ps}(n) - \frac{1}{2}$, with n running over all the non-negative integers, gives all the occupied sites. Since our interest will still be in the scaling limit, the particular sequence with which we put s fermions every p sites does not affect the final result. As always, we look at the two point correlation function.

The application of Wick's theorem is done without any problem. In the finite-size intermediate passages, we just take the length of the lattice to be pl . We end up with the usual expression of the correlation function as a product of semi-infinite

5.4. GENERALIZATION OF THE DOMAIN-WALL-LIKE GEOMETRY

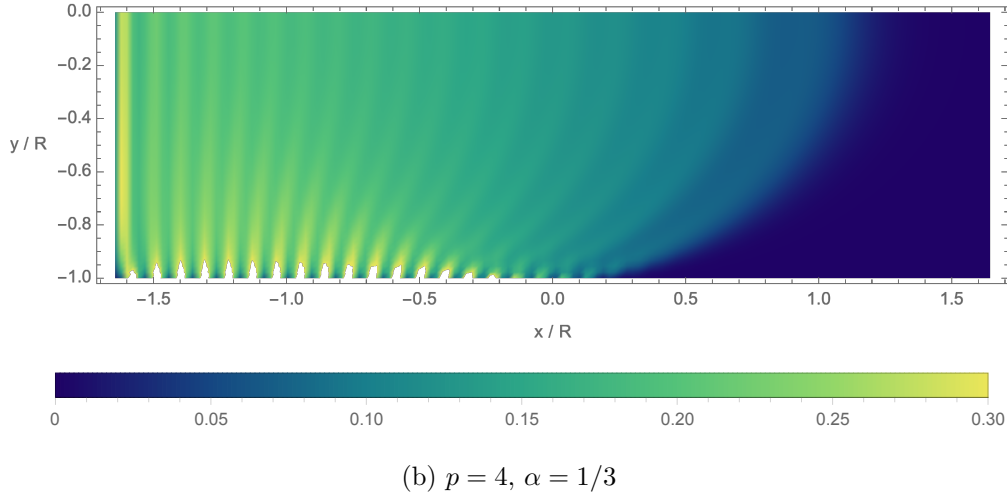
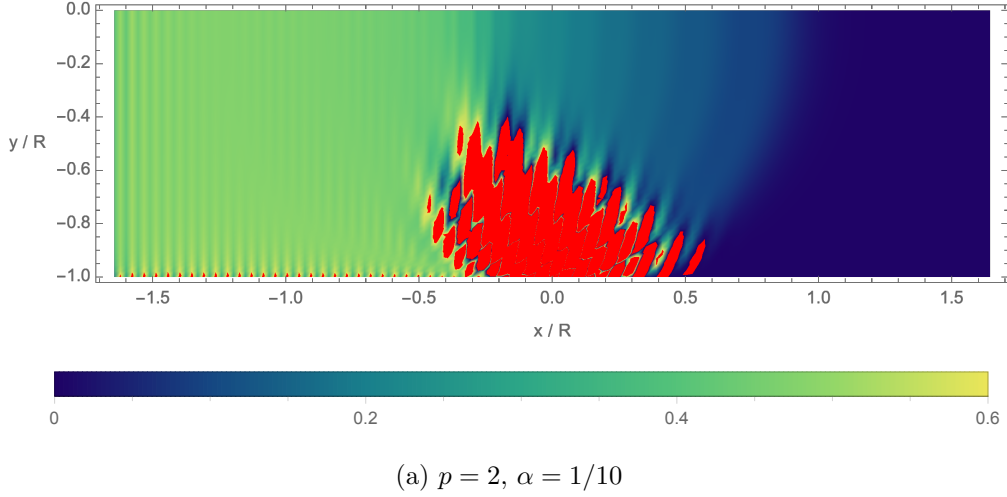


Figure 5.4: Density profile for a model with dispersion relation $\epsilon(k) = -\cos(k) - \alpha \cos(4k)$ in two different domain-wall-like geometries. This is an illustration of the fact that, increasing p , the number of solutions in the saddle-point equation diminishes, leading eventually to the disappearance of the regions where the density is ill-defined.

$$|\psi_{\frac{2}{3}}\rangle = \left| -\frac{13}{2}, -\frac{11}{2}, -\frac{9}{2}, -\frac{7}{2}, -\frac{5}{2}, -\frac{3}{2}, -\frac{1}{2} \right|^0 \left| +\frac{1}{2}, +\frac{3}{2}, +\frac{5}{2}, +\frac{7}{2}, +\frac{9}{2}, +\frac{11}{2}, +\frac{13}{2} \right\rangle_x$$

Figure 5.5: Representation of the boundary state in a general domain-wall-like geometry in the case $p = 3, s = 2$.

matrices:

$$\begin{aligned} \langle \psi_{\frac{s}{p}} | c_x^\dagger(y) c_{x'}(y') | \psi_{\frac{s}{p}} \rangle_R &= \sum_{m,n=0}^{+\infty} u_m T_{mn}^{-1} v_n, \\ \begin{cases} u_m = \langle 0 | c_{x'} c_{-S_{ps}(m)-\frac{1}{2}}^\dagger(-(R+y')) | 0 \rangle \\ v_n = \langle 0 | c_{-S_{ps}(n)-\frac{1}{2}} c_x^\dagger(-(R-y)) | 0 \rangle \\ T_{mn} = \langle 0 | c_{-S_{ps}(m)-\frac{1}{2}} c_{-S_{ps}(n)-\frac{1}{2}}^\dagger(-2R) | 0 \rangle \end{cases}. \end{aligned} \quad (5.50)$$

At this point we usually apply semi-infinite Toeplitz matrices' properties to compute the inverse of T . But here comes the essential complication: T is not Toeplitz anymore. As a matter of fact,

$$T_{mn} = \langle 0 | c_{-S_{ps}(m)-\frac{1}{2}} c_{-S_{ps}(n)-\frac{1}{2}}^\dagger(-2R) | 0 \rangle = \int_{-\pi}^{+\pi} \frac{dq}{2\pi} e^{-iq(S_{ps}(m)-S_{ps}(n))} e^{-2R\epsilon(q)}, \quad (5.51)$$

where $S_{ps}(m) - S_{ps}(n) \neq S_{ps}(m-n)$, because of the presence of the 'mod' function.

Nonetheless, T still has a certain structure: it is block-Toeplitz. Indeed let us decompose T in blocks of dimension $s \times s$ and identify the block whose top left element is $T_{As Bs}$ with T_{AB} :

$$T = \begin{pmatrix} T_{00} & T_{01} & \dots \\ T_{10} & T_{11} & \dots \\ \dots & \dots & \dots \end{pmatrix}, \quad T_{As+m, sB+n} = (T_{AB})_{m,n} \quad \forall m, n \in \{0, \dots, s-1\}. \quad (5.52)$$

The elements of one generic block are

$$(T_{AB})_{mn} = \langle 0 | c_{-pA-m-\frac{1}{2}} c_{-pB-n-\frac{1}{2}}^\dagger(-2R) | 0 \rangle = \int_{-\pi}^{+\pi} \frac{dq}{2\pi} e^{-iq(p(A-B))} e^{-iq(m-n)} e^{-2R\epsilon(q)}, \quad (5.53)$$

which tells us that each block is a Toeplitz matrix (this time it is finite) and that the dependence of the block-indices is

$$T_{AB} = [G]_{A-B}, \quad (5.54)$$

where $[G]$ is some matrix function. Similarly to what we did with semi-infinite Toeplitz matrices, we can construct the symbol defining the semi-infinite block-Toeplitz matrix T as

$$G(k) = \sum_{A \in \mathbb{Z}} e^{ikl} [G]_A. \quad (5.55)$$

The difference with the previous case is that the symbol is now a matrix.

There are tools to treat this kind of matrix that have been used to approach similar problems, see e.g. [63]. Even though the mathematical treatment is more complicated, we expect that the final result will have an analogous expression to the ones we saw so far. Such conjecture is strongly supported by numerics.

5.4. GENERALIZATION OF THE DOMAIN-WALL-LIKE GEOMETRY

Let us conclude mentioning that a possible way to circumvent the computation with block-Toeplitz matrices could be using the insight we gained from our previous treatment for geometries with $s = 1$ to construct an ansatz to plug in alternative methods to find the density. To give an example, a possible alternative method is the hydrodynamic approach, based on [64]; see for instance [28]. We will not delve here into this possibility, but we mention it as a possible direction for future work.

Chapter 6

Final Remarks and Conclusion

Let us summarize what has been done. We started with a certain model of fermionic particles on a one dimensional lattice that can hop to nearest-neighbour and next-nearest-neighbour sites. We considered its imaginary-time evolution in the so-called domain wall geometry, which consists in taking the lattice in the initial and final states completely empty on the right and fully occupied on the left of the origin.

We focused on the two-point correlation function of the model, whose definition was inspired by a mapping between a dimer model and a fermionic model. In particular, our interest was mainly in the density and its limit shapes. After having introduced the main tools to be used during the computation, we worked out an exact integral formula for the correlation function of our model, providing an alternative derivation for a known result. Such integral formula was then used to characterize the limit shapes for the density profile. In particular, we observed that, when the nearest-neighbour and the next-nearest-neighbour hoppings are both present, there are values of position and imaginary time for which the density is not between zero and one, but is singular. A prescription to find the exact limit shapes was given.

Starting from the observation that the density is well defined everywhere in the absence of the next-nearest-neighbours hopping, we gave an argument according to which the ill-definition of the density originates from the non-trivial minus signs introduced in the expectation value of the density by fermions jumping over each other. As a by-product, this implies that geometries with a higher total fermion density are more susceptible to exhibit an ill-defined density. To investigate such statement, we considered what we called *domain-wall-like* geometries, where the lattice in the initial and final states is empty on the right and has one fermion every p sites on the left. As a first step, we found an exact integral formula for the correlation function. Because of some complications due to the geometry, the integral formula is explicit only in the scaling limit. After that, we characterized

CHAPTER 6. FINAL REMARKS AND CONCLUSION

the limit shapes of the density profile and found that the density is well defined everywhere in space and imaginary time (at least in the scaling limit), consistently with our observation that lower densities are less problematic. This showed that our dispersion relation, even though not defining a totally positive model, allows for some boundary conditions that, at least in the scaling limit, enhance the probabilistic interpretation. Beside understanding the sign and divergence problem of the density, some new results concerning limit shapes were found throughout our work.

We concluded our discussion noticing how the whole argument could be generalized to other types of hoppings, highlighting that the conclusion is the same: reducing the total density reduces the number of solutions in the saddle-point equation for the asymptotic study, until there are only two of them, thus leading to a well-defined density.

The interest in non-positive models is not new to physics. For instance, a similar situation is often encountered when simulating quantum systems, using Monte Carlo methods, e.g. [65, 66]: to simulate (quantum) fermionic systems one basically uses the quantum-statistical mechanics correspondence and may end up with a statistical mechanics model where the Boltzmann weights are not all non-negative; this is often dubbed “sign problem”, as the lack of positivity of the statistical mechanical interpretations makes numerical simulations extremely slow to converge. Statistical models with non positive weights are also interesting in their own rights, in particular they may appear when trying to reformulate a non-local but positive model as a local one, e.g. [67].

Some open questions remain, like the extension of our argument to what we called *general domain-wall-like* geometries, i.e. geometries where the lattice in the boundary states is empty on the right and is populated with an arbitrary constant density on the left. We mentioned that numeric simulations show similar phenomenology to the previous case and the problem could be tackled by alternative methods, such as hydrodynamics.

Another possible development could be to include interactions in the model. Essentially, the transfer matrix formalism allows to see all the models exhibiting the limit shape phenomenon as quantum systems evolving in imaginary time. The majority of solved models maps to free fermions, but there is interest in the interacting case. Needless to say, interactions makes everything much harder, but some results are available. For recent developments see [68–72] and references therein. One of the complications is that Wick’s theorem cannot be used as simply; however, we strongly suspect that, considering interactions in our model, the phenomenology would stay the same, though it would be much harder to describe the arctic curves analitically.

Finally, fluctuations have been excluded from our treatment, but they are actually there, on top of the density profile we described. Even specializing to the axis

$y = 0$, where we know our model always allows for a statistical interpretation, the study of the fluctuations is a point of interest in mathematical literature. For $\alpha = 0$, the interfaces are known to follow the Tracy-Widom distribution [73] and it can be shown to be the case also for almost all values of α [28]. On the other hand, when $\alpha = \alpha_c$ the fluctuations appear to decay slower with distance than the Tracy-Widom distribution. This aspect requires a deeper understanding and possibly an analytic description.

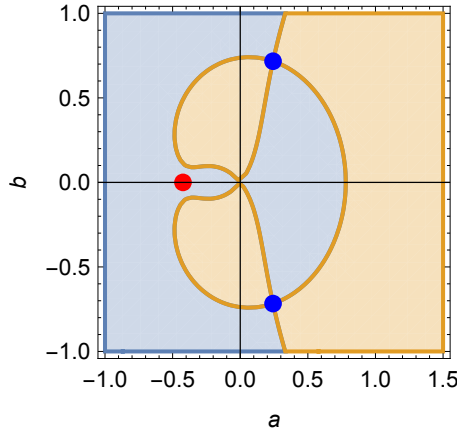
CHAPTER 6. FINAL REMARKS AND CONCLUSION

Appendix A

Saddle-Point Method for the Density

In this appendix, we evaluate the asymptotic behaviour of the density (4.6) in the scaling limit via the saddle-point method.

We will focus on the case $\alpha > 0$ in which the values of X and Y in the expression of the density are such that the saddle-points configuration is qualitatively similar to the one represented in Fig. 4.5b (in the language of Chapter 4, we consider those values X, Y in Regime II for which the deformation described in that chapter is not possible). Both the density formula and the figure are reported here for convenience:



$$\varrho(X, Y) = \lim_{R \rightarrow +\infty} \int_{C_z} \frac{dz}{2\pi i \sqrt{z}} \int_{C_w} \frac{dw}{2\pi i \sqrt{w}} \frac{e^{R(f_\alpha(w, X, Y) - f_\alpha(z, X, Y))}}{z - w}, \quad (\text{A.1})$$

where everything is defined as in Chapter 4.

The three saddle points that are shown in the figure are all we need (the fourth one will not play any role); let us call z_1 and $z_2 = z_1^*$ the blue ones, where z_1 is the saddle point in the lower half of the complex plane, and a_3 the red one.

APPENDIX A. SADDLE-POINT METHOD FOR THE DENSITY

Let us start with the application of the saddle-point method to the integral in w : we can deform the contour so that it goes through the red saddle point via the steepest descent path, in such a way that the red point is seen as a maximum. Intuitively (but it could also be shown analytically), this path will go towards the not-shaded region, since we know that u is smaller there than in the surroundings. Then we close the contour passing through the blue saddle points. In the end, the leading behaviour is given by the surroundings of the point where the function is maximum, i.e. a_3 .

We expand the exponent around the saddle point as

$$f_\alpha(z, X, Y) \simeq f_\alpha(a_3, X, Y) + \frac{1}{2} f''_\alpha(a_3, X, Y) s^2 e^{i\varphi} \equiv f_\alpha(a_3, X, Y) + \frac{1}{2} r s^2 e^{i(\theta+2\varphi)}, \quad (\text{A.2})$$

where

$$z - a_3 \equiv s e^{i\varphi}, \quad s, r \in \mathbb{R}^+, \quad \theta, \varphi \in [-\pi, \pi) \quad (\text{A.3})$$

and the derivative is taken with respect to the first argument.

Since we have

$$\begin{cases} \operatorname{Re}[f_\alpha(z, X, Y)] \simeq \operatorname{Re}[f_\alpha(a_3, X, Y)] + \frac{1}{2} r s^2 \cos(\theta + 2\varphi) \\ \operatorname{Im}[f_\alpha(z, X, Y)] \simeq \operatorname{Im}[f_\alpha(a_3, X, Y)] + \frac{1}{2} r s^2 \sin(\theta + 2\varphi) \end{cases}, \quad (\text{A.4})$$

the steepest descent path (the one for which a_3 corresponds to the most peaked maximum possible for the real part) is the one satisfying

$$\theta + 2\varphi = \pi + 2n\pi, \quad (\text{A.5})$$

with $n \in \mathbb{Z}$. Notice also that in this direction the imaginary part is constant, so that we disregard the possibility of destructive oscillations.

In first approximation, the steepest descent path in the neighbourhood of a_3 is a vertical line (travelled up to down) because of the symmetry of our function, so we can parametrize it taking $\varphi = -\pi/2$ and $s \in [-\epsilon, \epsilon]$, with $\epsilon > 0$ infinitesimally small.

From the saddle-point method we have

$$\begin{aligned} \int_{C_w} \frac{dw}{2\pi i \sqrt{w}} \frac{e^{Rf_\alpha(w, X, Y)}}{z - w} &\simeq \int_{-\epsilon}^{+\epsilon} \frac{ds}{2\pi \sqrt{a_3}} \frac{e^{R(f_\alpha(a_3, X, Y) - \frac{1}{2} r s^2)}}{a_3 - z} \\ &\simeq e^{Rf_\alpha(a_3, X, Y)} \int_{-\infty}^{+\infty} \frac{ds}{2\pi \sqrt{a_3}} \frac{e^{-\frac{1}{2} R r s^2}}{a_3 - z} \\ &= e^{Rf_\alpha(a_3, X, Y)} \frac{1}{\sqrt{2\pi a_3 r R}} \frac{1}{a_3 - z}. \end{aligned} \quad (\text{A.6})$$

Notice how, stopping at the leading order, the two initial integrals decouple, leaving a single Gaussian integral that is easily evaluated. The sub-leading orders would not have this characteristic and the computation would be harder.

An analogous thing can be done with the integral in z , but, because of the minus sign at the exponent, this time the steepest descent path wants to pass through the saddle points in such a way that they act as minima of $\text{Re}[f_\alpha]$. As above, we expand the exponent around the saddle point as

$$f_\alpha(z, X, Y) \simeq f_\alpha(a_3, X, Y) + \frac{1}{2} f''_\alpha(a_3, X, Y) s^2 e^{2i\varphi} \equiv f_\alpha(a_3, X, Y) + \frac{1}{2} r s^2 e^{i(\theta+2\varphi)}, \quad (\text{A.7})$$

with

$$z - a_3 \equiv s e^{i\varphi}, \quad s, r \in \mathbb{R}^+, \quad \theta, \varphi \in [-\pi, \pi]. \quad (\text{A.8})$$

But this time we will choose the contour deformation in such a way that

$$\theta + 2\varphi = 2n\pi, \quad (\text{A.9})$$

with $n \in \mathbb{Z}$. (Again, the imaginary part is constant in the neighbourhood of the saddle points, ruling out destructive contributions from the oscillating part.)

In the end, the contour deformation will pass through z_1 and z_2 always staying within the shaded region; let us parametrize it as $z_1 + e^{i\varphi}s$, with $s \in [-\epsilon, \epsilon]$, $\epsilon > 0$ and $\varphi \in (-\pi/2, \pi/2)$, in the neighbourhood of z_1 . The parametrization for z_2 is just the reflection, i.e. $z_1^* + e^{-i\varphi}s$ for $s \in [-\epsilon, \epsilon]$, travelled reversely.

From the saddle-point method:

$$\begin{aligned} & \int_{C_z} \frac{dz}{2\pi i \sqrt{z}} \frac{e^{-Rf_\alpha(z, X, Y)}}{a_3 - z} \\ & \simeq e^{+i\varphi} \int_{-\infty}^{+\infty} \frac{ds}{2\pi i \sqrt{z_1}} \frac{e^{-R(f_\alpha(z_1, X, Y) + \frac{1}{2}rs^2)}}{a_3 - z_1} - e^{-i\varphi} \int_{-\infty}^{+\infty} \frac{ds}{2\pi i \sqrt{z_1^*}} \frac{e^{-R(f_\alpha(z_1^*, X, Y) + \frac{1}{2}rs^2)}}{a_3 - z_1^*} \\ & = e^{+i\varphi} \int_{-\infty}^{+\infty} \frac{ds}{2\pi i \sqrt{z_1}} \frac{e^{-R(f_\alpha(z_1, X, Y) + \frac{1}{2}rs^2)}}{a_3 - z_1} - e^{-i\varphi} \int_{-\infty}^{+\infty} \frac{ds}{2\pi i \sqrt{z_1^*}} \frac{e^{-R(f_\alpha(z_1^*, X, Y) + \frac{1}{2}rs^2)}}{a_3 - z_1^*} \\ & = \text{Im} \left[e^{i\varphi} \int_{-\infty}^{+\infty} \frac{ds}{\pi \sqrt{z_1}} \frac{e^{-R(f_\alpha(z_1, X, Y) + \frac{1}{2}rs^2)}}{a_3 - z_1} \right], \end{aligned} \quad (\text{A.10})$$

where we used that f is holomorphic almost everywhere. The Gaussian integral can be finally computed, giving

$$\int_{C_z} \frac{dz}{2\pi i \sqrt{z}} \frac{e^{-Rf_\alpha(z, X, Y)}}{a_3 - z} \simeq \frac{\sqrt{2} e^{-R \text{Re}[f_\alpha(z_1, X, Y)]}}{\sqrt{\pi Rr}} \text{Im} \left[\frac{e^{-iR \text{Im}[f_\alpha(z_1, X, Y)]} e^{i\varphi}}{\sqrt{z_1}(a_3 - z_1)} \right]. \quad (\text{A.11})$$

Notice that the potential residue contributions that are picked up are not important because they are finite, while the double integral diverges. That is why we ignored the pole during the deformations.

APPENDIX A. SADDLE-POINT METHOD FOR THE DENSITY

Since, as can be easily checked, $\frac{e^{Rf_\alpha(a_1, X, Y)}}{\sqrt{a_3}}$ is real, in the limit $R \rightarrow +\infty$

$$\boxed{\varrho(X, Y) \sim \frac{e^{R(\operatorname{Re}[f_\alpha(a_3, X, Y)] - f_\alpha(z_1, X, Y))} \operatorname{Im} \left[\frac{e^{-iR \operatorname{Im}[f_\alpha(z_1, X, Y)]} e^{i\varphi}}{\sqrt{z_1(a_3 - z_1)}} \right]}{\pi R \sqrt{a_3 |f''_\alpha(a_3, X, Y)| |f''_\alpha(z_1, X, Y)|}}, \quad (\text{A.12})$$

where the derivatives are evaluated with respect to the first argument and $\varphi \in (-\pi/2, \pi/2)$ is a phase that

$$\operatorname{Arg}[f''_\alpha(z_1, X, Y)] + 2\varphi = 2n\pi, \quad (\text{A.13})$$

for some $n \in \mathbb{Z}$.

The result that has been obtained is clearly real and, since $\operatorname{Re}[f_\alpha(a_3, X, Y) - f_\alpha(z_1, X, Y)] > 0$, diverges exponentially to ∞ , oscillating between $-\infty$ and $+\infty$ infinitely fast (actually, one could also think about tuning the oscillating factor to get a finite value, but, still, the integral is divergent almost everywhere).

This proves the divergence of the density in the regions where it is not between zero and one.

Appendix B

Hilbert Transform

In this appendix we evaluate the Hilbert transform of the function (5.35), i.e.

$$\xi(k) = -\cos(k/p) - \alpha \cos(2k/p). \quad (\text{B.1})$$

We resort to eq. (3.46), so let us start by computing the Fourier coefficients of $\xi(k)$. Since the function is even, we have $[\xi]_m = [\xi]_{-m}$ and

$$\begin{aligned} \frac{[\xi]_m + [\xi]_{-m}}{2} &= - \int_{-\pi}^{\pi} \frac{dk}{2\pi} \left(\cos\left(\frac{k}{p}\right) + \alpha \cos\left(\frac{2k}{p}\right) \right) \cos(km) \\ &= - \int_0^{\pi} \frac{dk}{2\pi} \left(\cos\left(\frac{1+pm}{p}k\right) + \cos\left(\frac{1-pm}{p}k\right) \right) \\ &\quad - \alpha \int_0^{\pi} \frac{dk}{2\pi} \left(\cos\left(\frac{1+(p/2)m}{(p/2)}k\right) \cos\left(\frac{1-(p/2)m}{(p/2)}k\right) \right). \end{aligned} \quad (\text{B.2})$$

Now,

$$\int_0^{\pi} \frac{dk}{2\pi} \cos(\gamma k) = \begin{cases} \frac{\delta_{\gamma,0}}{2}, & \text{if } \gamma \in \mathbb{Z} \\ \frac{\sin(\gamma k)}{2\pi\gamma}, & \text{otherwise} \end{cases}. \quad (\text{B.3})$$

Hence we have

$$\frac{[\xi]_m + [\xi]_{-m}}{2} = \begin{cases} -\frac{1}{2}\delta_{m,1} - \frac{1}{2}\delta_{m,-1} - \frac{\alpha}{2}\delta_{m,2} - \frac{\alpha}{2}\delta_{m,-2}, & p = 1 \\ \frac{2\cos(m\pi)}{\pi(4m^2-1)} - \frac{\alpha}{2}\delta_{m,1} - \frac{\alpha}{2}\delta_{m,-1}, & p = 2 \\ \frac{p\cos(m\pi)\sin(\pi/p)}{\pi(p^2m^2-1)} + \alpha \frac{(p/2)\cos(m\pi)\sin(\pi/(p/2))}{\pi((p/2)^2m^2-1)}, & p > 2 \end{cases}. \quad (\text{B.4})$$

Being $\xi(k)$ even, the Hilbert transform is just

$$\tilde{\xi}(k) = 2 \sum_{m=1}^{+\infty} \sin(kn) \frac{[\xi]_m + [\xi]_{-m}}{2}. \quad (\text{B.5})$$

APPENDIX B. HILBERT TRANSFORM

Now, since we are not able to give a closed form of the sum for general p , we rewrite it as an integral, which is usually more manageable, using

$$\sum_{m=1}^{+\infty} \frac{\sin(km) \cos(m\pi)}{p^2 m^2 - 1} = -\frac{\sin(k)}{2} \int_0^{+\infty} dx \frac{\sinh(x)}{\cosh(px) + \cos(k)}, \text{ for } p > 1. \quad (\text{B.6})$$

(The other sum, for $p > 2$, is analogously approached.)

Proof. First of all, we decompose the denominator using the identity

$$\frac{1}{p^2 n^2 - 1} = \frac{1}{2} \left(\frac{1}{np - 1} - \frac{1}{np + 1} \right). \quad (\text{B.7})$$

After that, for each term, we use the integral representation

$$\frac{1}{\gamma} = \int_0^{+\infty} dx e^{-\gamma x}, \quad (\text{B.8})$$

valid $\forall \gamma > 0$. Then, using also the complex representation for the sine

$$(-1)^m \sin(mk) = \frac{e^{im(k+\pi)} - e^{-im(k+\pi)}}{2i}, \quad (\text{B.9})$$

we have

$$\begin{aligned} \sum_{m=1}^{+\infty} \frac{\cos(m\pi) \sin(mk)}{p^2 m^2 - 1} &= \int_0^{+\infty} dx \sum_{m=1}^{+\infty} \frac{e^{-(pm-1)x} - e^{-(pm+1)x}}{2} \frac{e^{im(k+\pi)} - e^{-im(k+\pi)}}{2i} \\ &= \int_0^{+\infty} dx \sinh(x) \sum_{m=1}^{+\infty} e^{-pmx} \frac{e^{im(k+\pi)} - e^{-im(k+\pi)}}{2i} \\ &= \frac{1}{2i} \int_0^{+\infty} dx \sinh(x) \left(\frac{1}{1 - e^{i(k+\pi)-px}} - \frac{1}{1 - e^{-i(k+\pi)-px}} \right) \\ &= \frac{1}{2} \int_0^{+\infty} dx \sinh(x) \frac{-\sin(k)}{\cosh(px) + \cos(k)}, \end{aligned} \quad (\text{B.10})$$

thus proving (B.6).

□

Finally, we solve explicitly the integral via computer algebra systems for $p = 2$, while we leave the integral expression implicit for $p \geq 3$. From

$$\begin{aligned} \int_0^{+\infty} dx \frac{\sinh(x)}{\cosh(2x) + \cos(k)} &= \csc\left(\frac{k}{2}\right) \operatorname{arctanh}\left(\tan\left(\frac{k}{4}\right)\right) \\ &= \frac{1}{2} \csc\left(\frac{k}{2}\right) \operatorname{arctanh}\left(\sin\left(\frac{k}{2}\right)\right), \end{aligned} \quad (\text{B.11})$$

we have

$$\tilde{\xi}(k) = \begin{cases} -\sin(k) - \alpha \sin(2k) & , \quad p = 1 \\ -\frac{2}{\pi} \operatorname{arctanh}(\sin(k/2)) \cos(k/2) - \alpha \sin(k) & , \quad p = 2 \\ -\frac{p}{\pi} \int_0^{+\infty} dx \frac{\sin\left(\frac{\pi}{p}\right) \sin(k) \sinh(x)}{\cosh(px) + \cos(k)} - \alpha \frac{p}{2\pi} \int_0^{+\infty} dx \frac{\sin\left(\frac{2}{p}\pi\right) \sin(k) \sinh(x)}{\cosh\left(\frac{p}{2}x\right) + \cos(k)} & , \quad p > 2 \end{cases}. \quad (\text{B.12})$$

APPENDIX B. HILBERT TRANSFORM

Bibliography

- [1] R. Kenyon. *Lectures on Dimers*. arXiv:0910.3129, October 2009.
- [2] N. Elkies, G. Kuperberg, M. Larsen, and J. Propp. *Alternating Sign Matrices and Domino Tilings*. arXiv:math/9201305, May 1991.
- [3] W. Jockusch, J. Propp, and P. Shor. *Random Domino Tilings and the Arctic Circle Theorem*. arXiv:math/9801068, January 1998.
- [4] H. Cohn, N. Elkies, and J. Propp. *Local Statistics for Random Domino Tilings of the Aztec Diamond*. Duke Mathematical Journal, 85(1):117–166, October 1996.
- [5] K. Johansson. *Non-Intersecting Paths, Random Tilings and Random Matrices*. Probability Theory and Related Fields , 123(2):225–280, June 2002.
- [6] F. Colomo and A. G. Pronko. *Third-Order Phase Transition in Random Tilings*. Physical Review E, 88(4):042125, October 2013.
- [7] A. M. Vershik and S. V. Kerov. *Asymptotic of the Largest and the Typical Dimensions of Irreducible Representations of a Symmetric Group*. Functional Analysis and Its Applications, 19(1):21–31, 1985.
- [8] E. A. Rakhmanov. *Equilibrium Measure and the Distribution of Zeros of the Extremal Polynomials of a Discrete Variable*. Sbornik: Mathematics, 187(8):1213–1228, August 1996.
- [9] B. Nienhuis, H. J. Hilhorst, and H. W. J. Blote. *Triangular SOS Models and Cubic-Crystal Shapes*. Journal of Physics A: Mathematical and General, 17(18):3559–3581, December 1984.
- [10] R. Cerf and R. Kenyon. *The Low-Temperature Expansion of the Wulff Crystal in the 3D Ising Model*. Communications in Mathematical Physics, 222(1):147–179, August 2001.
- [11] P. L. Ferrari and H. Spohn. *Step Fluctuations for a Faceted Crystal*. arXiv:cond-mat/0212456, January 2003.

BIBLIOGRAPHY

- [12] H. Cohn, M. Larsen, and J. Propp. *The Shape of a Typical Boxed Plane Partition*. arXiv:math/9801059, May 2002.
- [13] A. Okounkov and N. Reshetikhin. *Correlation Function of Schur Process with Application to Local Geometry of a Random 3-Dimensional Young Diagram*. arXiv:math/0107056, January 2003.
- [14] R. Kenyon, A. Okounkov, and S. Sheffield. *Dimers and Amoebae*. arXiv:math-ph/0311005, November 2003.
- [15] R. Kenyon and A. Okounkov. *Planar Dimers and Harnack Curves*. arXiv:math/0311062, October 2004.
- [16] R. Kenyon and A. Okounkov. *Limit Shapes and the Complex Burgers Equation*. Acta Mathematica, 199(2):263–302, 2007.
- [17] N. Allegra, J. Dubail, J.-M. Stéphan, and J. Viti. *Inhomogeneous Field Theory inside the Arctic Circle*. Journal of Statistical Mechanics: Theory and Experiment, 2016(5):053108, May 2016.
- [18] D. M. Bressoud. *Proofs and Confirmations: The Story of the Alternating Sign Matrix Conjecture*. Spectrum Series. Cambridge University Press, Cambridge ; New York, 1999.
- [19] F. Colomo and A. G. Pronko. *The Limit Shape of Large Alternating Sign Matrices*. SIAM Journal on Discrete Mathematics, 24(4):1558–1571, January 2010.
- [20] R. J. Baxter. *Exactly Solved Models in Statistical Mechanics*. Dover Publications, Mineola, N.Y, dover ed edition, 2007. OCLC: ocn154799434.
- [21] K. Palamarchuk and N. Reshetikhin. *The 6-Vertex Model with Fixed Boundary Conditions*. arXiv:1010.5011, October 2010.
- [22] F. Colomo and A. G. Pronko. *The Arctic Curve of the Domain-Wall Six-Vertex Model*. Journal of Statistical Physics, 138(4-5):662–700, March 2010.
- [23] A. Borodin, I. Corwin, and V. Gorin. *Stochastic Six-Vertex Model*. Duke Mathematical Journal, 165(3):563–624, February 2016.
- [24] B. Debin, P. Di Francesco, and E. Guitter. *Arctic Curves of the Twenty-Vertex Model with Domain Wall Boundaries*. Journal of Statistical Physics, 179(1):33–89, April 2020.

BIBLIOGRAPHY

- [25] D. Romik. *The Surprising Mathematics of Longest Increasing Subsequences*. Institute of Mathematical Statistics Textbooks. Cambridge University Press, New York, 2015.
- [26] C. Schensted. *Longest Increasing and Decreasing Subsequences*. Canadian Journal of Mathematics, 13:179–191, 1961.
- [27] J. Baik, P. Deift, and K. Johansson. *On the Distribution of the Length of the Longest Increasing Subsequence of Random Permutations*. arXiv:math/9810105, March 1999.
- [28] J.-M. Stéphan. *Extreme Boundary Conditions and Random Tilings*. arXiv:2003.06339, March 2020.
- [29] P. Jordan and E. Wigner. *Über das Paulische äquivalenzverbot*. Zeitschrift für Physik, 47(9-10):631–651, September 1928.
- [30] J. Negele and H. Orland. *Quantum Many-Particle Systems*. Number 68 in Frontiers in Physics. Addison-Wesley, Reading, Mass., 5. print edition, 1988. OCLC: 833252580.
- [31] G. Mussardo. *Statistical Field Theory: An Introduction to Exactly Solved Models in Statistical Physics*. Oxford Graduate Texts. Oxford Univ. Press, Oxford, 2010. OCLC: 699263129.
- [32] P.W. Kasteleyn. *The Statistics of Dimers on a Lattice*. Physica, 27(12):1209–1225, December 1961.
- [33] H. N. V. Temperley and M. E. Fisher. *Dimer Problem in Statistical Mechanics—an Exact Result*. Philosophical Magazine, 6(68):1061–1063, August 1961.
- [34] E. H. Lieb. *Solution of the Dimer Problem by the Transfer Matrix Method*. Journal of Mathematical Physics, 8(12):2339–2341, December 1967.
- [35] J.-M. Stéphan, S. Furukawa, G. Misguich, and V. Pasquier. *Shannon and Entanglement Entropies of One- and Two-Dimensional Critical Wave Functions*. Physical Review B, 80(18):184421, November 2009.
- [36] F. Alet, Y. Ikhlef, J. L. Jacobsen, G. Misguich, and V. Pasquier. *Classical Dimers with Aligning Interactions on the Square Lattice*. Physical Review E, 74(4):041124, October 2006.
- [37] E. Lieb, T. Schultz, and D. Mattis. *Two Soluble Models of an Antiferromagnetic Chain*. Annals of Physics, 16(3):407–466, December 1961.

BIBLIOGRAPHY

- [38] R. Livi and P. Politi. *Nonequilibrium Statistical Physics: A Modern Perspective*. Cambridge University Press, Cambridge, United Kingdom New York, NY Port Melbourne, 2017. OCLC: 1004772077.
- [39] J. I. Latorre and A. Riera. *A Short Review on Entanglement in Quantum Spin Systems*. Journal of Physics A: Mathematical and Theoretical, 42(50):504002, December 2009.
- [40] N. Nagaosa and S. Heusler. *Quantum Field Theory in Strongly Correlated Electronic Systems*. Texts and Monographs in Physics. Springer, Berlin, 1999. OCLC: 845281288.
- [41] T. Giamarchi. *Quantum Physics in One Dimension*. Number 121 in The International Series of Monographs on Physics. Clarendon ; Oxford University Press, Oxford : New York, 2004. OCLC: ocm52784724.
- [42] P. Calabrese and J. Cardy. *Evolution of Entanglement Entropy in One-Dimensional Systems*. Journal of Statistical Mechanics: Theory and Experiment, 2005(04):P04010, April 2005.
- [43] J.-M. Stéphan and J. Dubail. *Local Quantum Quenches in Critical One-Dimensional Systems: Entanglement, the Loschmidt Echo, and Light-Cone Effects*. Journal of Statistical Mechanics: Theory and Experiment, 2011(08):P08019, August 2011.
- [44] P. Calabrese and J. Cardy. *Quantum Quenches in 1 + 1 Dimensional Conformal Field Theories*. Journal of Statistical Mechanics: Theory and Experiment, 2016(6):064003, June 2016.
- [45] J. Dubail, J.-M. Stéphan, J. Viti, and Pasquale Calabrese. *Conformal Field Theory for Inhomogeneous One-Dimensional Quantum Systems: The Example of Non-Interacting Fermi Gases*. SciPost Physics, 2(1):002, February 2017.
- [46] G. C. Wick. *The Evaluation of the Collision Matrix*. Physical Review, 80(2):268–272, October 1950.
- [47] M. Gaudin. *Une démonstration simplifiée du théorème de wick en mécanique statistique*. Nuclear Physics, 15:89–91, February 1960.
- [48] C. Boutillier, J. Bouttier, G. Chapuy, S. Corteel, and S. Ramassamy. *Dimers on Rail Yard Graphs*. Annales de l’Institut Henri Poincaré D, 4(4):479–539, December 2017.

- [49] B. Simon. *Orthogonal Polynomials on the Unit Circle*. Number v. 54 in American Mathematical Society Colloquium Publications. American Mathematical Society, Providence, R.I, 2005. OCLC: ocm56730074.
- [50] H. Widom. *Asymptotic Behavior of Block Toeplitz Matrices and Determinants. II*. Advances in Mathematics, 21(1):1–29, July 1976.
- [51] G. Szegö. *On Certain Hermitian Forms Associated with the Fourier Series of a Positive Function*. In R. Askey, editor, *Gabor Szegö: Collected Papers*, pages 269–283. Birkhäuser Boston, Boston, MA, 1982.
- [52] M. A. Cazalilla. *Bosonizing One-Dimensional Cold Atomic Gases*. Journal of Physics B: Atomic, Molecular and Optical Physics, 37(7):S1–S47, April 2004.
- [53] F. W. King. *Hilbert Transforms*. Number 124-125 in Encyclopedia of Mathematics and Its Applications. Cambridge University Press, Cambridge [Eng.] ; New York, 2009. OCLC: ocn299942188.
- [54] J. Mathews and R. L. Walker. *Mathematical Methods of Physics*. W. A. Benjamin, New York, 2d ed edition, 1970.
- [55] P. Flajolet and R. Sedgewick. *Analytic Combinatorics*. Cambridge University Press, Cambridge ; New York, 2009. OCLC: ocn244767782.
- [56] M. Abramowitz. *Handbook of Mathematical Functions: With Formulas, Graphs, and Mathematical Tables*. Dover Publications, 2012. OCLC: 868965076.
- [57] A. Okounkov. *The Uses of Random Partitions*. arXiv:math-ph/0309015, September 2003.
- [58] M. Prähofer and H. Spohn. *Scale Invariance of the PNG Droplet and the Airy Process*. Journal of Statistical Physics, 108(5/6):1071–1106, 2002.
- [59] Y. V. Sidorov, M. V. Fedoryuk, and M. I. Shabunin. *Lectures on the Theory of Functions of a Complex Variable*. Mir Publishers, Moscow, 1985.
- [60] A. Okounkov and N. Reshetikhin. *Random Skew Plane Partitions and the Pearcey Process*. arXiv:math/0503508, April 2005.
- [61] S. Mkrtchyan. *Scaling Limits of Random Skew Plane Partitions with Arbitrarily Sloped Back Walls*. Communications in Mathematical Physics, 305(3):711–739, August 2011.
- [62] C. Boutillier, S. Mkrtchyan, N. Reshetikhin, and P. Tingley. *Random Skew Plane Partitions with a Piecewise Periodic Back Wall*. Annales Henri Poincaré, 13(2):271–296, March 2012.

BIBLIOGRAPHY

- [63] T. Berggren and M. Duits. *Correlation Functions for Determinantal Processes Defined by Infinite Block Toeplitz Minors*. arXiv:1901.10877, August 2019.
- [64] A. G. Abanov. *Hydrodynamics of Correlated Systems: Emptiness Formation Probability and Random Matrices*. In É. Brézin, V. Kazakov, D. Serban, P. Wiegmann, and A. Zabrodin, editors, *Applications of Random Matrices in Physics*, volume 221, pages 139–161. Springer Netherlands, Dordrecht, 2006.
- [65] E. Y. Loh, J. E. Gubernatis, R. T. Scalettar, S. R. White, D. J. Scalapino, and R. L. Sugar. *Sign Problem in the Numerical Simulation of Many-Electron Systems*. Physical Review B, 41(13):9301–9307, May 1990.
- [66] F. Becca and S. Sorella. *Quantum Monte Carlo Approaches for Correlated Systems*. Cambridge University Press, first edition, November 2017.
- [67] A. Gainutdinov, D. Ridout, and I. Runkel. *Logarithmic Conformal Field Theory*. Journal of Physics A: Mathematical and Theoretical, 46(49):490301, December 2013.
- [68] F. Colomo and A. Sportiello. *Arctic Curves of the Six-Vertex Model on Generic Domains: The Tangent Method*. Journal of Statistical Physics, 164(6):1488–1523, September 2016.
- [69] J. de Gier, R. Kenyon, and S. S. Watson. *Limit Shapes for the Asymmetric Five Vertex Model*. arXiv:1812.11934, December 2018.
- [70] A. Aggarwal. *Arctic Boundaries of the Ice Model on Three-Bundle Domains*. arXiv:1812.03847, November 2019.
- [71] D. Keating, N. Reshetikhin, and A. Sridhar. *Integrability of Limit Shapes of the Inhomogeneous Six Vertex Model*. arXiv:2004.08971, April 2020.
- [72] R. Kenyon and I. Prause. *Gradient Variational Problems in \mathbb{R}^2* . arXiv:2006.01219, June 2020.
- [73] C. A. Tracy and H. Widom. *Level-Spacing Distributions and the Airy Kernel*. Communications in Mathematical Physics, 159(1):151–174, January 1994.

Acknowledgements

I am grateful to my two supervisors, Jean-Marie and Filippo, for their guidance and their fundamental comments about this work. Thank you also for making my traineeship in Lyon possible: it has been a wonderful experience. A special acknowledgement to Jean-Marie, who initiated me to research and helped me setting in Lyon.

I would also like to express my gratitude to my parents and to Giulia for always being there and for providing me unfailing support throughout all my years of study. This accomplishment would not have been possible without you.